

Max-Planck-Institut für Astrophysik

Physik Department

Technische Universität München

**Simulating supernova shock propagation
through stellar envelopes in 3D**

Nicolay J. Hammer

Vollständiger Abdruck der von der Fakultät für Physik der Technischen Universität München zur Erlangung des akademischen Grades eines

Doktors der Naturwissenschaften (Dr. rer. nat.)

genehmigten Dissertation.

Vorsitzender: Univ.-Prof. Dr. L. Oberauer

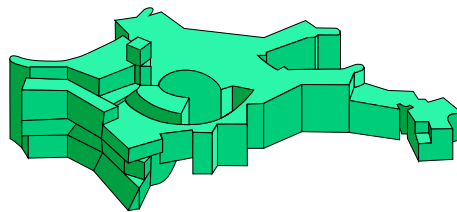
Prüfer der Dissertation:

1. Priv.-Doz. Dr. E. Müller
2. Univ.-Prof. Dr. Th. Feldmann

Die Dissertation wurde am 17. 11. 2008 bei der Technischen Universität München eingereicht und durch die Fakultät für Physik am 12. 01. 2009 angenommen.

Simulating supernova shock propagation through stellar envelopes in 3D

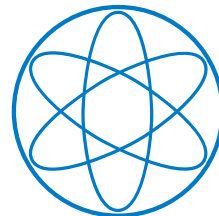
Nicolay J. Hammer



Max Planck Institut für Astrophysik



Technische Universität München



Physik Department

”A kite flies highest against the wind, not with it.”

Winston Churchill (1874-1965)

for my wonderful parents

Elvira and Joachim

and for my beloved

Ruth

Contents

Zusammenfassung	1
Abstract	3
I Introduction	5
1 Motivation	7
1.1 Historical Supernovae ¹	7
1.2 Types of Supernovae	8
1.3 The Supernova SN 1987A	10
1.3.1 General	10
1.3.2 Evidence for Mixing	12
2 Field of Research	15
2.1 Core Collapse Supernovae	15
2.1.1 Core Collapse and Bounce	16
2.1.2 Stalling and Reviving the Shock Wave	16
2.1.3 Standing Accretion Shock Instability	19
2.1.4 The Shock and the Envelope	20
2.2 Evidence for Mixing and Asphericity in ccSNe	20
2.3 Earlier Work on Mixing and Asphericity in SN Models	23
3 The Designation of this Thesis	25
II Fundamentals	27
4 The PROMETHEUS Code	29
4.1 Physical Approximations and Numerical Algorithms	29
4.2 Performance, Scaling Behaviour, and the need for HPC Systems	30
4.3 Computational Setup	30
4.4 Initial Models	32
4.4.1 Model Structure	32
4.4.2 Nuclear Composition	33

4.4.3	Thermodynamical Quantities	33
4.4.4	Energetics	33
4.4.5	Asphericity and Perturbations	34
4.4.6	Comparison Models in 2D	35
5	Hydrodynamic Instabilities	37
5.1	Fundamental Equations	37
5.2	Rayleigh-Taylor Instability	40
5.2.1	Introduction	40
5.2.2	Linear Analysis in Plane Geometry	41
5.2.3	Linear Analysis in Spherical Geometry	42
5.2.4	Non-linear Modelling, Numerical Studies and Further Details	43
5.3	Kelvin-Helmholtz Instability	44
5.3.1	Introduction	44
5.3.2	Linear Analysis of a Compressible Fluid in Plane Geometry	45
5.3.3	Further Details	47
5.4	Richtmyer-Meshkov Instability	48
5.4.1	Introduction	48
5.4.2	Impulsive Theory in Plane Geometry	49
5.4.3	Linear Compressible Theory in Plane Geometry	50
5.4.4	Spherical Case, Non-linear Theory and Further Studies	50
III	Simulations in 3 Dimensions	51
6	Analysis of 3D Runs	53
6.1	Testing the Resolution of Our Setup	53
6.2	Energetics and total Mass	53
6.2.1	Energy of the Explosion	53
6.2.2	Saturation of the Explosion Energy	55
6.2.3	Conservation of Mass	55
6.3	The Rayleigh-Taylor Instability in 3 Dimensions	56
6.4	Metal Velocities and Masses	57
6.4.1	Mass fractions of chemical species in Radial-Velocity Space	57
6.4.2	Clump velocity in 3D vs. 2D	60
6.4.3	Spatial Distribution of Heavy Elements	65
6.5	The Richtmyer-Meshkov Instability in 3 Dimensions	68
6.5.1	RMI at the H/He Interface	68
6.5.2	Time Scale of the Development	68
6.5.3	Analysis Using Volume-Integrated Vorticity	70
6.5.4	RMI at the (C+O)/He Interface	72
6.6	Discussion and Conclusions	72
6.6.1	Strength of Our Study	72
6.6.2	Weakness of Our Study	72
6.6.3	Discussion of Our Results	73
6.6.4	Outlook on Future Works	73

IV Appendix	75
A Additional Plots	77
1.1 Additional Plots Initial Model	77
1.2 Additional Plots Model 3D3	80
1.3 Additional Plots Model 3D2	89
1.4 Additional Plots Model 2D2	94
1.5 Additional Plots Model 2D80	98
B Definitions & Abbreviations	103
C Mathematics	105
3.1 Spherical Polar Coordinates	105
3.2 Vector Operators in Cartesian Coordinates	105
3.3 Vector Operators in Spherical Polar Coordinates	106
Bibliography	107
Online References	111
Acknowledgement	112
Curriculum Vitae	114

List of Tables

4.1	Scaling Behaviour Of PROMETHEUS	31
4.2	Model Parameter	34
6.1	Masses of Nuclear Species	57
B.1	Definitions & Abbreviations	103

List of Figures

1.1	Spectra and lightcurves of SNe.	8
1.2	Supernovae classification scheme.	9
1.3	Light curve and spectra of SN 1987A	10
1.4	SN radial velocity profile	12
2.1	A presupernova star	15
2.2	Core Collapse — Core Bounce — Shock Evolution	17
2.3	Reviving the stalled shock wave.	18
2.4	The advective-acoustic cycle	19
2.5	Image in optical emission lines of Cas A	21
2.6	Density and entropy distribution of model b23a and b18b	22
4.1	PROMETHEUS parallel SpeedUp and scaling efficiency	30
4.2	Computational grid.	31
4.3	Composition of the Initial Model 3D3	32
4.4	The shock wave of the initial model 3D3	35
5.1	Rayleigh-Taylor Instability	40
5.2	RTI configuration	41
5.3	Development of a Kelvin-Helmholtz wave.	44
5.4	KHI geometry and dispersion relation.	45
5.5	Computation of NOVA Richtmyer-Meshkov Instabilit experiments.	48
5.6	RMI setup and vortex generation.	49
6.1	Density distribution of model b23a 3 000 s after core collapse	54
6.2	Total energies and masses vs. time	55
6.3	Position of the shock wave vs. density gradients.	56
6.4	Fraction of fast metal metal in model 3D3	58
6.5	Metal Mass vs. Velocity, Model: 3D3	59
6.6	The "helium wall" in 2D and 3D.	60
6.7	Parametric sphere & torus.	61
6.8	Metal Mass vs. Velocity, Model: 2D2 vs. 3D3, slice 2	62
6.9	Metal Mass vs. Velocity, Model: 2D80 vs. 3D3, slice 80	63
6.10	Angular data bins in longitudinal direction of model 3D3.	65
6.11	Metal Mass vs. Velocity, binned longitudinal, Model: 3D3	66
6.12	Metal iso-cotours: model 3D3.	67
6.13	H/He interface of model 3D3 at late epochs.	68
6.14	ΔR_s at $R_s \approx R_{H/He}$ and the RMI of model 2D80	69

6.15	Integrated absolut vorticity of model 3D3.	70
6.16	RMI at the C/He interface.	71
A.1	Progenitors density structures.	77
A.2	Progenitors density slope.	78
A.3	Progenitors temperature structures.	78
A.4	Progenitor nuclear composition structure.	79
A.5	Entropy iso-contour plots of model 3D3	81
A.6	Entropy iso-contour plots of model 3D3, slice 2	82
A.7	Entropy iso-contour plots of model 3D3, slice 80	83
A.8	Density iso-contour plots of model 3D3	84
A.9	Density iso-contour plots of model 3D3, slice 2	85
A.10	Density iso-contour plots of model 3D3, slice 80	86
A.11	Metal Mass vs. Velocity, Model: 3D3, slice 2	87
A.12	Metal Mass vs. Velocity, Model: 3D3, slice 80	88
A.13	Metal Mass vs. Velocity, Model: 3D2	90
A.14	Entropy iso-contour plots of model 3D2	91
A.15	Density iso-contour plots of model 3D2	92
A.16	Metal iso-contours: model 3D2.	93
A.17	Metal Mass vs. Velocity, Model: 2D2	95
A.18	Entropy iso-contour plots of model 2D2	96
A.19	Density iso-contour plots of model 2D2	97
A.20	1D velocity profile of model 2D80.	98
A.21	1D pressure profiles of model 2D80.	99
A.22	Metal Mass vs. Velocity, Model: 2D80	100
A.23	Entropy iso-contour plots of model 2D80	101
A.24	Density iso-contour plots of model 2D80	102
C.1	Definition of spherical polar coordinates	105

Zusammenfassung

3D Simulationen der Stoßpropagation durch Supernovahüllen

Die vorliegende Arbeit beschäftigt sich mit dem dynamischen Mischen von Nukleosyntheseprodukten in der Hülle von Core-Collapse Supernovae. Mit Hilfe von drei-dimensionalen Computermodellen wurde der Einfluß verschiedener hydrodynamischer Instabilitäten auf das Mischverhalten und die dynamischen Prozesse in der Hülle untersucht.

Dabei wurden neue Erkenntnisse über die Inhomogenität der gemischten Hüllenmaterie und die Maximalgeschwindigkeit schwerer Nukleosyntheseprodukte gewonnen. Diese wurden mit Ergebnissen von Vorläuferarbeiten verglichen und diskutiert. Des Weiteren wurden Vergleiche mit Beobachtungen der Supernova SN 1987A gezogen.

2 *Zusammenfassung*

Abstract

Simulating supernova shock propagation through stellar envelopes in 3D

The following work addresses the dynamical mixing of nucleosynthesis products in envelopes of core collapse supernovae. The influence of hydrodynamic instabilities on the mixing and the dynamics was investigated by means of three dimensional computer models.

New insights into the inhomogeneity of the mixed envelope matter and the maximum velocity of heavy nucleosynthesis products were gained. The results are discussed and compared with previous works and to observations of SN 1987A.

Part I

Introduction

Chapter 1

Motivation

1.1 Historical Supernovae¹

The phenomenon of supernovae (SNe) is already known for a long time, even though the true nature of it was not understood up to the 1940's. These “new stars” (lat: stella nova → new star), sometimes also called “guest stars”, suddenly appeared, were visible for some weeks, and faded away again. Such events were reported by astronomers in China as well as in the Middle East and in Europe in the year 185 A. D. and on 1 May 1006, which is supposed to be the brightest SNe recorded in human history, “bright enough to cast shadows on the ground at night, brighter than the quarter moon” (Marschall 1988). The remnants of both SNe can be observed as radio sources today.

Another supernova (SN) was seen by the Chinese in 1054, but not by others. It left behind the supernova remnant (SNR), which is known today as the Crab Nebulae. In contrast to the other remnants, a compact stellar remnant is found inside this SN remnant, acting as a pulsar. This means that it emits pulses of electromagnetic radiation, 30 per second in that case.

On 17 November 1572 the young Tycho Brahe, a Danish astronomer, discovered another SN in the constellation Cassiopeia and observed it for several months. Another one was described in detail by Johannes Kepler, one of the most famous astronomers in history, in October 1604. The supernova which left behind the SNR Cas A was not observed at all. However, taking into account the size and the expansion velocity of the remnant, the explosion must have seen somewhen between 1650 and 1680.

The last SN visible for the naked eye and the first one since Kepler's SN in 1604 went off on 23 February 1987 und was first seen by a few professional and amateur astronomers. Because it influenced astronomy and astrophysics greatly, as well as it is of fundamental importance for this work, I will give more details in Section 1.3.

Between 1885 and the 1930's some supernovae were also discovered in neighbouring galaxies. Then, Fritz Zwickey and his assistant J. J. Johnson, who were working at CalTech, started a systematic search programm and found 20 SNe within half a decade.

Up to the late 1990's astronomers discovered 10 to 30 SNe each year making the total number increase to about 700. At that date extended automatic supernova search programmes using robotic telescope units were started, e.g. Lick Observatory and the Tenagra Observatory Supernova Searches (LOTOSS). They “produce” between 200 and 300 SNe each year, so the total number has reached

¹This Section is based on section I.A and I.B of Bethe (1990) and the Book *The Supernova Story* by Marschall.

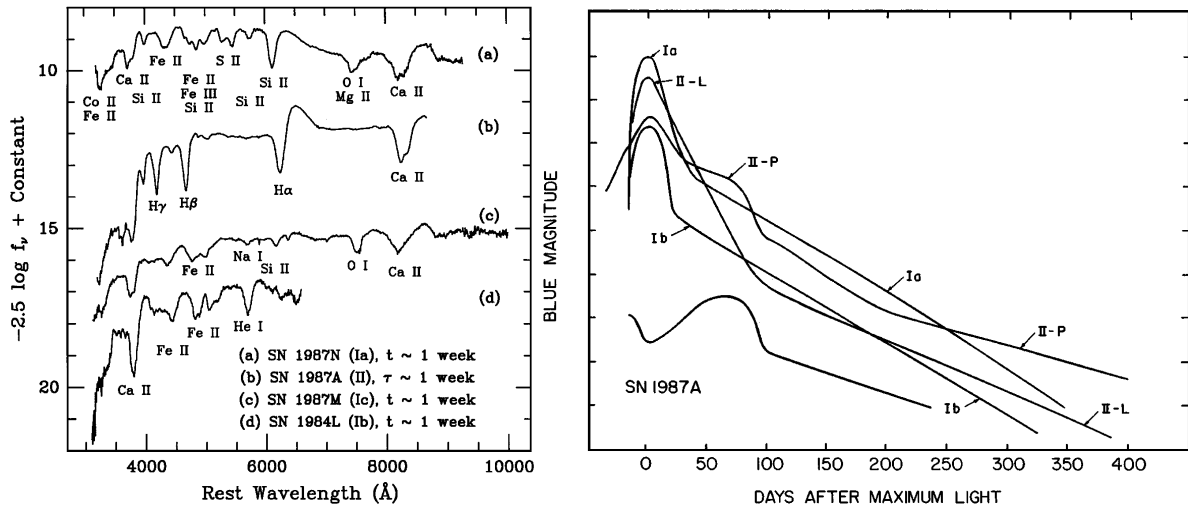


Figure 1.1: Left: Early-time spectra of SNe, showing the four major types and subtypes. The variables t and τ represent the time after observed B-band maximum, and the time after core collapse, respectively. Right: Schematic light curves for SNe of Types Ia, Ib, II-L, II-P, and SN 1987A. The curve for SNe Ib includes SNe Ic as well, and represents an average. Figures and description from Filippenko (1997).

several thousand known supernovae up to now (see *List of Supernovae* at the Harvard-Smithsonian Center for Astrophysics).

1.2 Types of Supernovae

Minkowski (1941) established two distinct classes of supernovae. Zwicky originally sorted his SNe in a system of five classes, but afterwards the two class system was adopted (Figure 1.2). The system was extended by additional subclasses, resulting in the following observer's picture. SNe of Type I, which show no hydrogen lines and SNe of Type II which do (Figure 1.1). The progenitors of Type I SNe are hydrogen deficient objects, whereas the progenitors of Type II have a relatively thick hydrogen envelope.

The term Type IIb was invented by Woosley et al. (1987) in connection with the first models for SN 1987A. It is now usually used for SNe which show the spectral behaviour of Type II at maximum light and in the early phase of their evolution, and which make a transition towards the spectral behaviour of a Type Ib SNe at later phases (~ 30 -40 days after maximum light).

The class of Type I SNe is further subdivided into Type Ia SNe, showing rather strong silicon lines and Type Ib/c with no silicon lines. The difference between the subclasses b and c is the appearance of helium lines. In contrast to that, the class of Type II SNe is further subdivided into Type III, Type IIP, and Type IIb, mainly by the behaviour of their lightcurves. Supernovae of Type III (“linear”) show a sharper maximum followed by a steep decline in their lightcurves, whereas SNe of Type IIP (“plateau”) have a broader maximum followed by a plateau (i.e. an almost constant luminosity) from roughly day thirty to a hundred days after maximum light and a shallower decline afterwards compared to Type III SNe.

Sometimes a fourth Type II subclass named Type II η is used, which is characterised by narrow emission lines on top of the broad absorption features. It is speculated that these are Type II SNe

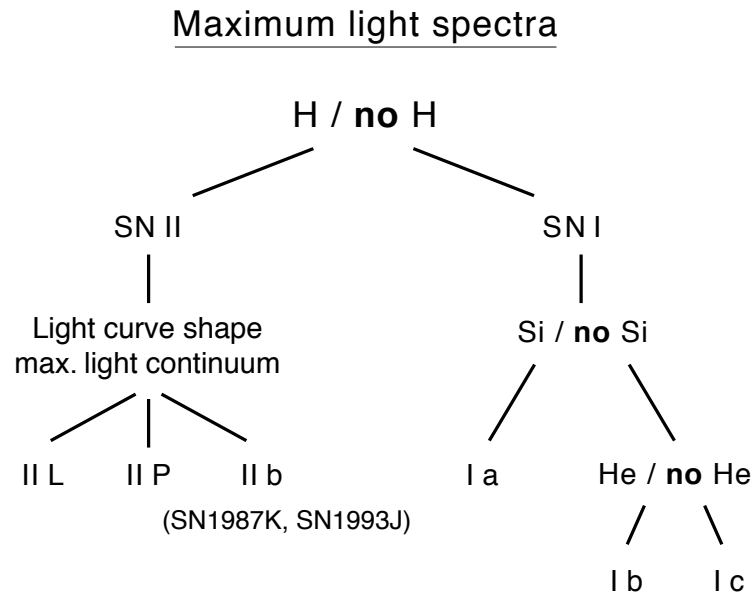


Figure 1.2: Supernovae classification scheme. Figure from Harkness & Wheeler (1990).

sitting in the middle of massive stellar outflows, and that the emission lines are the result of the SN ejecta interacting with those massive stellar outflows. Every supernova of Type II not matching the subclasses mentioned so far is usually classified as a peculiar SN of Type II, or SN Ipec.

Over the times two ideas were suggested for the energy source of supernovae. Baade & Zwicky (1934) suggested that the source for the tremendous energy of supernova explosions is the gravitational collapse of the stellar core to a neutron star (NS). They used the new concept of neutron stars which was proposed by Landau in 1932. The rivalling idea, suggested by Hoyle & Fowler (1960) and Fowler & Hoyle (1964), was that the energy is released in a thermonuclear explosion.

Today it is commonly accepted that both ideas are realised in nature. Thus, SNe of Type Ia are thermonuclear explosions of a C/O white dwarf. The white dwarf accretes material from a companion star until it reaches the Chandrasekhar mass limit, resulting in the ignition of its degenerated carbon core. Since the white dwarf has no hydrogen envelope or only an extreme thin one, no hydrogen lines are visible in the spectrum of the resulting Type Ia supernova.

Supernovae of the other types, i.e. Type Ib/c and Type II, are due to gravitational core collapse of massive stars at the end of their thermonuclear evolution. I will present an overview of the mechanism of core collapse supernovae (ccSNe) in Section 2.1.

Nowadays, it seems likely that there is a rather continuous transition between the SNe types II, Ib, and Ic, depending on the mass loss of the progenitor during its evolution. Except for Type Ia SNe, they are all ccSNe. Reducing the mass of the hydrogen envelope, one gets a SN of Type Iip, Type III, and of Type IIb if the hydrogen envelope has nearly vanished. A star completely stripped from its hydrogen envelope will produce a Type Ib SN and, if the helium shell is also stripped, one will get SNe of Type Ic.

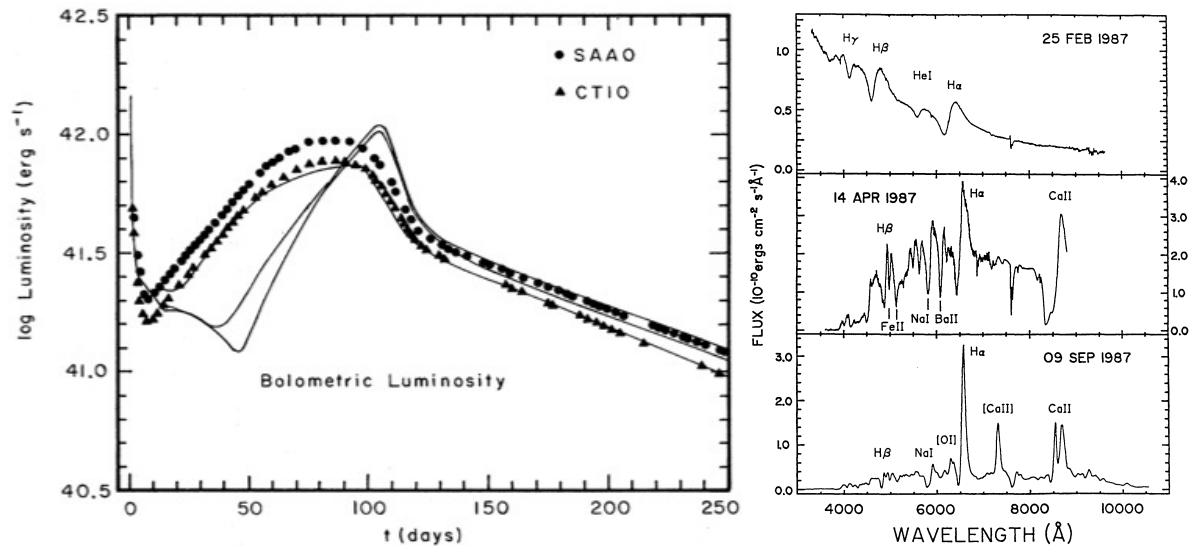


Figure 1.3: Left panel: Bolometric luminosity of Supernova 1987A, as observed by Cerro Tololo Inter-American Observatory (CTIO) and the South African Astronomical Observatory (SAAO). The three theoretical curves are from Woosley et al. (1988b); the one that fits CTIO includes mixing, the other two do not. Figures and description from Bethe (1990)

Right panel: The optical spectrum of SN 1987A at three different epochs: (a) February 25, 1987, only 40 hr after core collapse. Note the broad profiles of the hydrogen and helium lines and the large blueshifts of the P Cygni absorption components. (b) April 14, 1987, 50 days after core collapse. The spectrum is now dominated by lines of low ionisation elements. Note the strength of the barium line at 6142\AA . (c) September 9, 1987, more than 100 days after the maximum of the bolometric light curve. The spectrum has by this time taken on more of a nebular appearance, with strong emission lines of hydrogen, oxygen, calcium, and sodium dominating [observations from Cerro Tololo Inter-American Observatory (CTIO); figure from Woosley et al. (1988b)]. Figure from Woosley & Phillips (1988) and description from Arnett et al. (1989b).

1.3 The Supernova SN 1987A

1.3.1 General

The Supernova SN 1987A certainly is the most detailed studied supernova up to now. It is the first supernova from which neutrinos are observed. It is also the only stellar neutrino source so far (besides the sun) which was detected in neutrinos.

Three hours before SN 1987A was discovered by its optical outburst, two underground detectors had already recognised signals from the core collapse itself (e.g. Arnett 1987; Bethe 1990), more precisely from the neutrino burst which followed the collapse of the stellar core. The Japanese detector Kamiokande II, located in the Kamioka mine, detected 12 events in a time interval of 12.44 seconds (see Hirata et al. 1987, 1988), and the IMB detector located in the Morton-Thiokol mine (Ohio, USA) detected 8 neutrinos in a time interval of 5.58 seconds (see Bionta et al. 1987; Bratton et al. 1988). The detected signals of both laboratories coincide perfectly in time, and the detection matched the expected time of the supernova's neutrino burst so well, that there was no doubt that they had detected the core collapse of Sk-69 202, the progenitor of SN 1987A. The reported detections by two other neutrino detectors, namely the Italian-Soviet Liquid Scintillation Detector neutrino telescope located

underneath Mont Blanc and the Baksan neutrino telescope in the North Caucasus Mountains, are believed to be stochastic events (e.g. Arnett 1987; Bethe 1990).

A star of the Sanduleak catalogue, Sk -69 202, coincided in its position with SN 1987A, and after the supernova had faded away in the UV range, it turned out that this star had disappeared. Sk -69 202 was a B3 I blue supergiant, which was quite a surprise since it was always believed that the progenitors of Type II supernovae are red supergiants. SN 1987A showed a very rapid brightening in the first days, which immediately pointed to a progenitor having an atmosphere more compact than a red supergiant.

Several ideas were suggested why SN 1987A's progenitor was a blue rather compact star, e.g. severe mass loss due to stellar winds (e.g. Chevalier & Fransson 1987) or due to interaction with a binary companion (e.g. Fabian et al. 1987). Another idea was an unusual stellar evolution track caused by the low metallicity in the Large Magellanic Cloud (LMC). This was the result of one of the most thorough studies of that "*blue riddle*" by Woosley et al. (1988b). Even though there is still a discussion going on about the progenitor of SN 1987A, it is nowadays commonly accepted that has returned to a blue stage after encountering a red phase for some 10^5 years before, as discussed by Woosley et al. (1988b).

But SN 1987A was not only remarkable because of its small distance and the observed neutrino signal. Although the prominent hydrogen features of its optical spectrum are clearly indicating its Type II nature, the optical spectrum of SN 1987A (Figure 1.4, right panel) as well as the UV and IR spectra show much more rapid changes than in ordinary SN of Type II, including a phase where the spectrum is dominated by spectral features of elements in low ionisation stages.

The bolometric lightcurve of SN 1987A (Figure 1.4, left panel) shows a significant drop in the first few days. Thereafter, it brightens up again, finally reaching a 2nd maxima lasting for more than hundred days. Afterwards the lightcurve follows an exponential decline. The adiabatic expansion of the exploding star reduces its reservoir of thermal energy, decreasing the density and the temperature. This also shortens the diffusion time scale of photons, until radiation can escape freely from the expanding supernova atmosphere. The strong decline of the luminosity in the beginning is the cooling tail of the stars photosphere heated by the shock breakout. The luminosity can be expressed as

$$L = 4\pi R^2 \sigma T^4 \quad , \quad (1.1)$$

where R denotes the radius and T the temperature of the star's photosphere (σ is the Stefan-Boltzmann radiation constant). Directly after shock breakout the temperature drops linearly with time as the stellar envelope behaves as an homologous adiabatic expanding ideal gas $T \sim V^{\frac{1}{3}}$ (e.g. Landau & Lifschitz 1991), thus the luminosity decreases correspondingly. Homologous expansion means that the expansion velocity is proportional to the radius. The photosphere is defined by the recombination front, moving steadily into the inner mass shells of the supernova atmosphere. The recombination front the surface separating the hotter inner parts of the stellar envelope, consisting out of fully ionised plasma, from the cooler outer parts consisting out of neutral or partially ionised gas. Here happens of the ion electron recombination happens.

At first, this motion is negligible compared to the SN's expansion velocity. The position of the photosphere increases linearly in time, i.e. its surface is growing quadratically causing the brightening of the lightcurve. Later on, when the temperature has dropped, the photosphere moves further in towards the slower moving parts of the atmosphere.

It finally recedes in space, when the recombination front reaches those parts of the envelope having a expansion velocity comparable to the velocity of the recombination front. Therefore the lightcurve brightens eventually slower. The decay of the radioactive elements, produced by explosive burning

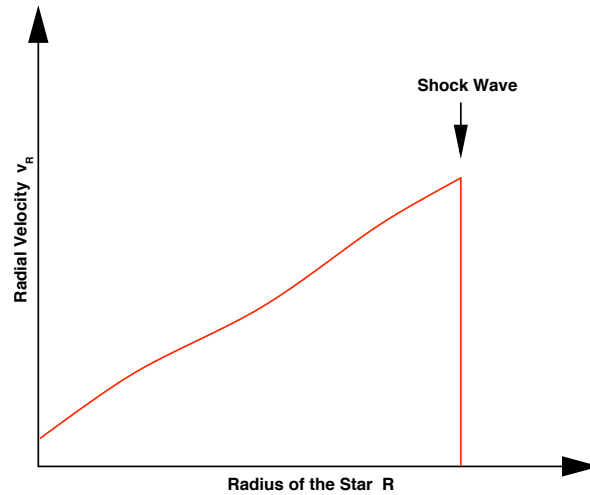


Figure 1.4: Sketch showing an average radial velocity profile of an exploding star.

behind the shock wave during the first seconds of the explosion, stores additional energy in the atmosphere. γ -rays released by the decays Compton scatter at the free electrons of the stellar plasma, thereby, heating the plasma. Each scatter process roughly releases half the rest frame energy of a photon in thermal energy. As the photon diffusion time decreases, the trapping of that radioactive energy is reduced. This increases the luminosity until the amount of energy which is radiated away matches the amount of energy stored by decay. Subsequently the luminosity follows the decay of its radioactive energy source.

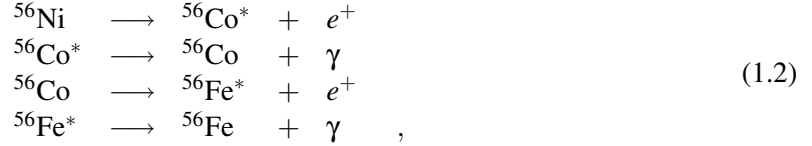
1.3.2 Evidence for Mixing

Modeling the lightcurve of SN 1987A requires two things. First, the opacity which is dominated by metals, i.e. elements heavier than He, has to be smoothed out over the whole stellar envelope, especially over the helium shell and the hydrogen envelope, to explain the overall smooth behaviour of the lightcurve (Figure 1.4, left panel). This can only be achieved if iron group elements are mixed far outwards in the stellar envelope. Secondly, to reproduce the broad 2nd maxima (Figure 1.4, left panel) one has to assume that the inward moving recombination front of hydrogen, the so called hydrogen recombination wave, reaches the deep core of the supernova, thus, hydrogen has to be mixed deep into the core (e.g. Nomoto et al. 1988).

Generally the envelope of an exploding star expands homologous, i.e. the radial velocity is proportional to the radius (Figure 1.4). The star has an onion-like structure. Inside the hydrogen envelope are lying the cores of the elements produced during the thermonuclear evolution embedded in each other (Subsection 2.1.1, Figure 2.1).

The early detection of X- and γ -rays requires mixing of ^{56}Ni and other radioactive elements to the very outer layers of the supernova. Moreover, the maximum of the γ -ray emission of SN 1987A, which is produced by the radioactive decay of ^{56}Co , was observed less than one year after the explosion. This is much earlier than what was expected if no ^{56}Ni was mixed outwards during the explosion of the star. A detailed discussion of that can be found in Arnett et al. (1989b). The decay chain of ^{56}Ni can

be given in the following way



${}^{56}\text{Ni}$ has a half life of $\tau_{1/2}({}^{56}\text{Ni}) = 6.075\text{d}$, and ${}^{56}\text{Co}$ has a half life $\tau_{1/2}({}^{56}\text{Co}) = 77.26\text{d}$ (Pfennig et al. 1995).

Between 20 and more than a hundred days days after the explosion a feature around the $\text{H}\alpha$ P-Cygni profile at around -5000km s^{-1} (March 20) was observed, now known as the ‘‘Bochum Event’’ (Hanuschik & Dachs 1987a,b). It was interpreted as local *depletion of the occupation number due to variations in either density or excitation conditions close to the photosphere* at that time (Hanuschik 1988). This could be explained by clump of stellar matter, having a different density than the stellar envelope and/or exhibiting locally different energy deposition.

Optical speckle interferometric observations indicated a ‘‘very bright’’ source near SN 1987A (Matcher et al. 1987; Nisenson et al. 1987; Meikle et al. 1987). The source was not present prior to the supernova and is now known as the ‘‘mystery spot’’. It appeared around the same time as the ‘‘Bochum Event’’, and had a comparable position in radial velocity space ($\pm 4000 \pm 2000\text{km s}^{-1}$).

Haas et al. (1990) reported from mid infrared spectroscopy of forbidden Fe II lines an expansion velocity for iron of 2000km s^{-1} . However, a single line feature was measured at around 3500km s^{-1} . Using the integrated line flux, they derived the total mass of single ionised iron as $0.026M_{\odot}$.

Note that some evidence of mixing in supernovae was already given by the chemical inhomogeneity of the Cas A SNR (Figure 6.3), as well as the fact that iron was observed at the same velocity as oxygen in the same remnant.

Chapter 2

Field of Research

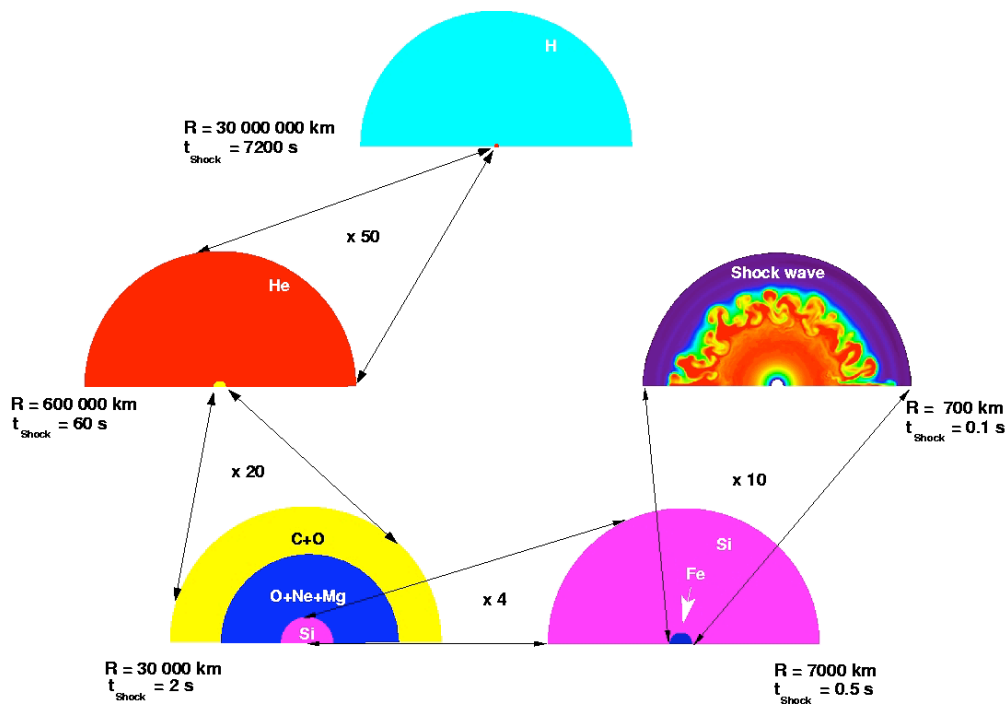


Figure 2.1: Illustration of the length scales and the onion like structure of a presupernova star. The time scale t_{shock} give the times the shock wave needs to travel through that part of the star, respectively. Figure from Kifonidis (2000)

2.1 Core Collapse Supernovae

Massive stars with masses larger than $\sim 8 M_{\odot}$ end their lives with a supernova explosion of type II or type Ib/c. The inner core of the massive star collapses and a compact remnant, either a neutron star or a black hole, is formed. Below $10 M_{\odot}$ the collapsing stellar core is a Ne/Mg/O core. Above $\sim 25 M_{\odot}$, the compact remnant will be a black hole rather than a neutron star. For this work, only the mass range between $10 M_{\odot}$ and $25 M_{\odot}$ is of interest, hence I restrict this overview to that mass range.

2.1.1 Core Collapse and Bounce

At end of their thermonuclear evolution and shortly before they end their lives, massive stars with $\sim 10 - 25 M_{\odot}$ have an onion like structure (Figure 2.1). The inner core of the star, which is mainly made out of iron group elements is surrounded by the silicon core. Further out are following the O/Ne/Mg shell, the carbon oxygen shell, and the helium shell. This complete onion like structure lies deeply embedded in the vast hydrogen envelope of the star. These ‘‘onion’’ shells are separated by burning layers where the star fuses elements of the shell lying outside into elements of the shell lying inside, respectively. At the innermost burning layer, where temperatures are in the order of 4×10^9 K, α particles, produced by thermal desintegration are added successively to ^{28}Si , which at the same time is fused to either ^{56}Ni or ^{54}Fe . This process is adding more and more mass to the iron core.

Finally, the growing iron core reaches a point where the dynamic is speeding up tremendously. The contraction changes into free fall, the core is collapsing (Figure 2.2, upper left panel) and the gravitational binding energy is released in form of neutrinos, which leave the collapsing core instantaneously. When the core density approaches nuclear density ($\rho_{\text{trap}} \approx 10^{12} \text{g/cm}^3$), the mean free path of neutrinos becomes smaller than the size of the collapsing core, and the diffusion time scale of neutrinos (\implies coherent scattering on nuclei) becomes larger than the collapse time scale. The neutrinos are now trapped acting as an additional radiation pressure component (Figure 2.2, upper centre panel). At densities exceeding nuclear density ($\rho \gtrsim 10^{14} \text{g/cm}^3$) the nuclear EOS stiffens significantly. That fact together with the neutrino trapping forces the collapsed core to bounce back launching a hydrodynamic shock wave.

2.1.2 Stalling and Reviving the Shock Wave

Colgate & Johnson (1960) proposed a theory based on the idea of Baade & Zwicky (1934), in which a hydrodynamical shock wave is launched by the core bounce after the stellar core collapse (Subsection 2.1.1). This shock wave was believed to explode the star. But the shock wave moves through the still infalling dens matter of the outer stellar core, i.e. the part of the iron core lying outside the homologous inner part. It heats up the shocked material to high temperatures, loosing huge amounts of its energy mainly by the photodisintegration of heavy nuclei and neutrino emission. This severe energy losses finally cause the shock wave to stall. All numerical models of the past decades agreed in the point that the prompt shock fails to explode the star (see Janka et al. 2007, sec 1.1 and the references therein).

In 1966 Colgate & White realised that there are some problems with the prompt shock model and they proposed an idea whereby the region behind the shock wave is absorbing a small fraction of the vast number of neutrinos emitted by the newly born neutron star by reactions of the type



Colgate & White’s neutrino driven model was criticised, because it had problems to give matching explosion energies, but later the idea was revived, when it was realised that the energy deposition could take up to a few hundred milliseconds (Bowers & Wilson 1982). From that point on the idea got more and more accepted and the following picture for the explosion mechanism of a ccSN emerged with time.

The shock wave which was launched by the core bounce (Subsection 2.1.1) and stalled by the processes mentioned in the beginning of this subsection is then acting like a standing accretion shock, at which the matter still falling in supersonically from the outer parts of the stellar core, is decelerated and then further advected subsonically onto the proto-NS.

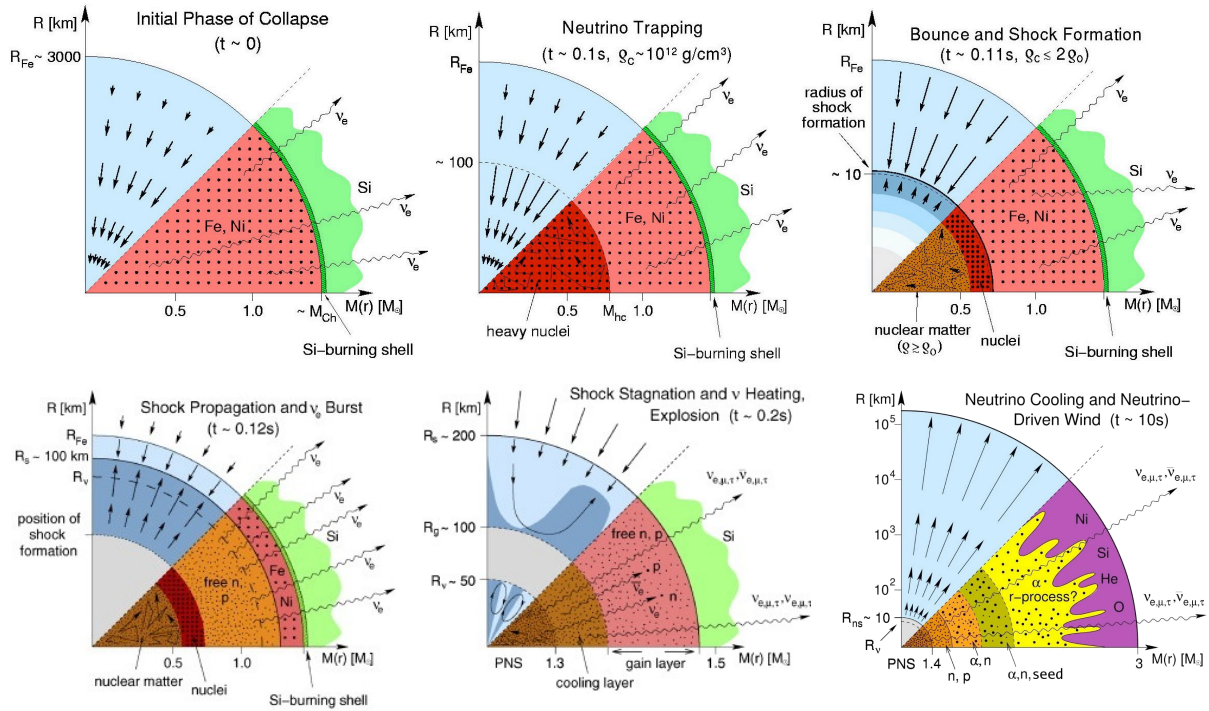


Figure 2.2: Schematic representation of the evolutionary stages from stellar core collapse through the onset of the supernova explosion to the neutrino-driven wind during the neutrino-cooling phase of the proto-neutron star (PNS). The panels display the dynamical conditions in their upper half, with arrows representing velocity vectors. The nuclear composition as well as the nuclear and weak processes are indicated in the lower half of each panel. The horizontal axis gives mass information. M_{Ch} means the Chandrasekhar mass and M_{hc} the mass of the subsonically collapsing, homologous inner core. The vertical axis shows corresponding radii, with R_{Fe} , R_S , R_g , R_{ns} , and R_V being the iron core radius, shock radius, gain radius, neutron star radius, and neutrinosphere, respectively.

Upper left panel: Initial collapse phase — The iron core of the star passes through a rapid contraction phase in which gravitational binding energy is released in form of neutrinos.

Upper centre Panel: Neutrino trapping phase — When the core density approaches nuclear density ($\rho_{\text{trap}} \approx 10^{12} \text{g/cm}^3$) the mean free path of neutrinos becomes smaller than the the size of the collapsing core and the neutrinos' diffusion time scale becomes larger than the collapse time scale, thus neutrinos are trapped.

Upper right panel: Bounce phase — At densities exceeding nuclear density ($\rho \gtrsim 10^{14} \text{g/cm}^3$) the nuclear EOS stiffens vigorously. This and the neutrino trapping force the collapsed core to bounce back, launching a hydrodynamic shock wave.

Lower left panel: Early shock propagation phase — The shock wave launched from the newly born PNS propagates through the outer iron core. Due to severe energy losses by neutrino emission and photodisintegration of nuclei, the shock wave is stalled after having travelled only $\sim 100 \text{km}$.

Lower centre panel: Stalling shock and ν heating — Energy deposition in the cooler layers behind the shock due to absorption and scattering of a small fraction of neutrinos revives the shock wave.

Lower right panel: Neutrino driven wind phase — In the late phase, seconds after the core collapse, is the PNS is thermally cooling by emission of neutrinos, they drive a fast particle wind and provide the conditions for r-process nucleosynthesis. Figures and introduction from Janka et al. (2007).

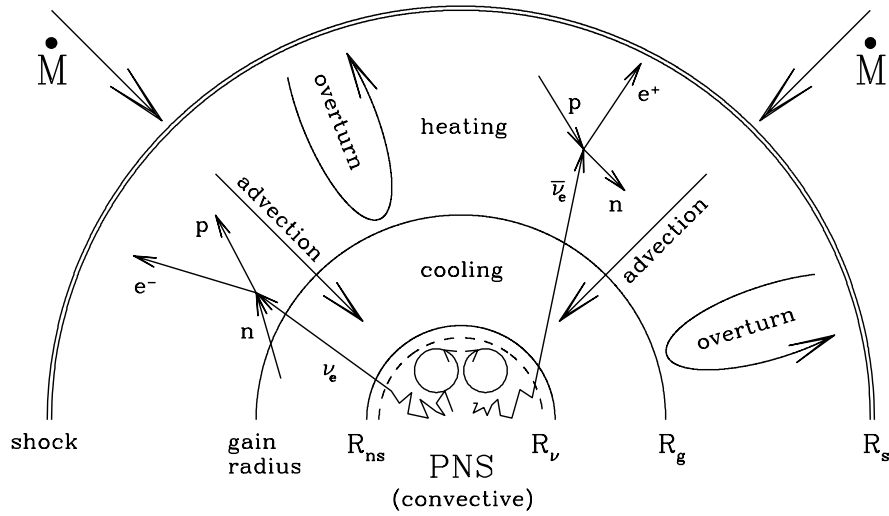


Figure 2.3: Sketch which summarizes the processes that determine the evolution of the stalled supernova shock after core bounce. Stellar matter falls into the shock at radius R_s with a mass accretion rate \dot{M} and a velocity near free fall. After deceleration in the shock, the gas is much more slowly advected towards the nascent neutron star through the regions of net neutrino heating and cooling, respectively. The radius R_{ns} of the neutron star is defined by a steep decline of the density over several orders of magnitude outside the neutrinosphere at R_ν . Heating balances cooling at the gain radius R_g . The dominant processes of energy deposition and loss are absorption of electron neutrinos onto neutrons and electron antineutrinos onto protons as indicated in the figure. Convective overturn mixes the layer between gain radius and shock, and convection inside the neutron star helps the explosion by boosting the neutrino luminosities. Figure and description from Janka (2001)

At the same time a huge amount of the neutrinos originally trapped inside the PNS are diffusing outwards to a region, where the density is low enough that they can freely stream away. There the so called neutrino photosphere is located, which is henceforth acting as the main radiation energy source. However, the hot matter located outside the PNS but inside the so called gain radius, is cooling by neutrino emission and hence acting as an additional radiation energy source. The gain radius (Figure 2.3) is defined at that distance from the center of the star, where the neutrino heating rate per nucleon is equal to the neutrino cooling rate per nucleon. It lies somewhere in the middle between the neutrino photosphere and the shock radius.

This situation has two implications for the shock wave and the region below. Firstly, the matter located below the shock wave and above the gain radius gets heated by the neutrino radiation and starts to expand, pushing the shock wave further out. Eventually, the shock wave reaches the less dense regions of the outer stellar core, which are falling in with much smaller velocities. Then the shock wave gets accelerated by the pressure gradient of the star. The formerly stalled shock wave was revived by neutrino radiation from the inner core.

Secondly, due to the more intense neutrino radiation field near the gain radius the matter there is heated more efficiently than the matter near the shock wave. This leads to a negative entropy gradient. If stellar layer have a negative entropy gradient, i.e. layer lying deeper inside the star are hotter and less dense than those layers on top of them, this stratification may get convectively unstable. A region of neutrino driven convection with rising bubbles of heated matter develops between the gain radius

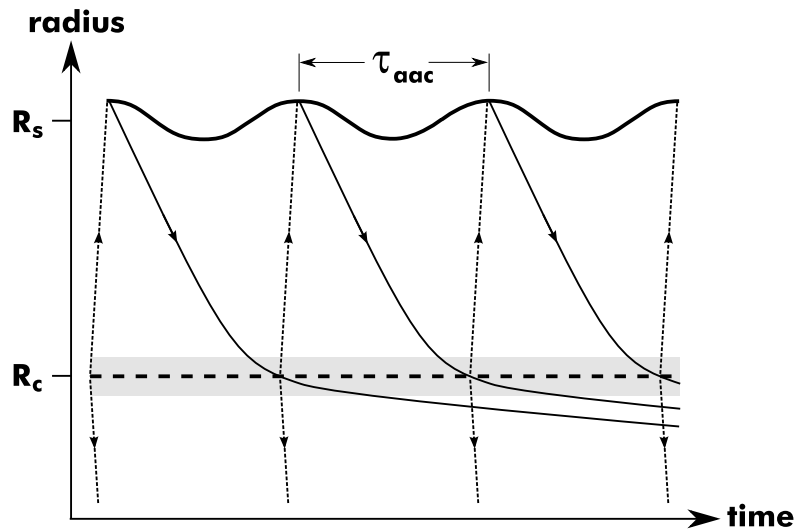


Figure 2.4: Schematic view of the advective-acoustic cycle between the shock at R_s (thick solid line) and the coupling radius, R_c (thick dashed line), in the linear regime, shown for the case where the oscillation period of the shock (τ_{osc}) equals the cycle duration, τ_{aac} . Flow lines carrying vorticity perturbations downwards are drawn as solid lines, and the pressure feedback corresponds to dotted lines with arrows. In the gray shaded area around R_c the flow is decelerated strongly. Figure and description from Scheck et al. (2008)

an the shock radius (Figure 2.2, lower centre panel and Figure 2.3). For this reason this region is known as “hot bubble” region (e.g. Janka & Müller 1996).

The inner parts of the PNS can also become convectively unstable, when the dispersing neutrinos create a negative entropy gradient. This phenomena is known as proto-neutron star convection (Figure 2.2, lower centre panel and Figure 2.3). It is increasing the neutrino luminosity somewhat, however, up to now its impact on the explosion mechanism is still unclear (e.g. Janka & Müller 1996). However, it may produce a significant strong high frequency gravitational radiation signal (e.g. Müller 1997).

In the last decade new dynamic processes like the above discussed neutrino driven convection and new hydrodynamic instabilities like the standing accretion shock instability (Subsection 2.1.3) were discovered, which are of potential importance for the post collapse dynamics of supernovae.

2.1.3 Standing Accretion Shock Instability

The standing accretion shock instability (SASI) may act on the stalled supernova shock wave (Figure 2.2, Subsection 2.1.2). Currently, two different ideas what is causing the unstable behaviour of the standing accretion shock compete with each other: a purely acoustic mechanism (Blondin et al. 2003; Blondin & Mezzacappa 2005) in which pressure waves oscillate in the cavity formed by the shock wave and the so called acoustic advective cycle (Foglizzo 2002; Foglizzo et al. 2007). However, the analysis of Scheck et al. (2006b) are pointing towards the acoustic advective cycle.

When the stalled SN shock wave which acts like an standing accretion shock on the still infalling layers of the collapsing star gets disturbed somewhat, those perturbations are advected towards the

PNS with the accreted matter (Figure 2.3). At the radius where the deceleration has its maximum the perturbations generate sound waves which are travelling through the advected matter upwards to the stalled shock wave and are eventually amplifying the perturbations of the stalled shock wave (Figure 2.4). This process is known as the acoustic advective cycle. The spherical shape of the stalled accretion shock gets unstable and finally, the supernova shock wave gets deformed globally. It turned out that low order modes of spherical harmonics are dominating the instability (Scheck et al. 2008). The globally shock deformation is able to trigger a Richtmyer-Meshkov instability (RMI, Section 5.4) at the He/H composition interface at later times of the explosion when the shock wave is successfully on its way through the stellar envelope. Therefore, it is of particular interest for this work. A detailed discussion of the SASI and the acoustic advective cycle can be found in Foglizzo (2002), (Blondin et al. 2003) and Foglizzo et al. (2007).

2.1.4 The Shock and the Envelope

At a time of 10 s after core collapse the shock wave has reached a radial position at about 10^5 km and is moving with a velocity of 10^4 km s⁻¹. It is finally on its way through the stellar envelope. At that time the still hot PNS is cooling by emission of thermal neutrinos, creating a fast, supersonic particle wind filling the evacuated region behind the shock accelerated envelope matter. At the radial position, where the faster moving wind is hitting the slower moving envelope matter, one finds the wind termination shock. The entropy there is reaching very high values, providing ideal nucleosynthesis conditions (Figure 2.2, lower right panel and Arcones et al. 2007).

The shock wave which is crossing the composition interfaces between the stellar shells (Figure 2.1) is causing the development of hydrodynamical instabilities, i.e. the Rayleigh-Taylor instability (RTI, Section 5.2), the Kelvin-Helmholtz instability (KHI, Section 5.3) and the Richtmyer-Meshkov instability (RMI, Section 5.4).

The growth of RT instabilities at the Si/O and (C+O)/He composition interfaces of the progenitor, seeded by the flow-structures resulting from neutrino-driven convection, leads to a fragmentation of this shell into metal-rich "clumps". This fragmentation starts already ~ 20 s after core bounce and is complete within the first few minutes of the explosion. Around 300 s afterwards these metal-rich "clumps" decouple from the flow and start to propagate ballistically and subsonically through the He core (Kifonidis et al. 2003), mixing heavy elements towards the stellar surface (Figure 2.6, right panel).

When a spherical shock wave crosses the He/H interface and subsequently reaches the hydrogen envelope of the star, it is slowed down strongly. A reverse shock and a dense helium shell is formed, which finally slows down the metal-rich "clumps" significantly (Kifonidis et al. 2003), compared to the observed "clump" velocities in SN 1987A (e.g. Mitchell et al. 2001; Haas et al. 1990). The aspherical shock waves generated in the models of Scheck et al. (2004, 2006b) deposit large amounts of vorticity into the He/H interface layer at times around 100 s, which triggers the growth of a strong RMI (see Kifonidis et al. 2006). The emerging vortices disrupt the He/H interface (compare Figure 2.6 left and centre panel), avoiding the deceleration of the metal-rich "clumps" formed earlier.

The knowledge gained from those studies resulted in some explanations of large scale anisotropies observed in several supernovae (Section 2.2), e.g. SN 1987A (e.g. Hillebrandt & Höflich 1989, Subsection 1.3.2).

More details about the present understanding of supernova physics, about the possible explosion mechanisms and the supernova phenomenology can be found in the reviews of Bethe (1990), Mezzacappa (2005), Kotake et al. (2006), Janka et al. (2007) and in the very comprehensible Nature Physics article by Woosley & Janka (2005).

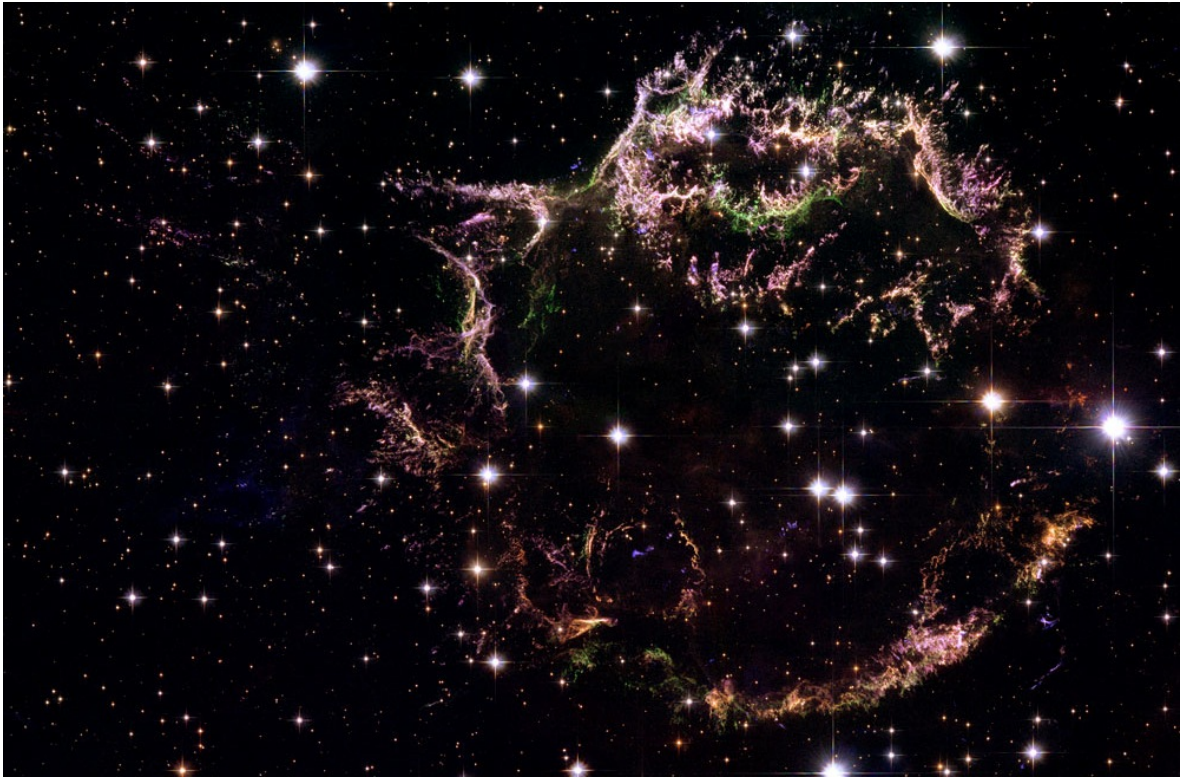


Figure 2.5: A new image taken with the NASA/ESA Hubble Space Telescope provides a detailed look at the tattered remains of a supernova explosion known as Cassiopeia A (Cas A). It is the youngest known remnant from a supernova explosion in the Milky Way. The new Hubble image shows the complex and intricate structure of the star’s shattered fragments. Note that colours denote different elements.

Credit: NASA, ESA, and the Hubble Heritage (STScI/AURA)-ESA/Hubble Collaboration. Acknowledgement: Robert A. Fesen (Dartmouth College, USA) and James Long (ESA/Hubble)

2.2 Evidence for Mixing and Asphericity in ccSNe

The most prominent example for observations pointing towards strong mixing in ccSNe still is SN 1987A (Subsection 1.3.2). Modelling the lightcurve and spectrum of SN 1987A using one dimensional radiation hydrodynamic models required mixing of heavy elements into the supernova envelope (Utrobin 2004; Utrobin & Chugai 2005). Observations of a He I line at 10830 Å more than ten days after the explosion of SN 1987A implied mixing of ^{56}Ni far outwards, where it reionises the matter of the supernova envelope (Fassia et al. 1998). Chevalier & Soker (1989) could explain the polarisation observed for SN 1987A by West et al. (1987) with modelled asymmetric radial flows.

In the last decade one dimensional explosion models comprising artificial mixing of heavy elements provided good fits to observed spectra and light curves of Type Ib supernovae (Shigeyama et al. 1990; Woosley & Eastman 1997). High-velocity oxygen-rich ejecta located outside the iron-rich ejecta in the SNR Cas A suggest “incomplete” mixing of iron group elements into the region above the silicon and sulfur layers, which failed to reach the oxygen layers of the star (Fesen et al. 2006). However, shape and element distribution in both the SNR Cas A (Figure 2.5) and others SNRs

already pointed to asphericity and mixing in core collapse SNe. Furthermore, mid-infrared observations showed evidence for heterogeneous distribution of sulfur and argon, either oxygen burning products, down into the silicate and neon shells (Douvion et al. 1999, 2000).

Spectropolarimetric observations of several lines in the optical and near infrared range show differing polarisation both in angle and strength, suggesting multiple asymmetric components in the ejecta of SN Ic (Kawabata et al. 2002; Wang et al. 2003). Studying the nebula spectra of the SN Ic 2002ap by the means of synthetic spectra Mazzali et al. (2007) found evidence for an oxygen-rich inner core and ^{56}Ni at high velocities, suggesting a highly aspheric explosion especially in the inner parts.

Modelling spectropolarimetric observation of Type II-P and Type IIn SNe at later epochs when the thick hydrogen envelope starts thinning revealed strong evidence for a highly aspheric distribution of the inner ejecta (Leonard et al. 2006, 2001, 2000). Similar results were obtained from spectropolarimetric observation of Type IIb SNe (Maund et al. 2007). Observations of near-infrared He I lines in the epoch between 50 and 100 days after core collapse are pointing towards reionisation of the ejected supernova envelope. (Fassia & Meikle 1999) could explain the observed line characteristics using explosion models including an artificial ^{56}Ni dredge up. The authors further argue that those lines are formed in a clumpy environment. Optical and X-ray observations of young SNRs resulting in velocity maps already pointed two decades ago towards asphericity being a common feature of core collapse SNe (Tuohy et al. 1982; Tuohy & Dopita 1983).

2.3 Earlier Work on Mixing and Asphericity in SN Models

The existence of Rayleigh-Taylor instabilities at the composition interfaces between the heavier elements in the stellar core and the helium shell and between the helium shell and the hydrogen envelope was shown for the first time by Ebisuzaki et al. (1989), using a linear approximation.

Studies of the nonlinear large scale development of Rayleigh-Taylor instabilities in stellar envelopes using numerical methods were carried out by Arnett et al. (1989a), Fryxell et al. (1991), and Müller et al. (1991). In any case they simulated only the upper half-sphere, including the range $0 < \theta < \frac{\pi}{2}$ and assuming rotation symmetry.

Two dimensional simulations following the supernova shock wave from its birth up to several month after core collapse were used to study hydrodynamical instabilities and the mixing of elements for the case of SN 1987A, by means of smooth particle hydrodynamics (SPH) (Herant & Benz 1991, 1992; Herant et al. 1992). Herant & Woosley (1994) made a analogue study, however, using a red supergiant supernova progenitor model.

Hungerford et al. (2003) performed three dimensional smoothed particle hydrodynamic simulations, ranging from 100 s up to 1 yr after core collapse. Their simulation used a piston driven spherical explosion model as input, therefore, neglecting multidimensional effects like neutrino driven convection and RT/KH instabilities at the inner composition interfaces, i.e. all interfaces located inside the stellar helium core. The simulations included parameterised shock asphericity. However, this approach differs significantly from modelling aspherical shock induced by the SASI (Subsection 2.1.3). Moreover, using SPH as hydrodynamics method in that case might not be as suitable as high resolution shock capturing methods, like PPM (Section 4.1).

The most sophisticated simulations of supernova shock propagation through the stellar envelope were carried out by Kifonidis et al. (2003, 2006). They employed the HERAKLES hydrodynamics code which uses the adaptive mesh refinement (AMR) method AMRA (Plewa & Müller 2001). Their second work used axisymmetric input models of Scheck et al. (2004, 2006b), which exhibit large scale

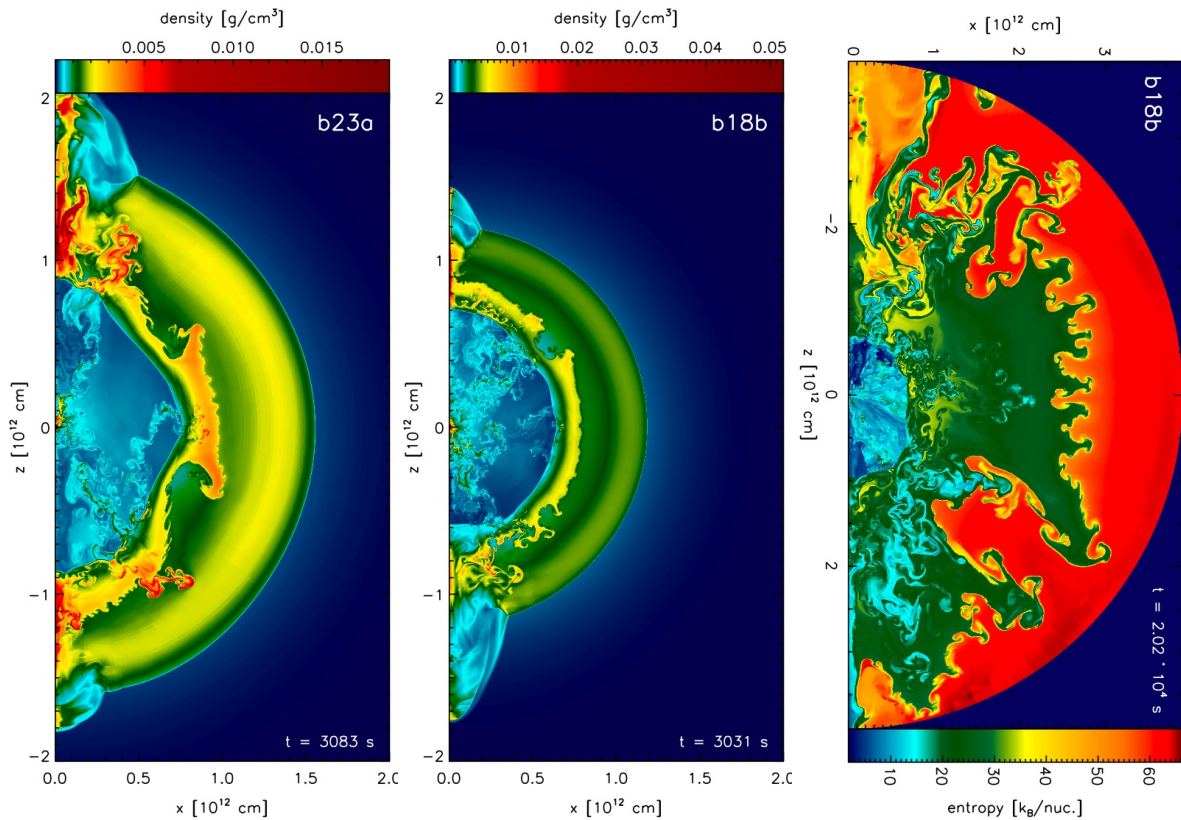


Figure 2.6: Left Panel: Density distribution of model b23a 3 000 s after core collapse. One can clearly see the large vortices generated by the Richtmyer-Meshkov instability at the H/He interface located at $\sim 7.5 \times 10^{11}$ cm.

Centre Panel: Same as the left panel but for model b18b. The vortices mentioned above are not that strong developed yet, indicating a longer growth time.

Right Panel: Entropy distribution of model b18b 20 000 s after core collapse, where the large scale anisotropies have grown to their full extent. One can also recognize the mushroom-shaped Rayleigh-Taylor/Kelvin-Helmholtz “fingers”.

Figures from Kifonidis et al. (2006).

anisotropies leading to hydrodynamic instabilities, namely the combined Rayleigh-Taylor/Kelvin-Helmholtz instability (RTI, Section 5.2 and KHI, Section 5.3), and the Richtmyer-Meshkov instability (RMI, Section 5.4) (Figure 2.6).

Chapter 3

The Designation of this Thesis

Our scientific goal is the investigation of hydrodynamic instabilities in the stellar envelope of core collapse supernovae. Of particular interest is the resulting mixing of hydrogen and heavier elements, e.g. oxygen, nickel, etc., which are synthesised during the progenitor's thermonuclear evolution and during the explosion itself.

In three-dimensional simulations the developing dynamical structures are not restricted by any symmetry assumption, whereas all flow and composition structures have a cylindrical topology, if axis-symmetry is assumed. Scheck et al. (2006a) found distinct differences in the convective pattern and the distribution of up and down flows in 3D explosion models compared to their 2D counterparts. Since the convection pattern acts as a seed for the RT instabilities (compare Section 2.3), we expect significant differences for the stellar envelope dynamics and the mixing processes. The shock wave in a three dimensional model will deposit vorticity, which is not conserved in contrast to the two dimensional case where vorticity is conserved. That will lead to differences in the growth of the RM instability.

For our longterm simulation in three dimensions we will construct the initial model using the three dimensional radiation hydrodynamic models of Scheck et al. (2006a) extended by an stellar envelope for a $15 M_{\odot}$ blue supergiant (Bruenn 1993; Woosley et al. 1988a). This is required because the models of Scheck et al. (2006a) only cover the inner part of the star out to the middle of the C/O shell located at roughly 20 000 km. Scheck et al. (2006a) made the first steps to extend the work of Scheck et al. (2006b) towards 3 dimensional simulations, and their models are the most sophisticated supernova explosion models simulated in 3D so far. Since our project is thought as a step beyond the work of Kifonidis et al. (2006) towards three dimensional models, it was obvious to use the explosion 3D models of Scheck et al. (2006a) as initial models for our 3D simulations.

Part II

Fundamentals

Chapter 4

The PROMETHEUS Code

4.1 Physical Approximations and Numerical Algorithms

The simulations were performed with the PROMETHEUS hydrodynamics code which uses a direct Eulerian solver for the hydrodynamic equations based on the PPM (Piecewise Parabolic Method) algorithm of Colella & Woodward (1984). PPM is a conservative, high resolution shock capturing scheme of second order accuracy in time and third order accuracy for advection in the spatial dimensions. The implementation in our code uses the exact Riemann-solver of Colella & Glaz (1985) which handles a general EOS (equation of state). For this work we make use of a stellar EOS from Timmes & Swesty (2000) (Subsection 4.4.3).

Multifluid flows are treated with the Consistent Multifluid Advection Scheme (CMA) of Plewa & Müller (1999). To reduce the numerical diffusivity of the code a flattening procedure for the interpolated states is included, which was suggested in the Appendix of Colella & Woodward (1984). The appearance of odd-even-decoupling, a numerical instability many Riemann-solvers suffer from (Liou 2000), is prevented by using an approximate HLLC Riemann solver (Einfeldt 1988) for zones located inside a shock, following the idea of Quirk (1994, 1998). More details about PROMETHEUS and the used methods can be found in Kifonidis et al. (2003).

The code uses spherical polar coordinates (r, θ, ϕ) and a non-equidistant (logarithmic) radial grid to resolve the various length scales, which are significantly different in the inner and the outer parts of the star. The code is parallelised using OpenMP and optimised with a good scaling behaviour when making use of a few hundred CPUs (Section 4.2).

Additionally, we use a movable inner boundary to get rid of the smallest innermost grid zones and, eventually, to relax the CFL (Courant-Friedrich-Levy) condition on the time stepping. Due to the non-equidistant (logarithmic) radial grid and the convergence of the radial coordinate lines towards the central coordinate singularity the innermost grid zones are the smallest ones both in radial and angular direction. The CFL condition requires the time step to be smaller than the sound crossing time of the grid zone because physical information can propagate at maximum with the speed of sound. This assures that no interaction of two waves can happen in one zone during a timestep. Therefore, one can relax the restrictions from the time stepping by discarding the innermost radial grid zones. Discarding these zones is physically justified because the shock wave propagates outwards and all hydrodynamic structures grow with radial distance, i.e. the very inner parts of the computational domain are getting less important with time.

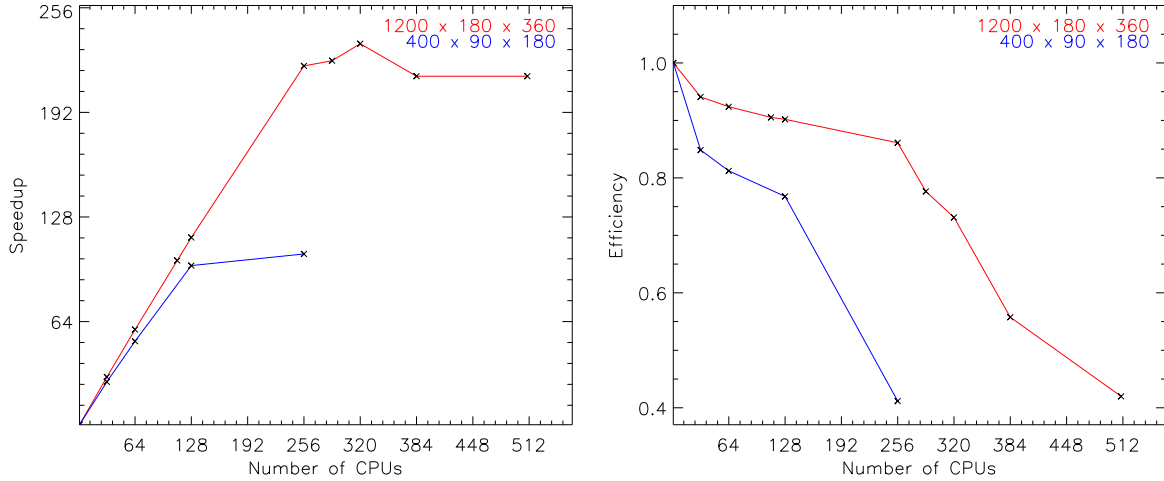


Figure 4.1: Left Panel: Measured parallel SpeedUp for the PROMETHEUS code as a function of grid size and of the numbers of CPUs used.

Right Panel: Same as in the left panel, but showing the measured scaling efficiency. Note that the grid size for **our project** is the larger one.

4.2 Performance, Scaling Behaviour, and the need for HPC Systems

We used a variant of the PROMETHEUS hydrodynamics code, which is optimised for a SGI Altix 3700 Bx2 system. Several changes in the OpenMP parallelisation of the code were made to make optimal use of a larger (>32) number of CPUs and the ccNUMA bus system.

We made several benchmark runs using up to 510 CPUs, i.e. one complete node of the LRZ’s HLRB II SGI Altix 4700 system, to verify the parallel performance of our code and to determine the optimal number of CPUs for our proposed project. In the benchmark, we solved Euler’s hydrodynamic equations on a grid of $1200 (N_r) \times 180 (N_\Theta) \times 360 (N_\Phi)$ zones. The exact scaling behaviour is given in Table 4.1 and Figure 4.1, respectively.

Our code PROMETHEUS has been successfully used on several HPC (High Performance Computing) systems, such as the IBM p690 P4 “Regatta” and the IBM p575 P5 system of the RZG (Rechenzentrum der Max-Planck-Gesellschaft), and the IBM p690 P4+ “JUMP” system at NIC (John von Neumann-Institut für Computing). Since our code is parallelised with OpenMP only, it was merely possible to use up to 32 CPUs (maximum shared memory node size), resulting in run times of months.

LRZ’s HLRB II gave us the possibility to finish our simulations on timescales of weeks, and allowed for three dimensional longterm simulations.

4.3 Computational Setup

The computational grid had 1 200 non-equidistant radial zones. The initial inner boundary was assumed to be at a radius of 200 km. This was necessary because the simulation do not include gravity.

Table 4.1: The scaling behaviour of the hydrodynamics code PROMETHEUS measured on the HLRB II SGI ALTIX 4700 platform using a computational grid of $1200(N_r) \times 180(N_\theta) \times 360(N_\phi)$ zones. The various table entries are: number of processors $nProc$, speedup of the full code with a given number of processors $SpeedUp (total)$, *scaling Efficiency*, i.e. $SpeedUp$ divided by $nProc$.

nProc	SpeedUp (total)	scaling Efficiency [%]
1	1	100
32	30	94
64	59	92
128	115	90
256	220	86
288	224	78
320	234	73
384	214	56
510	214	42

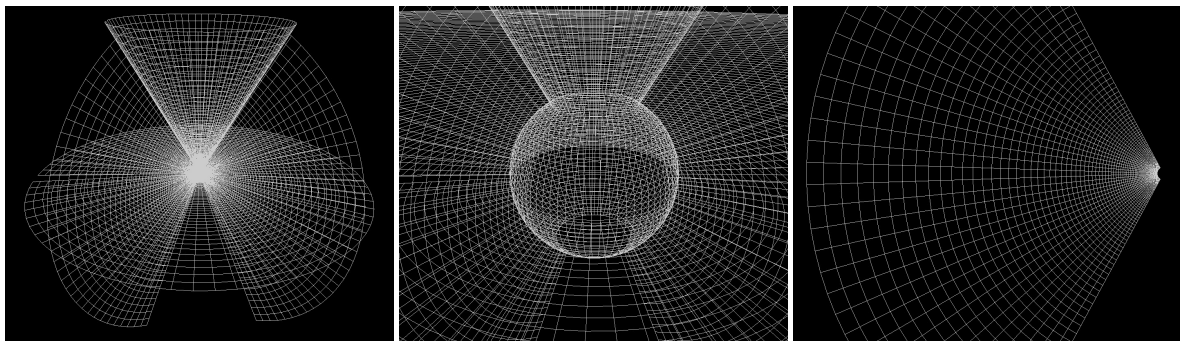


Figure 4.2: Left panel: Computational grid schematise by two $r - \theta - \phi$ plane at $\phi = \frac{3\pi}{4}, \frac{\pi}{4}$, respectively, the equatorial $r - \theta - \phi$ plane and the cone cutted out around the polar axis, as well as the central part cutted out.

Centre panel: Same as left panel, but central part blown up.

Right panel: Single $r - \theta - \phi$ plane of the grid. One can clearly see the logarithmic structure of the radial grid component. Note that for reasons of the presentability only every fifth grid point is plotted.

However, the three dimensional model of Scheck et al. (2006a) includes the outer layers of the PNS, which “explodes” if gravity is omitted. Thus the inner region of the three dimensional models was cut out and the mass was added to the central point mass remaining from the models of Scheck et al. (2006a). Furthermore, the influence of different inner boundary radii on the dynamics and mixing at late epochs was tested using a couple of two dimensional test simulations. It turned out that the late time results are insensitiv to the choice of the inner boundary radius.

The radial grid setup yields a maximum resolution of 2 km at the inner boundary and a resolution of 400 000 km at the outer boundary, located at 39 million km. At the outer boundary free outflow was allowed, whereas reflective boundary conditions were used for the inner boundary. Additionally, the inner boundary was shiftable with time to relax the strict CFL condition (Section 4.1).

In polar direction 180 angular zones were used, distributed equidistant between $0.15\pi < \theta <$

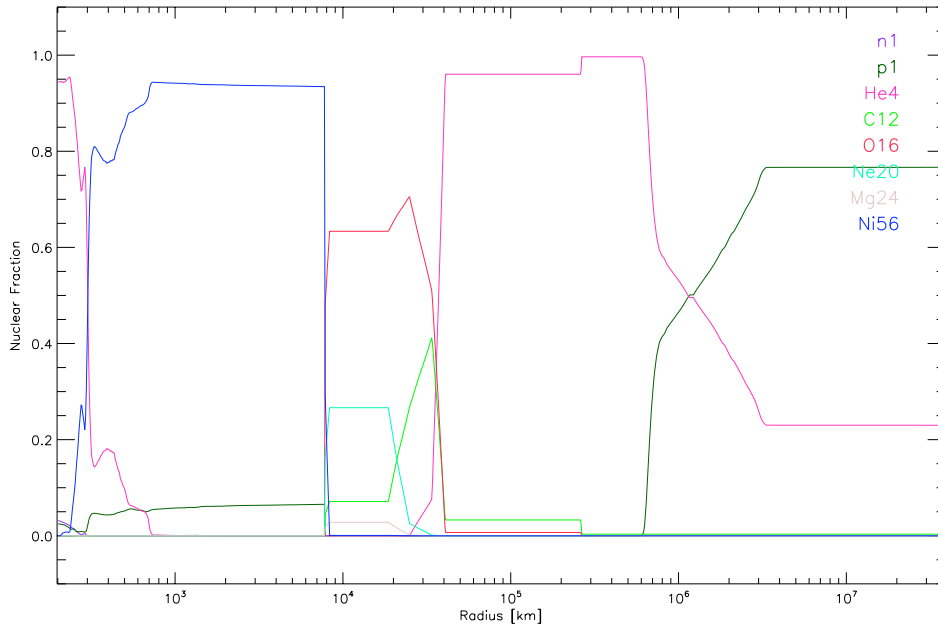


Figure 4.3: Composition of the Initial Model 3D3. Plotted is the fraction of chemical elements as a function of the radius. Note that due to the assumption of a spherical symmetric stellar envelope, this composition is shown in one dimension. Inside of the Shock radius, located roughly at 7 500 km, the composition is not spherical symmetric, but is also a function of θ and ϕ . Note the small fraction of neutrons at $R < 100$ km (purple). Note further that the composition plotted here, is just an example and not representative for the whole 3D domain.

0.85π and reflective boundary conditions are used. In equatorial direction 360 equidistant angular grid zones between $0 < \theta < 2\pi$ are used together with the assumptions of periodic boundary conditions. The resulting numerical grid has a resolution of 1° in both angular directions. Details of the used numerical grid are shown in Figure 4.2

4.4 Initial Models

4.4.1 Model Structure

The initial model for our longterm simulation in three spatial dimensions was constructed using the three dimensional radiation hydrodynamic models of Scheck et al. (2006a) extended by the stellar envelope of a spherical symmetric model of a $15M_\odot$ blue supergiant. This is required since the models of Scheck et al. (2006a) cover only the inner part of the star out to the middle of the C/O shell located at roughly 17 000 km.

Scheck et al. (2006a) used the post-collapse model of Bruenn (1993) as input and applied a random perturbation on the radial velocity field of the their initial model to break the spherical symmetry. Bruenn's model is based on stellar evolution model for a blue supergiant from Woosley et al. (1988a). Unfortunately, Bruenn's model covers only the stellar core and parts of the helium shell and the original stellar envelope was no longer available. In our simulations the progenitor envelope was therefore substituted by a matching envelope model (Woosley, private communication, Kifonidis et al. 2006,

sect. 3).

Scheck et al. (2006a) calculated two 3D radiation hydrodynamic models, one with 2° angular resolution, which reached a final time of 580 ms and one with 3° angular resolution which reached a final time of 1 s. Our model names 3D3 and 3D2 quote the angular resolution of the radiation hydrodynamic model used to create the initial model.

4.4.2 Nuclear Composition

The progenitor model was calculated including nuclear burning by making use of a so called α reaction network. This means one solves only the partial differential equations describing the nuclear reactions of heavy nuclei build up by a of α particles. Those reactions can be written as

$${}^{4x}\text{XX}(\alpha, \gamma){}^{4(x+1)}\text{YY} \quad (x \in [3 - 14]) \quad . \quad (4.1)$$

These nuclei are in detail ${}^{12}\text{C}$, ${}^{16}\text{O}$, ${}^{20}\text{Ne}$, ${}^{24}\text{Mg}$, ${}^{28}\text{Si}$, and ${}^{56}\text{Ni}$. In addition ${}^1\text{H}$ and ${}^4\text{He}$ and the fusion from ${}^1\text{H}$ to ${}^4\text{He}$, as well as the triple α burning from ${}^4\text{He}$ to ${}^{12}\text{C}$ is used. The resulting composition of the progenitor is shown in Figure 4.3.

Scheck et al. (2006a) used a reduced number of species, i.e. protons, neutrons, α particles, and ${}^{54}\text{Mn}$ as the nucleus representative for the heavy element fraction in their simulations to save computational costs. They were mainly interested in the interaction between neutrinos and the stellar matter which can be satisfactory described using those nuclear species. For the important neutrino reactions see Section 2.1.

To combine those two components to a initial mode for our simulations, we decided to keep the nuclear composition of the 3D explosion model inside the shock radius. However, we took the ${}^{54}\text{Mn}$ in the models of Scheck et al. (2006a) and redefined it to ${}^{56}\text{Ni}$ which we assumed as the representative nucleus of the heavy element fraction. Since there was virtual no ${}^{28}\text{Si}$ left outside the shock radius and inside the shock radiues, there was no information about ${}^{28}\text{Si}$ and ${}^{56}\text{Ni}$ available, both nuclei were treated as well as ${}^{56}\text{Ni}$.

The nuclear composition at radii greater than the shock radius, was not taken from the models of Scheck et al. (2006a), but instead, we decided to use the composition as given by the progenitor model. Therefore, we reconstructed the nuclear composition in the region between the shock radius and the outer boundary the models of Scheck et al. (2006a) by interpolating the nuclear composition of the progenitor using lagrangian coordinates derived from its density structure and the lagrangian coordinates derived from from the density structure of the Scheck model.

4.4.3 Thermodynamical Quantities

The density, the temperature, and the velocity are read from the interpolated model, therewith the other required hydrodynamical and thermodynamical quantities are updated in a consistent way using the EOS of Timmes & Swesty (2000), which we used as well for our simulations. It is a electron-positron EOS, which is based on table interpolation of the Helmholtz free energy (Timmes & Swesty 2000). The implemented interpolation scheme guarantees thermodynamic consistency within an temperature range from 10^4 K to 10^{10} K and a density range from 10^{-6} g/cm³ to 10^{10} g/cm³. The EOS furthermore includes contribution to the total pressure of a photon gas component and a gas component, consisting out of the 8 nuclear species included in our in initial model (Figure 4.3).

Table 4.2: Parameter configuration of Models 2D2, 2D80, 3D2, and 3D3. Mass, E_{tot} , and E_{kin} denote the total mass, total energy, and the kinetic energy, respectively. The total energy is defined as the sum of the internal and the kinetic energy. The latter is in addition given for each spatial dimension separately, denoted by upper index as r , θ , and ϕ , respectively. The size of the computational grid is given by the radius inner and outer boundary and the position of the left and right boundary in the angular directions. The last three rows give the number of grid points (n_r, n_θ, n_ϕ) and the relative resolution ($\frac{\Delta r}{r}, \Delta\theta, \Delta\phi$) for each spatial dimension.

Model	2D2	2D80	3D2	3D3
Mass [M_\odot]	15.7	15.7	15.7	15.7
E_{tot} [Bethe]	5.9×10^{-1}	7.8×10^{-1}	5.9×10^{-1}	6.7×10^{-1}
E_{kin} [Bethe]	1.0×10^{-1}	2.1×10^{-1}	6.5×10^{-2}	1.4×10^{-1}
E_{kin}^r [Bethe]	9.4×10^{-2}	2.0×10^{-1}	5.4×10^{-2}	1.3×10^{-1}
E_{kin}^θ [Bethe]	6.1×10^{-3}	7.8×10^{-3}	5.3×10^{-3}	6.1×10^{-3}
E_{kin}^ϕ [Bethe]	0.0	0.0	5.8×10^{-3}	6.9×10^{-3}
R_i [km] / R_o [10^6 km]	200/39	200/39	200/39	200/39
θ_l [π] / θ_r [π]	0.15 / 0.85	0.15 / 0.85	0.15 / 0.85	0.0325 / 0.9675
ϕ_l [π] / ϕ_r [π]	-1 / 1	-1 / 1	-1 / 1	-1 / 1
$n_r / \frac{\Delta r}{r}$ [10^{-2}]	400/(1.07...1.75)	400/(1.07...1.75)	400/(1.32...1.76)	400/(1.07...1.75)
$n_\theta / \Delta\theta$ [$^\circ$]	180 / 0.94	180 / 0.94	180 / 0.70	180 / 0.94
$n_\phi / \Delta\phi$ [$^\circ$]	1 / 360	1 / 360	360 / 1	360 / 1

4.4.4 Energetics

The radiation hydrodynamic models used as input for our simulations, were parameterised in terms of the total neutrino energy loss $\Delta E_{\text{v,core}}^\infty$ given in $\frac{1}{100} M_\odot c^2$ (Scheck et al. 2006a). This means that our model has an energy input of

$$\Delta E_{\text{v,core}}^\infty = \frac{12}{100} M_\odot c^2 = 215 \text{ b} \quad . \quad (4.2)$$

In a large parameter study using 70 two dimensional simulations (Scheck et al. 2006a) this parameter spanned the range from 10 to 21, which means that our initial model is settled in the lower third of this parameter range.

A closer view on the energetics of our models and more detailed discussion will be made in Section 6.2.

4.4.5 Asphericity and Perturbations

Random perturbations on the radial velocity were applied to spherical symmetric initial models of Scheck et al. (2006a) to break the symmetry. In their large parameter study using 70 two dimensional simulations, they were able to show that these randomly applied perturbations lead to the growth of either a dipole or a quadrupole SASI mode, i.e. $l = 1$ or $l = 2$ mode in spherical harmonics, respectively, because those are the fastest growing modes. Their distribution shows further that each mode is present by roughly 50 %.

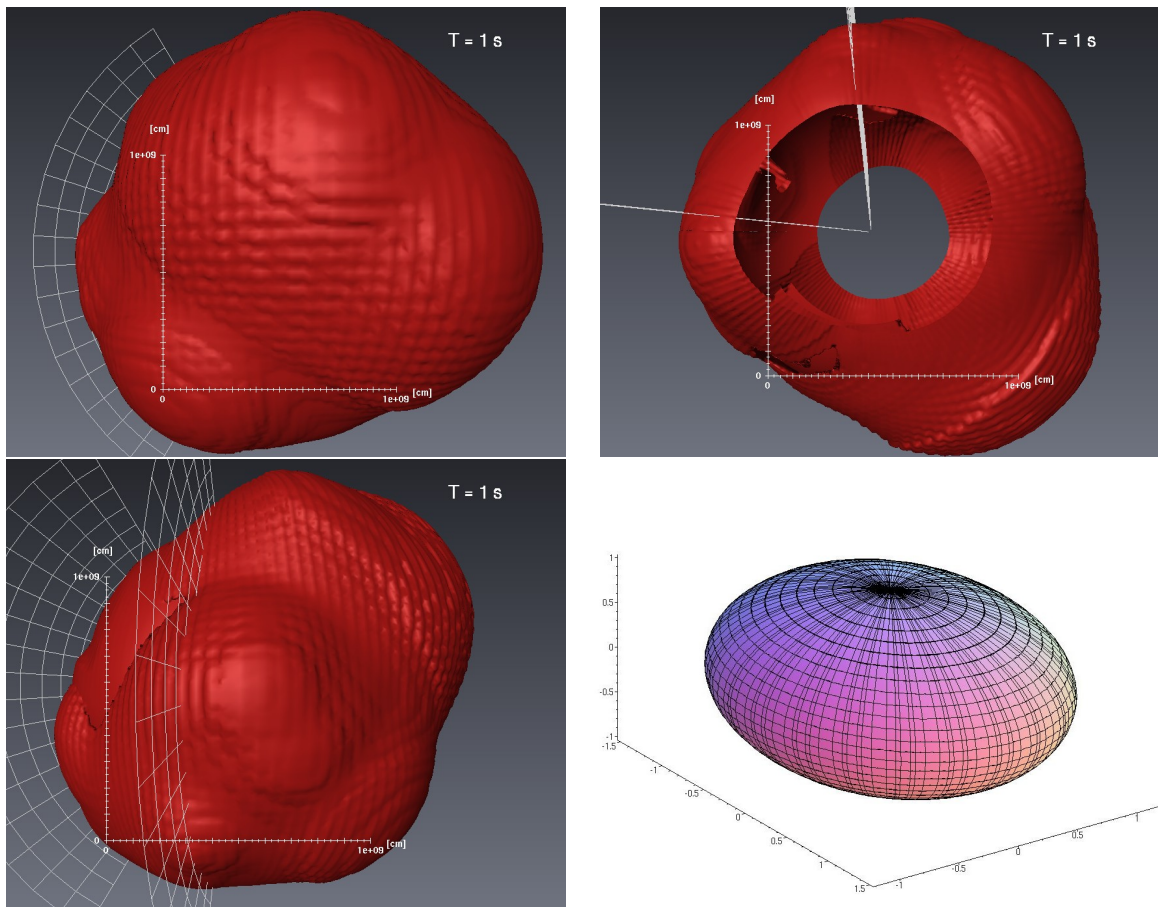


Figure 4.4: Entropy iso-contour representing the shock wave of the initial model 3D3 seen from three different directions. The plotted grid patches denote the slices at $\phi = 2^\circ$ and $\phi = 80^\circ$ which have been evolved as the two dimensional models 2D2 and 2D80. Note that this model shows a $l=1$ mode of the SASI (Subsection 2.1.3), which can be seen best in the upper left plot as a nose in the lower right corner and in the lower right plot as a nose in the upper right corner. The lower left plot shows a tri-axial ellipsoid with an axis ratio of $1.16:1.06:1.00$, however, note that the axis ratio in the plot has been inflated by a factor of three, to make the tri-axial shape of the ellipsoid evidently visible. Note further the small “ripples” on the iso-surface, which is an interpolation artefact.

This implies that our initial supernova models are representative for roughly the half of the aspheric models. However, the discovery of complex modes due to the additional degree of freedom in three dimensions, i.e. a spiral mode given by $l = 1$ and $m = 1$ in spherical harmonics (Blondin & Mezzacappa 2006, 2007; Blondin & Shaw 2007), raises the question how typical our initial models are with respect to that behaviour.

To characterise the deviations of our initial models from the sphericity, we approximated the deformed shock wave by a tri-axial ellipsoid (Figure 4.4). This analysis gives an axis ratio of $1.16:1.06:1.00$ for model 3D3 and an axis ratio of $1.04:1.02:1.00$ for model 3D2. This is a significantly smaller asphericity than the models analysed by Kifonidis et al. (2006), which exhibit asphericities that could be approximated by an ellipse having an axis ratio of $1.5:1.0$.

Note that we used a tri-linear interpolation scheme to map the model of Scheck et al. (2006a) onto our computational grid (Section 4.3, Figure 4.2), which created little “ripples” (Figure 4.4) as an

artefact. However, there is no evidence that this artefact influences the dynamics and the mixing at late epochs.

4.4.6 Comparison Models in 2D

To examine the influence of assuming rotation symmetry and the potential differences between modelling supernova shock propagation in two and three dimensions, we set up two meridional slices (Figure 4.4) of our three dimensional initial model 3D3 as separate two dimensional initial models 2D2 and 2D80 (Table 4.2).

Here meridional slice denotes the following procedure. We selected a single data point in the longitudinal angular or ϕ direction, with a well defined value of the longitudinal coordinate angle ϕ . Then we read all corresponding data points in the radial and the azimuthal angular direction (r, θ) into our two dimensional initial models. However, since vector quantities have only two components in a 2D simulation, the respective third component was neglected, e.g. the ϕ -velocity component. The 2D model names quote the index which denotes the selected data point in the longitudinal direction, i.e. index number 2 and index number 80.

Note that the same procedure was used to select the data sets we used to plot two dimensional “slices” of the three dimensional model 3D3, which correspond to the longitudinal directions of the 2D models. These two dimensional “slices” are used to compare the model 3D3 to our 2D models.

We used the same resolution and the same domain size in the radial and the azimuthal angular direction as for our 3D simulations. However, since the slices represent only a sub-sample of the three dimensional initial model, the physical quantities (Table 4.2), e.g. kinetic energy, are somewhat different for the two dimensional initial models compared to our three dimensional initial model. Moreover, neglecting the third component of the velocity field in the 2D simulations also leads to a somewhat different dynamical behaviour of our models.

Chapter 5

Hydrodynamic Instabilities

The description of the Rayleigh-Taylor instability and the Kelvin-Helmholtz instability which we present in Section 5.2 and Section 5.3, respectively, is based on the review articles from Sharp (1984), Gerwin (1968), and the book from Chandrasekhar (1961). We will describe the basic phenomenology of the two instabilities and we will give a brief outline about how to describe the development and the growth of the instabilities. However, a detailed discussion of the two instabilities is far beyond the scope of this work. The interested reader is referred to the book of Chandrasekhar (1961).

The same holds for the Richtmyer-Meshkov instability, which is described in Section 5.4 based on Brouillette (2002). The interested reader is also referred to the works of Richtmyer (1960) and Meshkov (1969, 1970) in that case.

5.1 Fundamental Equations

The formulation of the fundamental hydrodynamic equations used here, are taken from Müller (2005). The continuity equation describing the conservation of mass is defined in vector notation as

$$\frac{\partial \rho}{\partial t} + \text{div}(\rho \vec{v}) = 0 \quad , \quad (5.1)$$

where ρ denotes the density, t is the time and \vec{v} denotes the velocity in three spatial dimensions. Together with Equation C.3 this leads to the first of the basic hydrodynamic equations in cartesian coordinates

$$\frac{\partial \rho}{\partial t} + \frac{\partial(\rho v_x)}{\partial x} + \frac{\partial(\rho v_y)}{\partial y} + \frac{\partial(\rho v_z)}{\partial z} = 0 \quad . \quad (5.2)$$

Using Equation C.10 instead gives the formulation in spherical polar coordinates

$$\frac{\partial \rho}{\partial t} + \frac{1}{r^2} \frac{\partial(r^2 \rho v_r)}{\partial r} + \frac{1}{r \sin \theta} \frac{\partial(\sin \theta \rho v_\theta)}{\partial \theta} + \frac{1}{r \sin \theta} \frac{\partial(\rho v_\phi)}{\partial \phi} = 0 \quad . \quad (5.3)$$

Note that all variables are given in Cartesian coordinates $X = X(x, y, z, t)$ and spherical polar coordinates $X = X(r, \theta, \phi, t)$, respectively, where r is the radial coordinate, θ the azimuthal angle, and ϕ the polar angle.

The conservation of momentum is described by the Navier-Stokes equation

$$\frac{\partial}{\partial t} (\rho \vec{v}) + \text{div} [\rho (\vec{v} \otimes \vec{v})] + \text{div} \Pi = -\rho \text{grad} \Phi \quad , \quad (5.4)$$

where Π denotes the pressure tensor, which can be written as

$$\Pi = \rho I - \pi \quad . \quad (5.5)$$

Here I denotes the unit tensor and π the isotropic pressure tensor.

Neglecting viscosity the isotropic pressure tensor π is equal zero and one gets the Euler equation which describes the momentum conservation. The Euler equation in vector notation reads

$$\frac{\partial}{\partial t} (\rho \vec{v}) + \text{div} [\rho (\vec{v} \otimes \vec{v})] + \text{grad} p = -\rho \text{grad} \Phi \quad . \quad (5.6)$$

which can be written as

$$\frac{\partial \vec{v}}{\partial t} + (\vec{v} \text{grad}) \vec{v} + \frac{1}{\rho} \text{grad} p = -\text{grad} \Phi \quad . \quad (5.7)$$

When combining Equation 5.7 with Equation C.5 - Equation C.7, the Euler equation can be expressed in cartesian coordinates:

$$\frac{\partial}{\partial t} \begin{pmatrix} v_x \\ v_y \\ v_z \end{pmatrix} + \begin{pmatrix} \frac{\partial V_x}{\partial x} & \frac{\partial V_x}{\partial y} & \frac{\partial V_x}{\partial z} \\ \frac{\partial V_y}{\partial x} & \frac{\partial V_y}{\partial y} & \frac{\partial V_y}{\partial z} \\ \frac{\partial V_z}{\partial x} & \frac{\partial V_z}{\partial y} & \frac{\partial V_z}{\partial z} \end{pmatrix} \begin{pmatrix} v_x \\ v_y \\ v_z \end{pmatrix} + \frac{1}{\rho} \begin{pmatrix} \frac{\partial p}{\partial x} \\ \frac{\partial p}{\partial y} \\ \frac{\partial p}{\partial z} \end{pmatrix} = - \begin{pmatrix} \frac{\partial \Phi}{\partial x} \\ \frac{\partial \Phi}{\partial y} \\ \frac{\partial \Phi}{\partial z} \end{pmatrix} \quad . \quad (5.8)$$

Using the gradient in spherical polar coordinates given in Equation C.12 - Equation C.14, one gets

$$\begin{aligned} \frac{\partial}{\partial t} \begin{pmatrix} v_x \\ v_y \\ v_z \end{pmatrix} + \begin{pmatrix} \frac{\partial v_r}{\partial r} & \frac{1}{r} \frac{\partial v_r}{\partial \theta} & \frac{1}{r \sin \theta} \frac{\partial v_r}{\partial \phi} \\ \frac{\partial v_\theta}{\partial r} & \frac{1}{r} \frac{\partial v_\theta}{\partial \theta} & \frac{1}{r \sin \theta} \frac{\partial v_\theta}{\partial \phi} \\ \frac{\partial v_\phi}{\partial r} & \frac{1}{r} \frac{\partial v_\phi}{\partial \theta} & \frac{1}{r \sin \theta} \frac{\partial v_\phi}{\partial \phi} \end{pmatrix} \begin{pmatrix} v_r \\ v_\theta \\ v_\phi \end{pmatrix} \\ + \frac{1}{\rho} \begin{pmatrix} \frac{\partial p}{\partial r} \\ \frac{1}{r} \frac{\partial p}{\partial \theta} \\ \frac{1}{r \sin \theta} \frac{\partial p}{\partial \phi} \end{pmatrix} = - \begin{pmatrix} \frac{\partial \Phi}{\partial r} \\ \frac{1}{r} \frac{\partial \Phi}{\partial \theta} \\ \frac{1}{r \sin \theta} \frac{\partial \Phi}{\partial \phi} \end{pmatrix} \quad . \quad (5.9) \end{aligned}$$

The conservation of energy is described by the following energy equation in vector notation

$$\frac{\partial}{\partial t} (\rho E) + \text{div}[(\rho E + p)\vec{v}] + \text{div}\vec{h} + \text{div}(\pi\vec{v}) = -\rho\vec{v}\text{grad}\Phi \quad , \quad (5.10)$$

where E denotes the specific total energy, and \vec{h} describes the energy transport by heat conduction. Using Equation C.3 and C.4 together with Equation 5.10 one gets in Cartesian coordinates

$$\begin{aligned} & \frac{\partial}{\partial t} (\rho E) \\ & + \frac{\partial((\rho E + p)v_x)}{\partial x} + \frac{\partial((\rho E + p)v_y)}{\partial y} + \frac{\partial((\rho E + p)v_z)}{\partial z} + \\ & + \frac{\partial h_x}{\partial x} + \frac{\partial h_y}{\partial y} + \frac{\partial h_z}{\partial z} + \frac{\partial(\pi v_x)}{\partial x} + \frac{\partial(\pi v_y)}{\partial y} + \frac{\partial(\pi v_z)}{\partial z} \end{aligned} \quad (5.11)$$

$$= -\rho \left(v_x \frac{\partial \Phi}{\partial x} + v_y \frac{\partial \Phi}{\partial y} + v_z \frac{\partial \Phi}{\partial z} \right) \quad ,$$

and together with Equation C.10 and C.11 in spherical polar coordinates

$$\begin{aligned} & \frac{\partial}{\partial t} (\rho E) \\ & + \frac{1}{r^2} \frac{\partial(r^2(\rho E + p)v_r)}{\partial r} + \frac{1}{r \sin \theta} \frac{\partial(\sin \theta(\rho E + p)v_\theta)}{\partial \theta} + \frac{1}{r \sin \theta} \frac{\partial((\rho E + p)v_\phi)}{\partial \phi} \\ & + \frac{1}{r^2} \frac{\partial(r^2 h_r)}{\partial r} + \frac{1}{r \sin \theta} \frac{\partial(\sin \theta h_\theta)}{\partial \theta} + \frac{1}{r \sin \theta} \frac{\partial h_\phi}{\partial \phi} \end{aligned} \quad (5.12)$$

$$+ \frac{1}{r^2} \frac{\partial(r^2 \pi v_r)}{\partial r} + \frac{1}{r \sin \theta} \frac{\partial(\sin \theta \pi v_\theta)}{\partial \theta} + \frac{1}{r \sin \theta} \frac{\partial(\pi v_\phi)}{\partial \phi}$$

$$= -\rho \left(v_r \frac{\partial \Phi}{\partial r} + v_\theta \frac{1}{r} \frac{\partial \Phi}{\partial \theta} + v_\phi \frac{1}{r \sin \theta} \frac{\partial \Phi}{\partial \phi} \right) \quad .$$

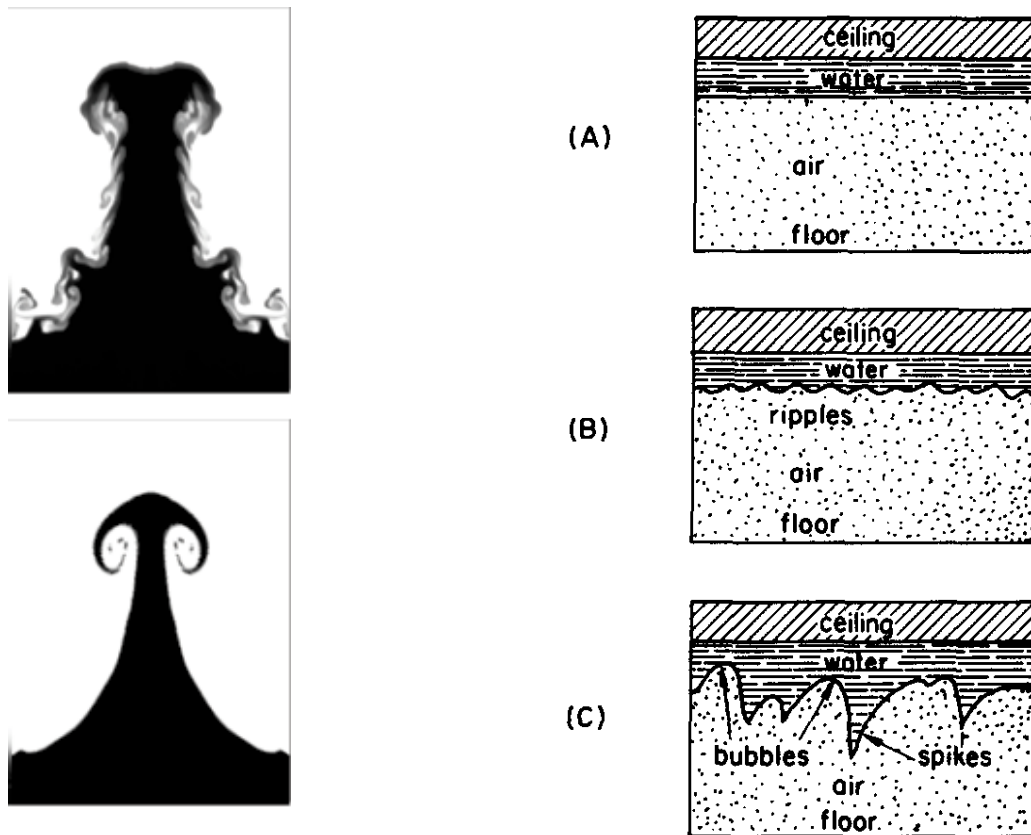


Figure 5.1: Left upper panel: Simulation of the nonlinear growth of a Rayleigh-Taylor Instability (RTI) from an initial perturbation of $\lambda = 200 \mu\text{m}$ using the hydrodynamic code PROMETHEUS with an ideal gas equation of state. Dark shadows of Cu stand out against bright regions of CH_2 . Note that the total effective acceleration is pointing upward in that case.

Left lower panel: Same as right upper panel, using the code arbitrary Lagrangian Eulerian CALE with an tabulated equation of state. Figures and description from Kane et al. (1997).

Right panel: (A) The pressure of air is quite sufficient to support a perfectly uniform layer of water 1 meter thick against the ceiling. (B) But the air pressure can not constrain the air-water interface to flatness. Ripples or irregularities will inevitably be present at the interface. (C) The irregularities grow, forming "bubbles" and "spikes." The water falls to the floor. Figures and description from (Sharp 1984)

5.2 Rayleigh-Taylor Instability

5.2.1 Introduction

The Rayleigh-Taylor instability (RTI) is a fingering instability at the interface between liquids differing in density when the heavier liquid is accelerated towards the lighter one (Strutt 1900; Taylor 1950). The brief description of the Rayleigh-Taylor instability that we give here, is based on the excellent review article by Sharp (1984), and on Chandrasekhar (1961).

We would like to start with an example for a Rayleigh-Taylor unstable configuration (Sharp 1984). Imagine a room with perfectly flat walls and a perfectly flat ceiling. Now place a perfectly plane layer of water, one meter in thickness, directly below the ceiling. The pressure of the air column below the

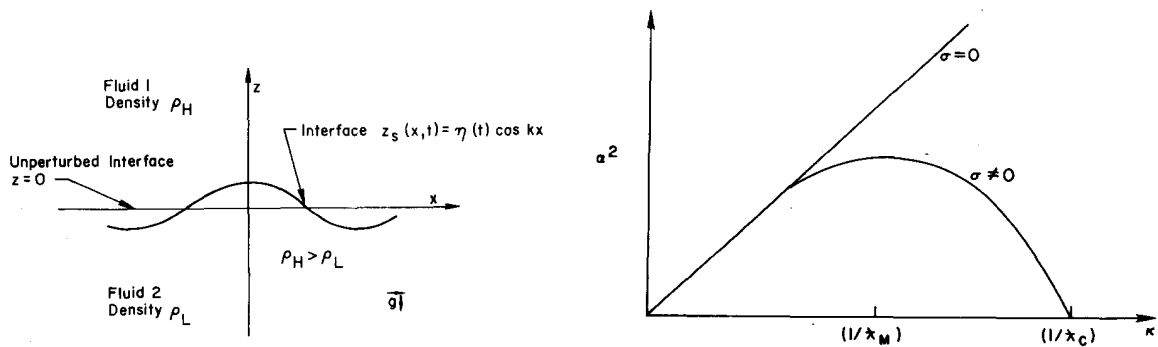


Figure 5.2: Left Panel: Two incompressible fluids of infinite depth, having densities $\rho_H > \rho_L$, meet at an interface. For $t < 0$, the interface is the plane $z = 0$. For times $t \geq 0$, the interface has a perturbed shape. The simple case $z = l(t) \cos(kx)$ is illustrated in the figure.

Right Panel: Schematic plot of the dispersion curve α^2 vs. k (Equation 5.16). Figures and description from (Sharp 1984)

water layer is more than enough to hold a water layer of 1 m in thickness (Figure 5.1,[A]). Remember that the water column equivalent of normal atmospheric pressure is more than 10 m. So from the pressure point of view the configuration should be stable, but the underlying air column fails to keep the interface between the water and the air in perfect planar geometry.

With time going on, the interface will be deformed, eventually having little ripples (Figure 5.1,[B]). Now on the one hand, there are regions which have a larger water column than the average and are supported by the pressure of a smaller air column than required to be in equilibrium. On the other hand, there are regions having smaller water column on top of a larger air column. The larger air column will push the smaller water column further upwards, whereas the region having a larger water column will push the smaller air column beneath it further downwards.

The whole configuration has become unstable and the water will form large fingers penetrating into the air layers (Figure 5.1,[C]) and, finally, falling down onto the floor of the room.

Now imagine the situation, when all the water has reached the floor. It will have the following configuration: a layer of water on top of the floor, 1 m thick and on top of it a large air column, separated by an interface, the water “surface”. If one does not wait too long, there will still be a lot of ripples on the water “surface”, but in contrast to the situation described before, the configuration is stable. Regions with higher water columns will tend to sink back whereas regions with smaller water columns are pushed back by the pressure gradient inside the water layer, towards the average water level. The ripples will only lead to surface or so called pressure waves.

What we have now learned from this quite simple almost everyday example is, that in configurations where the heavier fluid is accelerated towards the lighter fluid, the interface in between the fluids is Rayleigh-Taylor stable. But interfaces where the lighter fluid is accelerated towards the heavier fluid are Rayleigh-Taylor unstable.

5.2.2 Linear Analysis in Plane Geometry

As in the descriptive example above (Figure 5.1, right panel) we assume two inviscid fluids of different density, initially at rest, which meet at a plane interface. Furthermore we assume that a constant acceleration in the direction perpendicular to the interface plane is active. Then the total effective

acceleration \mathbf{G} can be written as

$$\begin{aligned}\mathbf{G} &= (\mathbf{g} - \mathbf{a}) \quad \text{with } \mathbf{g} > 0 \\ &= (g + a)\vec{e}_z = G\vec{e}_z \quad ,\end{aligned}\tag{5.13}$$

where g is the local gravitational acceleration, a an arbitrary acceleration, and \vec{e}_z is the unit vector in z direction, which was chosen to be normal to the interface between the two fluids at $z = 0$. We can suppose that the interface is at rest, but disturbed by perturbation of the form

$$Z_s = \eta(t) \cos(kx) \quad \text{with} \quad \frac{\eta(t)}{\lambda} < 1 \quad .\tag{5.14}$$

It can be shown, e.g. by analysis of the energies, that the amplitude of the perturbations is given by

$$\frac{d^2}{dt^2}\eta(t) = \alpha^2(k)\eta(t)\tag{5.15}$$

(Chandrasekhar 1961) with $\alpha^2(k)$ being

$$\begin{aligned}\alpha^2(k) &= G \left(\frac{\rho_H - \rho_L}{\rho_H + \rho_L} \right) k - \left(\frac{\sigma}{\rho_H + \rho_L} \right) k^3 \\ &= GAk - \left(\frac{\sigma A}{\rho_H - \rho_L} \right) k^3 \quad ,\end{aligned}\tag{5.16}$$

where A is the so called Atwood number

$$A = \frac{\rho_H - \rho_L}{\rho_H + \rho_L} \quad ,\tag{5.17}$$

which measures the normalised ratio of the densities of two fluids. σ is the coefficient of “surface” tension, or more precisely the coefficient of the tension at the interface. If the two fluids initially are at rest, then

$$\eta(t) = \eta(0) \cosh(\alpha t)\tag{5.18}$$

is the solution to Equation 5.15 (Figure 5.2, left panel). From Figure 5.2 one can easily see that perturbations shorter than a critical wavelength

$$\lambda_{crit.} = \frac{1}{k_{crit.}} = \sqrt{\frac{\sigma}{G(\rho_H + \rho_L)}}\tag{5.19}$$

are stable. This is due to the surface tension σ (Equation 5.16). Furthermore, Figure 5.2 also tells one that there is a fastest growing or most unstable wavelength

$$\lambda_{max.} = \frac{1}{k_{max.}} = \sqrt{3\lambda_{crit.}} \quad .\tag{5.20}$$

5.2.3 Linear Analysis in Spherical Geometry

A linear analysis in spherical geometry is more complex than in planar geometry (Subsection 5.2.2). Moreover, due to central convergence in spherical geometry, the whole stratification can already be unstable in case of two identical fluids.

The perturbations can be expanded in Legendre functions

$$\delta R_n(t) = \sum_n a_n(t) P_n(\cos \theta) \quad , \quad (5.21)$$

where $R(t)$ denotes the radius of the unperturbed spherical interface. Therewith, it may be shown that the amplitudes are fulfilling the following relation:

$$\ddot{a}(t) + \left(\frac{3\dot{R}}{R}\right) \dot{a}(t) - \alpha^2(n) \left(\frac{\dot{R}}{R}\right) a(t) = 0 \quad (5.22)$$

with

$$\alpha^2(n) = \frac{n(n-1)\rho_o - (n+1)(n+2)\rho_i}{n\rho_o + (n+1)\rho_i} \quad . \quad (5.23)$$

Here ρ_o denotes the density of the fluid outside the interface, whereas ρ_i denotes the density of the one inside. The dots denote the first and the second derivative with respect to the time, respectively. The mode number of the spherical harmonics, which is used to describe the perturbation, is given by n . Note that for very large R Equation 5.22 will give the same results as the analysis in planar geometry (Subsection 5.2.2), if additionally is assumed that \dot{R} is small ($\dot{R} \ll R$) and the perturbation wavelength is small, too, i.e. $n \gg 1$.

But assuming $\rho_o \rightarrow \rho_i$, we end up with

$$\ddot{a}(t) + \left(\frac{3\dot{R}}{R}\right) \dot{a}(t) - \left(\frac{2\ddot{R}}{R}\right) a(t) = 0 \quad . \quad (5.24)$$

Depending on $R(t)$ Equation 5.24 may have unstable solutions for an interface between two identical fluids. Depending on additional properties like the compressibility and the acceleration history the importance of the classical result, compared to the importance of geometry effects varies heavily. Therefore, the best method to study this problem is to perform numerical simulations in spherical geometry as done in this work (Section 6.5).

There are some works addressing the RTI in the spherical case (e.g. Bell 1951), but due to the behaviour shown above (Equation 5.21 - 5.24), there are no general results like in the planar case (Subsection 5.2.2).

5.2.4 Non-linear Modelling, Numerical Studies and Further Details

The simplest analysis of the non-linear Rayleigh-Taylor problem was done by Fermi (1951), and Fermi & von Neumann (1953). This example is briefly discussed in Sharp (1984). Numerous further non-linear studies, as well as numerical studies of the RTI, were done in the past decades (Sharp 1984, and references therein).

Since the interface between the moving Rayleigh-“finger” and the surrounding fluid at rest is a shear layer, the Rayleigh-Taylor instability is connected tightly to another hydrodynamic instability, the shear instability or Kelvin-Helmholtz instability (Section 5.3).

In Supernova explosion when the shock wave crosses the nuclear composition interfaces the stability criterium can be expressed the following way

$$\frac{\text{grad}(p)}{\text{grad}(\rho)} = \frac{\vec{\nabla} p}{\vec{\nabla} \rho} < \frac{1}{\Gamma} \quad (5.25)$$

(e.g. Benz & Thielemann 1990), where Γ denotes the adiabatic index.

In Chandrasekhar (1961) chapter X. (sect. 90.-99., p 428-480) one may find a description of the phenomenology of the RTI, as well as a mathematical motivated analytic approach, including the discussion of different cases.

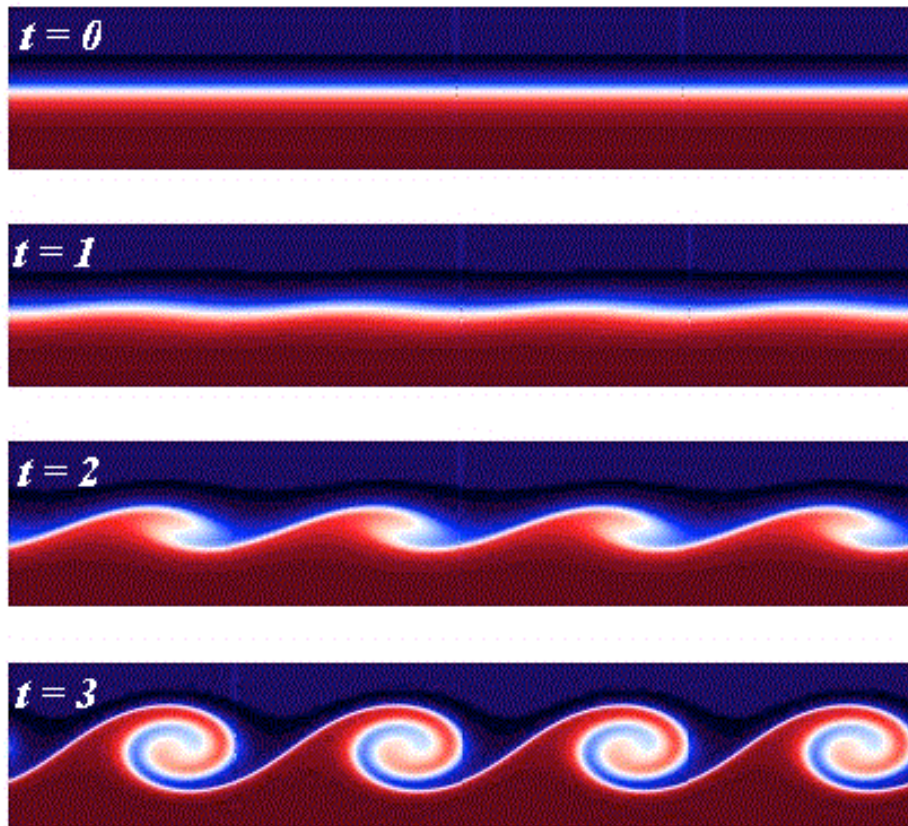


Figure 5.3: The figure shows the development of a Kelvin-Helmholtz wave computed by a 2-D SIMPLE based program with a higher accuracy upwind scheme for convection terms. No turbulence model was used. Richardson number = 0.07, Reynolds number = 300, dimensionless disturbance wavenumber = 0.43, Prandtl number = 0.71. The calculation is carried out in a regular mesh (100x248). Figures and description from Changhong Hu’s web page.

5.3 Kelvin-Helmholtz Instability

5.3.1 Introduction

The Kelvin-Helmholtz instability (KHI) denotes the under certain conditions unstable behaviour of an interface between two fluids which are moving relative to each other parallel to their interface. Helmholtz’s work is basically a description of the instability’s phenomenology. “*Every perfect geometrical sharp edge by which a fluid flows must tear it asunder and establish a surface of separation, however slowly the rest of the fluid may move*” (Helmholtz 1882). Later, in his work Lord Kelvin made an analytical approach to the topic (Kelvin 1910a,b).

The excitation of surface water waves by the wind is one of the most common examples for the KHI and certainly the one most strongly related to everyday life. However, this is only true for wind speeds exceeding a few meters per second. The observed excitation of much smaller waves due to wind speed down to a few centimeters per second cannot be explained by the KHI. They are suppressed by the stabilising effects of surface tension and gravity. Therefore, a theory including more complex wind-shear velocity profiles and resonance phenomena is required (Miles 1957, 1959).

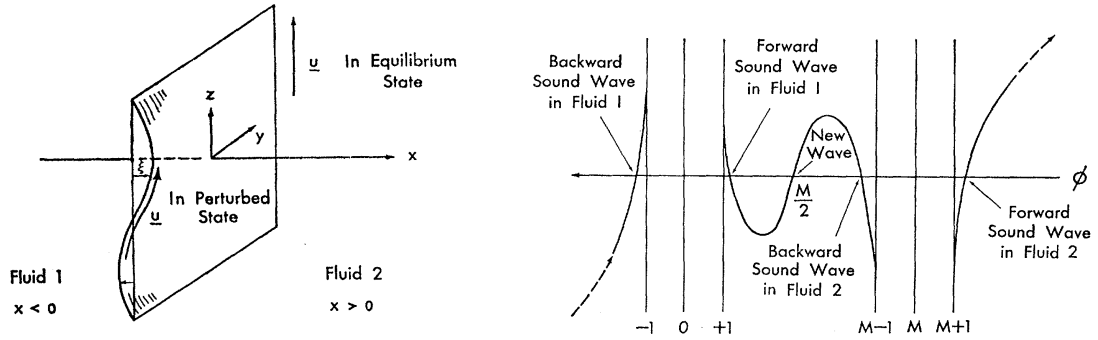


Figure 5.4: Left panel: Geometrical layout for the Kelvin-Helmholtz instability. Right panel: The roots of the dispersion relation $F(\phi) = 0$ (Equation 5.49) for supersonic relative flow ($M > 8^{\frac{1}{2}}$) between two compressible fluids of equal densities and sound speeds. Figures and description from Gerwin (1968).

The following brief description of the KHI is based on the review article from Gerwin (1968). Here we will only discuss the situation for compressible fluids and refer merely to the case of incompressible fluids, since the latter is not relevant for this work (Page 47, for further information see Gerwin 1968).

5.3.2 Linear Analysis of a Compressible Fluid in Plane Geometry

We assume two compressible fluids, fluid 1 located in the space $x > 0$ and fluid 2 in the space $x < 0$, connected by an interface at $x = 0$ lying in the y - z -plane (Figure 5.4). Fluid 2 is moving uniformly with velocity $\vec{u} = (0, 0, u_z)$. Assume further on that all perturbation quantities are independent of x , i.e. they are functions of (y, z, t) , i.e. they are connected via the term

$$e^{i(k_y y + k_z z - \omega t)} \quad , \quad (5.26)$$

where k_y and k_z denote the wave number of the perturbation in y and z direction, respectively and the angular frequency ω measures the time dependence of the perturbation. The density perturbations ρ_2 , the perturbation pressure p_2 and the perturbation velocity \vec{v}_2 of fluid 2 can be expressed by means of the linearised continuity equation (\rightarrow linearising Equation 5.2)

$$\left(\frac{\partial}{\partial t} + u_z \frac{\partial}{\partial z} \right) \rho_2 + \rho \vec{\nabla} \cdot \vec{v}_2 = 0 \quad (5.27)$$

and the linearised momentum equation (\rightarrow linearising Equation 5.8)

$$\rho \left(\frac{\partial}{\partial t} + u_z \frac{\partial}{\partial z} \right) \vec{v}_2 + \vec{\nabla} p_2 = 0 \quad , \quad (5.28)$$

where ρ denotes the equilibrium density. Note that quantities without index denote the equilibrium quantities, assumed to be the same in both fluids.

The equation system defined by Equation 5.27 and 5.28 together with our assumption, can be

solved using the following ansatz for the velocities

$$\vec{v}_1 = \frac{\vec{\nabla} p_1}{i\omega\rho} \quad (5.29)$$

$$\vec{v}_2 = \frac{\vec{\nabla} p_2}{i\omega'\rho} \quad . \quad (5.30)$$

The two angular frequencies (ω, ω') are connected via

$$\omega' = \omega - k_z u_z \quad . \quad (5.31)$$

To solve the problem one further needs “boundary” conditions at the interface. These are the pressure equilibrium

$$p_1 = p_2 \quad \text{at} \quad x = 0 \quad (5.32)$$

and the kinematic condition that the change of the interface displacement $\xi(y, z, t) \sim e^{i(k_y y + k_z z - \omega t)}$ (Figure 5.4) is proportional to the fluid’s velocity components normal to the interface

$$v_1^{(x)} = \frac{\partial}{\partial t} \xi = -i\omega \xi \quad (5.33)$$

$$v_2^{(x)} = \left(\frac{\partial}{\partial t} + u_z \frac{\partial}{\partial z} \right) \xi = -i\omega' \xi \quad \text{at} \quad x = 0 \quad . \quad (5.34)$$

Neglecting the production and the conduction of heat in fluid 2, the total pressure p_2 , the total density ρ_2 and the total velocity \vec{v}_2 are connected by the following equation

$$\left(\frac{\partial}{\partial t} + \vec{v}_2 \cdot \vec{\nabla} \right) \left(p_2 \rho_2^{-\gamma} \right) = 0 \quad , \quad (5.35)$$

which can also be expressed as

$$\left(\frac{\partial}{\partial t} + \vec{v}_2 \cdot \vec{\nabla} \right) p_2 = \gamma \left(\frac{p_2}{\rho_2} \right) \left(\frac{\partial}{\partial t} + \vec{v}_2 \cdot \vec{\nabla} \right) \rho_2 \quad , \quad (5.36)$$

where γ denotes the ratio of the specific heats which are assumed to be identical and constant for both fluids. Linearising Equation 5.36, one ends up with

$$\left(\frac{\partial}{\partial t} + u_z \frac{\partial}{\partial z} \right) p_2 = s^2 \left(\frac{\partial}{\partial t} + u_z \frac{\partial}{\partial z} \right) \rho_2 \quad , \quad (5.37)$$

where s denotes the speed of sound, again assumed to be the same in both fluids:

$$s = \sqrt{\frac{\gamma p}{\rho}} \quad . \quad (5.38)$$

Using the assumption about dependencies of perturbation quantities above (Equation 5.26) and eliminating the velocity and density perturbations from Equation 5.27, 5.28 and 5.37 one is left with the pressure perturbations

$$p_2 \propto e^{(-q_2 x)} \quad \text{for} \quad x > 0 \quad , \quad (5.39)$$

$$p_1 \propto e^{(-q_1 x)} \quad \text{for} \quad x < 0 \quad , \quad (5.40)$$

with the two factors in the exponent

$$q_2 = \sqrt{\frac{k^2 - (\omega')^2}{s^2}} \quad (5.41)$$

$$q_1 = \sqrt{\frac{k^2 - \omega^2}{s^2}} \quad , \quad (5.42)$$

where k is defined by

$$k := \sqrt{k_y^2 + k_z^2} > 0 \quad (5.43)$$

Note that, if q_2 or q_1 are complex, they might go to infinity for x going to infinity. Therefore, one must choose the real part to be positive to prevent this. If, however, the quantities are imaginary the sign of their roots has to be determined using the so-called Sommerfeld radiation condition (Sommerfeld 1949).

Using Equation 5.29, 5.30, 5.39 and 5.40 and applying the “boundary” condition defined by Equation 5.32 and 5.33, one finds the following dispersion relation:

$$\omega^2 q_2 = -(\omega')^2 q_1 \quad . \quad (5.44)$$

Note that this result can easily be adapted the incompressible case, too, where the speed of sound becomes infinite and the exponent factors q_2 and q_1 (Equation 5.41 and 5.42) are both equal to k . This results in the dispersion relation for incompressible fluids (Gerwin 1968):

$$\omega^2 = -(\omega')^2 \quad . \quad (5.45)$$

All the various parameters may be replaced by two relatively simple, dimensionless quantities. The phase velocity ϕ and the effective Mach number M , defined as

$$\phi := \frac{\omega}{k s} \quad (5.46)$$

$$M := \frac{u k_z}{k s} = u_z \cos\left(\frac{\theta}{s}\right), \quad (5.47)$$

with θ being the angle between the fluid velocity \vec{u} and the wave vector $\vec{k} = (0, k_y, k_z)$. The two new quantities may be used together with Equation 5.31, 5.41, and 5.42 to rewrite the dispersion relation (Equation 5.44) in the form

$$\phi^2 \sqrt{1 - (\phi - M)^2} = -(\phi - M)^2 \sqrt{1 - \phi} \quad . \quad (5.48)$$

Assuming ϕ to be real, then Equation 5.41 and 5.42 on the one hand and Equation 5.48 on the other hand contradict each other, if the square roots in Equation 5.48 are real. This leads immediately to the conclusion that they are purely imaginary and must have opposite signs. Using this conclusion Equation 5.48 can be brought into the form

$$F(\phi) = \phi^2 \sqrt{(\phi - M)^2 - 1} - (\phi - M)^2 \sqrt{\phi - 1} = 0 \quad . \quad (5.49)$$

This function is shown in the right panel of Figure 5.4 and describes the behaviour of the KHI. Looking on all of the five real roots shown in Figure 5.4 reveals that q_1 and q_2 are imaginary. Equation 5.39 and refeq-F.28 do vanish for $x \rightarrow \infty$ and the Sommerfeld radiation condition (Sommerfeld 1949) has

to be applied once more. Therewith, one is left behind with the three square roots located near the centre. For M approaching $\sqrt{8}$, the two roots near $+1$ and $M - 1$ approach the one at $\frac{M}{2}$. They become complex conjugates for values of M below the critical value $\sqrt{8}$, and the interface becomes unstable to modes satisfying the conditions above.

In contrast to the result we have obtained by this analysis of the compressible case (Equation 5.45), the interface in the incompressible case is unstable to all modes. This is the major difference between the two cases.

5.3.3 Further Details

For more details and other cases summarised here, the interested reader is referred to Gerwin (1968), and the references therein. A much more detailed discussion of the KHI can also be found in Chandrasekhar (1961) chapter X. (sect. 90.-99., p 428-480), and in the review articles of Blumen (1970) and Howard & Maslowe (1973).

Note that in the invicid case, due to the appearance of the KHI on all length scales, fluid flows showing the RTI, turbulence, etc. should have fractale character (Mandelbrot 1974), however, in numerical simulations the fractale behaviour is severely limited by the numerical resolution (Section 6.1 and Figure 6.1).

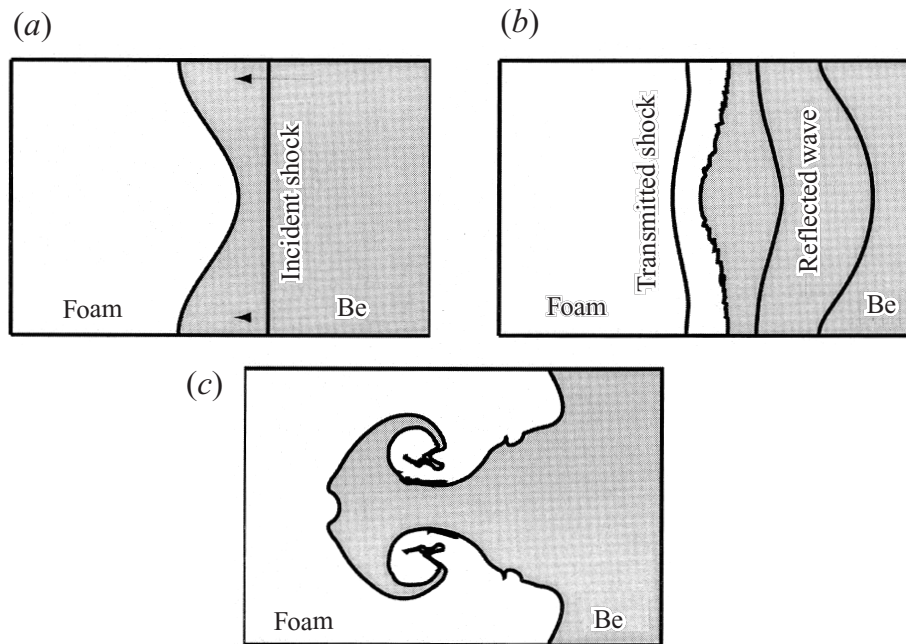


Figure 5.5: Simulation of a RMI experiment at the NOVA laser facility of Lawrence Livermore National Laboratory. (a) A shock wave moves (from right to left) toward the interface between beryllium (shaded) and foam (unshaded). (b) The shock wave has refracted through the interface and deposited vorticity along the interface that will drive perturbation growth. The transmitted shock and the two edges of the reflected rarefaction wave are also shown. (c) Late-time interface showing the characteristic mushroom shape. The transmitted and reflected waves have left the region shown in the figure. Figures and description from Holmes et al. (1999)

5.4 Richtmyer-Meshkov Instability

5.4.1 Introduction

Markstein (1957) first considered the problem of a shock accelerated interface between two fluids. However, the first detailed study of the problem was made by Richtmyer (1960). Later on, Meshkov confirmed experimentally Richtmyer's results, using shock-tube experiments (Meshkov 1969, 1970). The discussion of the Richtmyer-Meshkov instability (RMI) given here is based on the review article by Brouillette (2002).

Assume the following scenario (Figure 5.6, [a] and [b]). Two fluids of different densities ($\rho_1 < \rho_2$) are connected by an interface lying in y -direction of Cartesian coordinates. Furthermore, the interface is perturbed by a small amplitude perturbation of wave length λ . A shock wave travelling along the x -direction gets refracted when passing the interface. The pressure gradient of the shock wave and the density gradient of the interface are not aligned in that case (Figure 5.6, [c]), resulting in the generation of baroclinic vorticity, namely clockwise vorticity in the left part of the interface and counterclockwise vorticity in the right part (Figure 5.6, [d]). This, subsequently, leads to further deformation of the interface (Figure 5.6, [e]). Eventually, the interface will show two vortices in a mushroom-like shape (Figure 5.5, [c]).

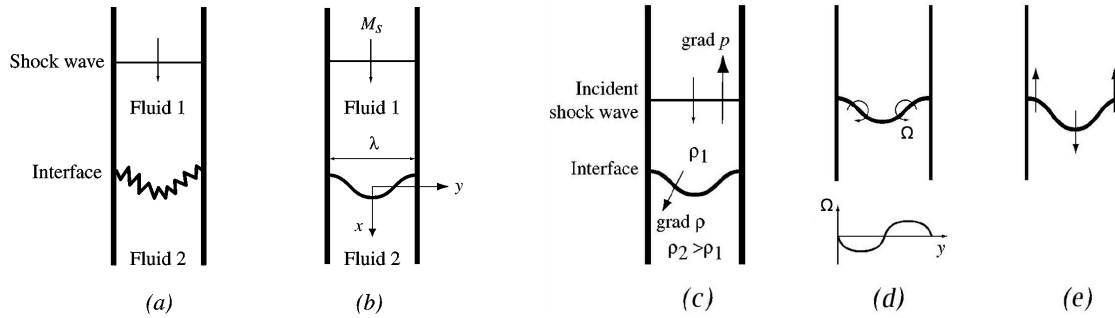


Figure 5.6: Basic configuration for the Richtmyer-Meshkov instability in the rectangular geometry. (a) Discontinuous multimode interface. (b) Discontinuous single-mode interface: initial perturbation given by $\eta(y, t=0) = \eta_0 \cos(2\pi y/\lambda)$. Two fluids, 1 and 2, initially at rest and having different properties (such as density ρ and ratio of specific heats γ , for example) are separated by an interface that has an initial perturbation; a plane shock wave, travelling from top to bottom from Fluid 1 into Fluid 2 is about to interact with the interface (c). Vorticity deposition at a light/heavy interface. (c) Initial configuration. (d) Circulation deposition and intensity of vortex sheet. Ω denotes the z-component of the vorticity $\Omega = \frac{\partial u_y}{\partial x} - \frac{\partial u_x}{\partial y}$ (cf. Equation 6.21 & Equation 6.22). The small figure below shows the vorticity Ω as a function of the y coordinate. (e) Subsequent deformation of the interface. Figures and descriptions from Brouillette (2002)

5.4.2 Impulsive Theory in Plane Geometry

Using the linear formalism of Taylor (1950), the perturbed interface (Figure 5.6, [b]) can be described as

$$y = \eta_0 \cos(kx) \quad \text{with} \quad k\eta_0 \ll 1 \quad , \quad (5.50)$$

which is a single mode sinusoidal perturbation of an arbitrary amplitude η_0 considered to be small. Therewith, the time evolution of the perturbation amplitude is given by

$$\frac{d^2}{dt^2} \eta(t) = k g A \eta(t) \quad , \quad (5.51)$$

using the Atwood number (Equation 5.17) of the preshock situation

$$A = \frac{\rho_2 - \rho_1}{\rho_1 + \rho_2} \quad (5.52)$$

and the perturbation wavenumber

$$k = \frac{2\pi}{\lambda} \quad (5.53)$$

defined by the perturbation wave length λ . Now we replace the constant acceleration used by Taylor (1950) with an impulsive acceleration

$$g = \Delta u \delta(t) \quad , \quad (5.54)$$

where $\delta(t)$ denotes the Dirac delta function and Δu is the change of the interface's velocity due to the shock refraction. Then by time integration of Equation 5.51 one gets the relation describing the impulsive growth rate

$$\dot{\eta}_{imp} = k \Delta u A \eta_0 \quad , \quad (5.55)$$

originally derived by Richtmyer (1960). This is the simplest way to describe the behaviour of a shock accelerated interface between two different fluids.

Although Richtmyer found a good agreement of the order of 5%-10% between this result and the results he obtained by solving the linearised problem numerically, subsequent studies proved that this was due to providential chosen parameters (Brouillette 2002, and references therein).

5.4.3 Linear Compressible Theory in Plane Geometry

The analytic solution for the compressible case of the RMI was derived by Fraley (1986) although the linearised perturbation equations for general fluids were already studied numerically by Richtmyer (1960). Fraley's relation for the linear growth rate in the compressible case reads

$$\dot{\eta}_{\infty} = k \Delta u \eta_0 \left(A + \varepsilon \frac{F}{\gamma_1} \right) , \quad (5.56)$$

where F is defined by the following function

$$\begin{aligned} F &= F(\xi, A) \\ &= \frac{1}{2} \left[(\xi - 1)^2 - 2 \frac{1+A}{1-A} - 2\xi + \frac{2}{\xi} \left(\frac{[1+A]^2}{1-A} + [1-A]\xi^2 \right) \right] \left(\frac{1-A}{\xi+1} \right) \end{aligned} \quad (5.57)$$

and ξ by

$$\xi = \sqrt{\frac{(1+A)\gamma_2}{(1-A)\gamma_1}} . \quad (5.58)$$

γ_1 and γ_2 denote the ratio of specific heats of the two fluids. The factor ε measures the strength of the shock wave, and is defined as (Mikaelian 1994)

$$\varepsilon = 1 - \frac{p_2}{p_0} , \quad (5.59)$$

where p_2 denotes the initial pressure of fluid 2 and p_0 denotes the initial pressure behind the shock wave, i.e. the pressure of the region in front of the reflected reverse shock. For weak shocks $\varepsilon \rightarrow 0$, as Equation 5.56 reduces to Richtmyer's impulsive growth rate relation (Equation 5.55). In case of a vanishing Atwood number $A = 0$, and $z = 0$, the growth rate is also zero, as expected in the case of an interface between two identical fluids. However, if $z \neq 0$, i.e. the case of different fluids having identical densities, perturbations will grow indicating that the RMI is not just a shock driven RTI, despite their similarities.

5.4.4 Spherical Case, Non-linear Theory and Further Studies

In the last 15 years a lot of progress in understanding the RMI was made. People made attempts to study the spherical geometric case (e.g. Meshkov et al. 1997) and steps towards a non-linear analytic theory were taken (e.g. Zhang & Sohn 1996, 1997). Numerical methods were successfully used to study the RMI (e.g. Holmes et al. 1999, Figure 5.5). The experimental approaches became much better, too (e.g. Kane et al. 1997). But, still some discrepancies between the analytic models, the numerical models, and the experimental data remain.

Anyway, although the RMI was initially of interest for the development of thermo-nuclear devices and later on for the research on inertial confinement fusion only, it is nowadays also of interest for astrophysics (Arnett 2000; Kifonidis et al. 2006).

Part III

Simulations in 3 Dimensions

Chapter 6

Analysis of 3D Runs

6.1 Testing the Resolution of Our Setup

To get an estimate for the needed resolution, we performed 2D simulation using the 2D explosion model b23a as input. Having been studied with high spatial resolution using adaptive mesh refinement (Kifonidis et al. 2006), this model is a very good “test case” since the hydrodynamics is well known.

Although, the fine structure of the hydrodynamic flows is somewhat different from that of model b23a in Kifonidis et al. (2006), the larger scales are reproduced very well. One can clearly see the large vortices generated by the Richtmyer-Meskov instability at the H/He interface located at $\sim 10^{11}$ cm / 10^7 km. All large mushroom-like structures generated by the RTI can be identified in our test model b23a, as well. The position and the shape of the reverse shock, generated by transmission of the supernova shock wave through the H/He interface is reproduced quite well. Even the overall shape of artificial “axis”-features are the same.

These results demonstrate that our computational setup provides enough spatial resolution to follow the dynamics of a supernova envelope. However, the absence of a RMI at the H/He interface (Section 6.5) in our 3D model 3D3 give rise to the question if the radial resolution we chose guided by the numerical costs, was not enough to resolve the asphericity of our models at late epochs.

6.2 Energetics and total Mass

6.2.1 Energy of the Explosion

Explosion energies of supernovae are usually of the order of 10^{51} erg (1 b) (Kasen & Woosley 2008). The explosion energy of supernova models is defined generally as the sum of internal, kinetic and gravitational binding energy. Our simulations was performed neglecting gravity, which makes it difficult to state an accurate value for the explosion energy of our models. To estimate a value for the explosion energies of our models 3D3 and 3D2, we calculated the binding energy of the progenitor’s envelope lying outside the shock wave and subtracted it from the sum of internal and kinetic energy, because at least this amount of energy is required to explode the star.

Using that approach we can estimate that the models 3D3 and 3D2 have a explosion energy of 0.65 b and 0.49 b, respectively (Figure 6.3). This indicates that the models are sub-energetic by roughly a factor of 1.5 and a factor of 2, respectively. However, estimating the energy reservoir of a SN, using a typical NS mass of $1.4 M_{\odot}$ (Stairs 2004), a NS radius of 15 km (e.g. Link et al. 1999; Rutledge et al. 2001; Trümper et al. 2004), and the expression for the total gravitational binding energy

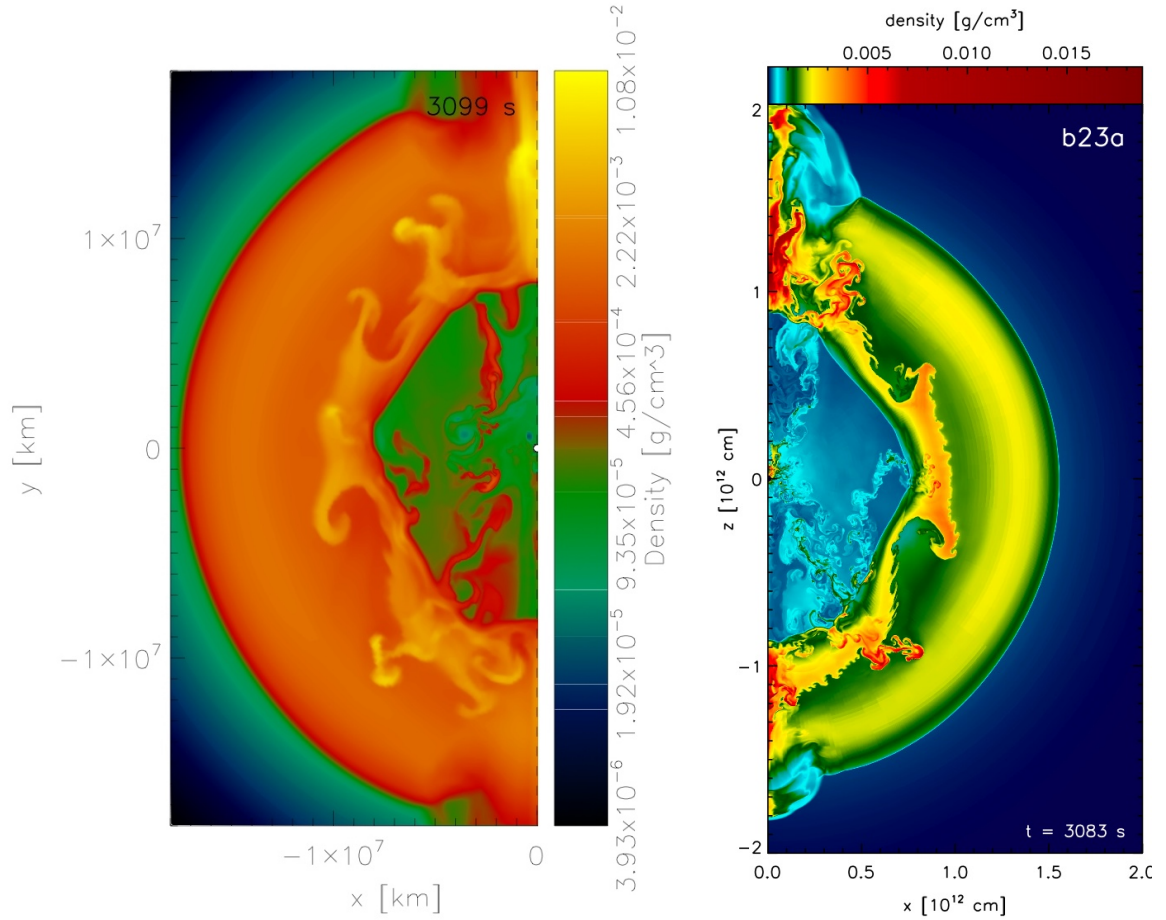


Figure 6.1: Density distribution of model b23a 3000 s after core collapse. One can clearly see the large vortices generated by the Richtmyer-Meskov instability at the H/He interface located at $\sim 10^{11}$ cm / 10^7 km.

Left Panel: Two dimensional simulation performed with the same basic setup and the same resolution as our three dimensional longterm simulation.

Right Panel: Two dimensional simulation by Kifonidis et al. (2006) making use of adaptive mesh refinement. A lot of fine hydrodynamical structures are resolved, especially the small structures created by the Kelvin-Helmholtz instabilities on top of the vortices created by the Richtmyer-Meshkov instability, and the fingers created by the Rayleigh-Taylor instabilities.

of a NS given in Scheck et al. (2006a)

$$E_{\text{bind}} = 3 \times 10^{53} \left(\frac{M_{\text{NS}}}{M_{\odot}} \right) \left(\frac{R_{\text{NS}}}{10 \text{ km}} \right)^{-1} \text{ erg} \quad , \quad (6.1)$$

gives a total amount of energy released during the core collapse of 280 b. After one second the total energy which was radiated away by the models of Scheck et al. (2006a) is roughly 25 b. This means there is still ten times more energy store inside the neutrino radiation source than has been radiated away up to that time and which potentially could contribute to the explosion energy.

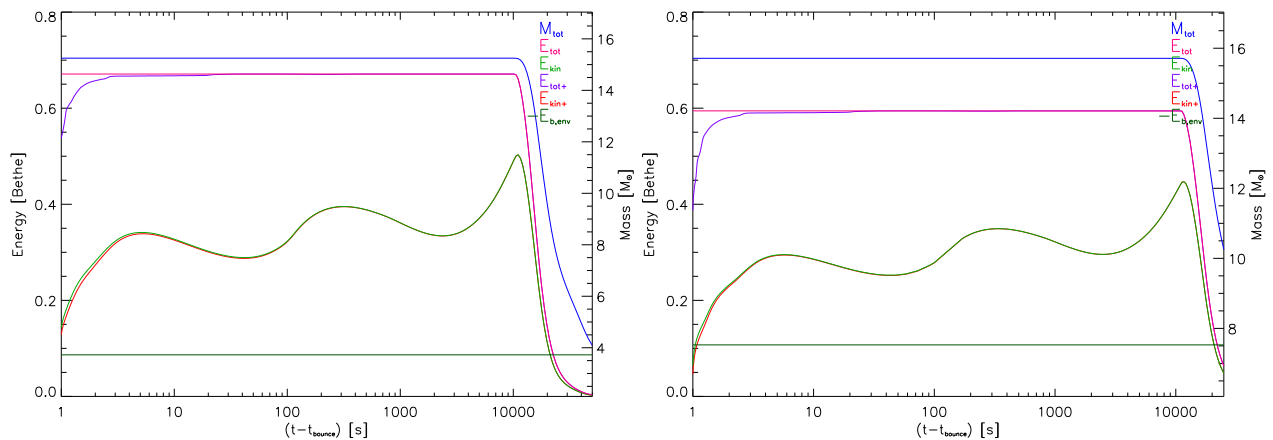


Figure 6.2: Plot showing the evolution of the total energies (magenta) with time of the model 3D3 (left panel) and 3D2 (right panel). Furthermore, the total mass (blue) is plotted, to indicate when the expanding star is leaving the computational grid. The flat dark green line at the bottom represents the negative binding of the envelope. As inner radius for the integration of the gravitational potential the mean shock radius at 1 s was chosen. The quantities indicated with a + are integrated accounting only for fluid elements, having a positive radial velocity.

6.2.2 Saturation of the Explosion Energy

Arcones et al. (2007) performed spherical symmetric radiation hydrodynamic supernova simulations spanning the range from milliseconds after the core collapse up to 10 seconds. Their analysis showed that the models M15-l1-r1 and M15-lt1-r4 gained up to 25% more explosion energy in the time range from 1 to 3 seconds after the core collapse. This suggests strongly that the explosion models of Scheck et al. (2006a) are not saturated with respect to the explosion energies. Guided by the energetic argument and the results of Arcones et al. (2007) it would be preferable to run the supernova simulation up to a few seconds including neutrino radiation and then continue with a purely hydrodynamic simulation.

The first thing one recognises when plotting the kinetic energy is the growth and the wave-like structure of kinetic energy. The kinetic energy is growing because the shock wave is accelerating when propagating down the pressure/density gradient. The wave-like structure can be linked to the flattening and steepening of the gradients (Figure 6.3) due to the onion-like composition structure of the progenitor (Figure 2.1). The density of the stellar envelope follows roughly $\rho \propto r^{-n}$ with $n = 3$ (Figure A.2). Therefore we can express the gradient through the slope of the density profile. The shock wave, which is bearing the most of the kinetic energy, gets decelerated when running through the flatter gradients ($n < 3$) in the middle of the helium and hydrogen composition shells and it accelerates more when reaching the step gradients ($n > 3$) at the composition interfaces and at the outer parts of the hydrogen envelope. We estimated the “position” of the maximum of the kinetic energy used in Figure 6.3 by searching the grid cell with the largest value of the kinetic energy.

6.2.3 Conservation of Mass

Additionally, Figure 6.2 shows the total mass of the models versus time. The total mass stays constant during the first 10^4 s, indicating that the mass loss due to the cutting of the inner boundary (Section 4.1) is negligible. At around 10^4 s the shock wave reaches the outer boundary of our computational grid. That is why the kinetic energy peaks around that time. The stellar envelope starts to expand and a large

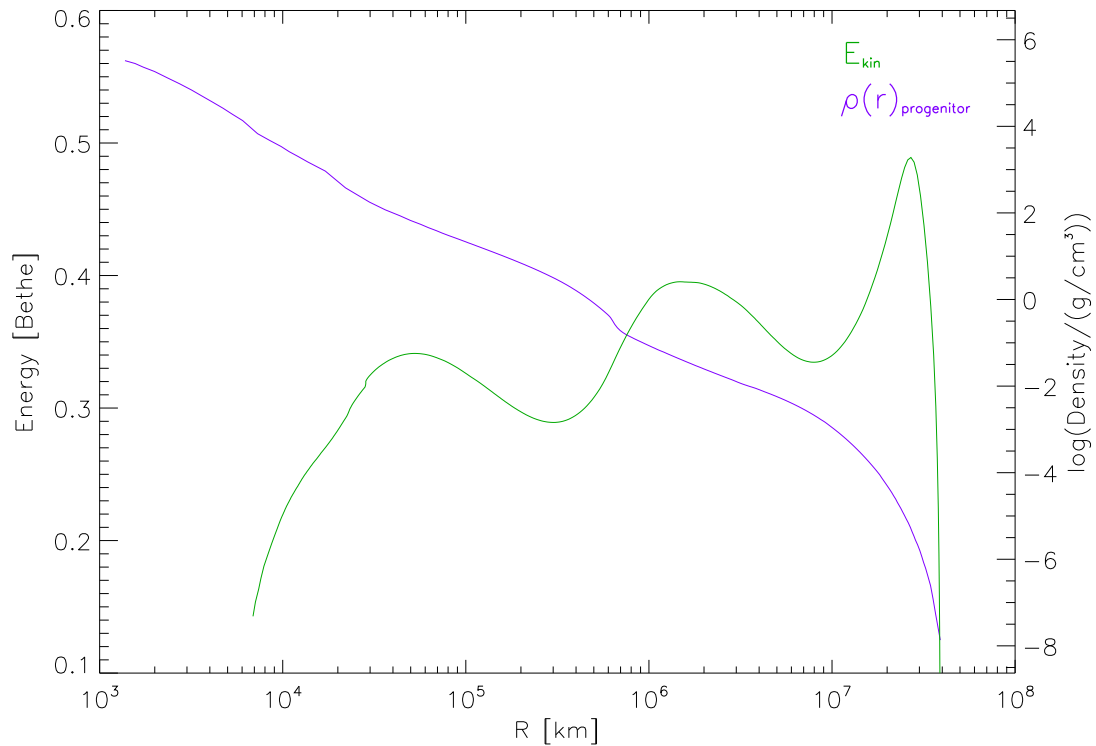


Figure 6.3: Density structure of the supernova progenitor versus radius and kinetic energy carried by the shock wave versus the position of the shock wave.

fraction of the hydrogen shell and subsequently other composition layers leave the computational domain through the outer boundary. The total mass, the internal energy and the kinetic energy of the model drop significantly.

6.3 The Rayleigh-Taylor Instability in 3 Dimensions

When looking at the developing Rayleigh-Taylor “fingers” one recognises, that the flow structures in our three dimensional model 3D3 are similar in size to those found in previous two dimensional simulations (Kifonidis et al. 2006, 2003).

However, all flow structures appear “rounder” and have less fine structure. This is simply because of the much lower radial and angular resolution of the 3D simulations compared to the 2D studies. Remember that the AMR grid used by Kifonidis et al., had already a resolution, without the additional mesh refinement levels, of 0.25° in angular direction and 4 000 logarithmically distributed radial zones. Thus the 2D simulations had a resolution more than four times better than in our computational setup (Section 4.4).

Table 6.1: Total masses of the nuclear species included in our models 3D3 and 3D2.

Nuclear Species	Mass M_i [M_\odot]	Mass fraction M_i/M_{tot}
^1n	6.62×10^{-6}	4.25×10^{-7}
^1H	8.14	0.52
^4He	5.42	0.35
^{12}C	1.19×10^{-1}	7.60×10^{-3}
^{16}O	1.84×10^{-1}	1.18×10^{-2}
^{20}Ne	4.69×10^{-2}	3.00×10^{-3}
^{24}Mg	4.88×10^{-3}	3.13×10^{-4}
^{56}Ni	1.69×10^{-1}	1.09×10^{-2}

Model 3D3 proves that the structures created by the neutrino driven hot bubble convection (Subsection 2.1.2) and by the SASI (Subsection 2.1.3), are acting as seeds for the RTI (Section 5.2), which develops at the various composition interfaces of the stellar envelope (Figure 2.1), especially at the H/He interface. Comparing the surface of the deformed shock wave in our initial models (Figure 4.4) with the time series plots showing the evolution of the density and entropy distribution of model 3D3 (Figure A.5, A.8) reveals that the “nose” originating from the SASI and the prominent fast moving clump of heavy elements (Figure 6.4) which could be identified at late epochs, coincide in their azimuthal and longitudinal directions. It is most likely that the upflow connected with the $l = 1$ SASI mode (Subsection 4.4.5) in the 3D models of Scheck et al. (2006b) which generated the “nose”, is the seed of this “super clump”.

The fast moving clumps penetrate the H/He composition interface without difficulties. The slow down of these clumps due to the passage of the reverse shock, which forms below the H/He interface, is only marginal (Figure 6.5, 6.13). This finding contradicts the results of Kifonidis et al. (2003) and maybe due to the smaller cross section of the smaller heavy element in the 3D case (Subsection 6.4.2). Note that, the interface is partially disrupted through the clumps acting like “cannon balls” (Figure 6.13).

6.4 Metal Velocities and Masses

6.4.1 Mass fractions of chemical species in Radial-Velocity Space

We took the value of the hydrodynamic variables of every grid cell and sorted them into velocity bins of 100 km s^{-1} width using the radial velocity value associated with the grid cell. Subsequent to that, we volume-integrated the density of all cells within a radial velocity bin to get the contained mass. Finally, we plotted the so defined mass distribution versus the radial velocity (Figure 6.5).

The total mass of ^{56}Ni contained in the fastest moving clumps can be estimated to be roughly $2 \times 10^{-3} M_\odot$ (Figure 6.4). As ^{56}Ni traces all nuclear species heavier than ^{24}Mg in our models, the actual amount of radioactive ^{56}Ni mixed outwards in the explosion is significantly smaller. Anyway, there is still enough radioactive ^{56}Ni mixed outwards to provide an explanation of observed phenomena which are associated with clumps of radioactive species (Subsection 1.3.2, Section 2.2).

Haas et al. (1990) derived from observation of SN 1987A a total mass of $0.026 M_\odot$ of single ionised iron moving at a mean velocity of 2000 km s^{-1} (Subsection 1.3.2). This translates to a mass

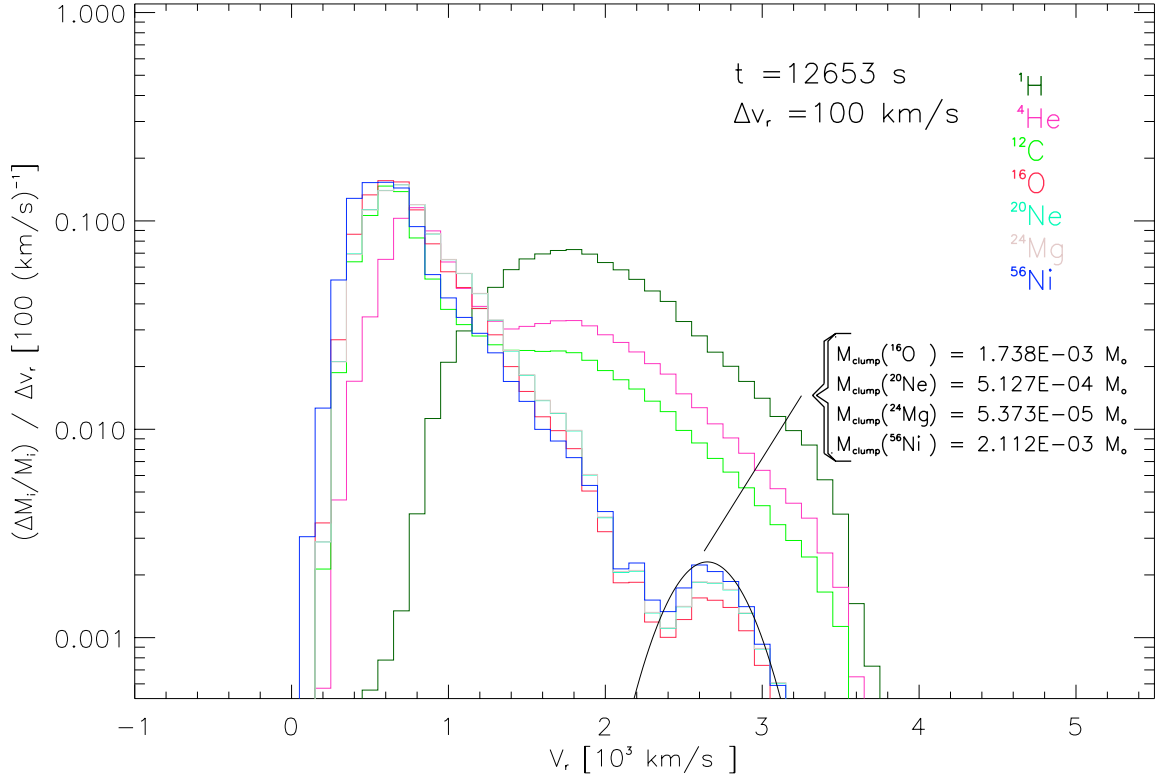


Figure 6.4: Blow up of the last panel in Figure 6.5. The black Gaussian marks a fraction of fast metal clumps which can also be seen in Figure A.5 and A.8. The associated metal masses are given inside the plot in units of solar masses.

fraction of 0.15 of ^{56}Ni (Table 6.1), which we used as a representative nucleus of the iron group (Subsection 4.4.2). Comparing that to the velocity distribution of ^{56}Ni in Figure 6.4 shows that the explosion energy of our model 3D3 is to low (cf. Subsection 6.2.1) to reproduce this observation, since there is not enough ^{56}Ni moving with such high velocities. A larger explosion energy would extend the velocity distribution to higher velocities.

Note that our models are containing a fraction of debris neutrons (Figure 4.3), which are mixed outwards in our simulation. These free neutrons actually would be involved into various kinds of nucleosynthesis processes (e.g. Woosley et al. 2002, sect. VIII and the references therein), which are neglected in our simulations.

When our two models, 3D3 and 3D3 are compared with each other in the radial velocity space (Figure 6.5, A.13), the former model does develop fast moving heavy element clumps, whereas the latter does not. This is not surprising since the velocity maximum scales with the explosion energy as

$$v_r^{\max} \sim \sqrt{E_{\text{exp}}} \quad , \quad (6.2)$$

which can be derived by setting the explosion energy equal to the kinetic energy $E_{\text{kin}} = \frac{1}{2}mv^2$, and which is approximately 10% larger in model 3D3 (Figure 6.2).

These heavy element clumps are forming between 10 and 20 seconds after core collapse and occupy a fraction in the radial velocity space (Figure 6.5), which is clearly separated from the rest of the heavy elements having a continuous velocity distribution. The formation period of these clumps indicates that they are already formed by the RTIs (Section 6.3, 5.2) developing at the composition

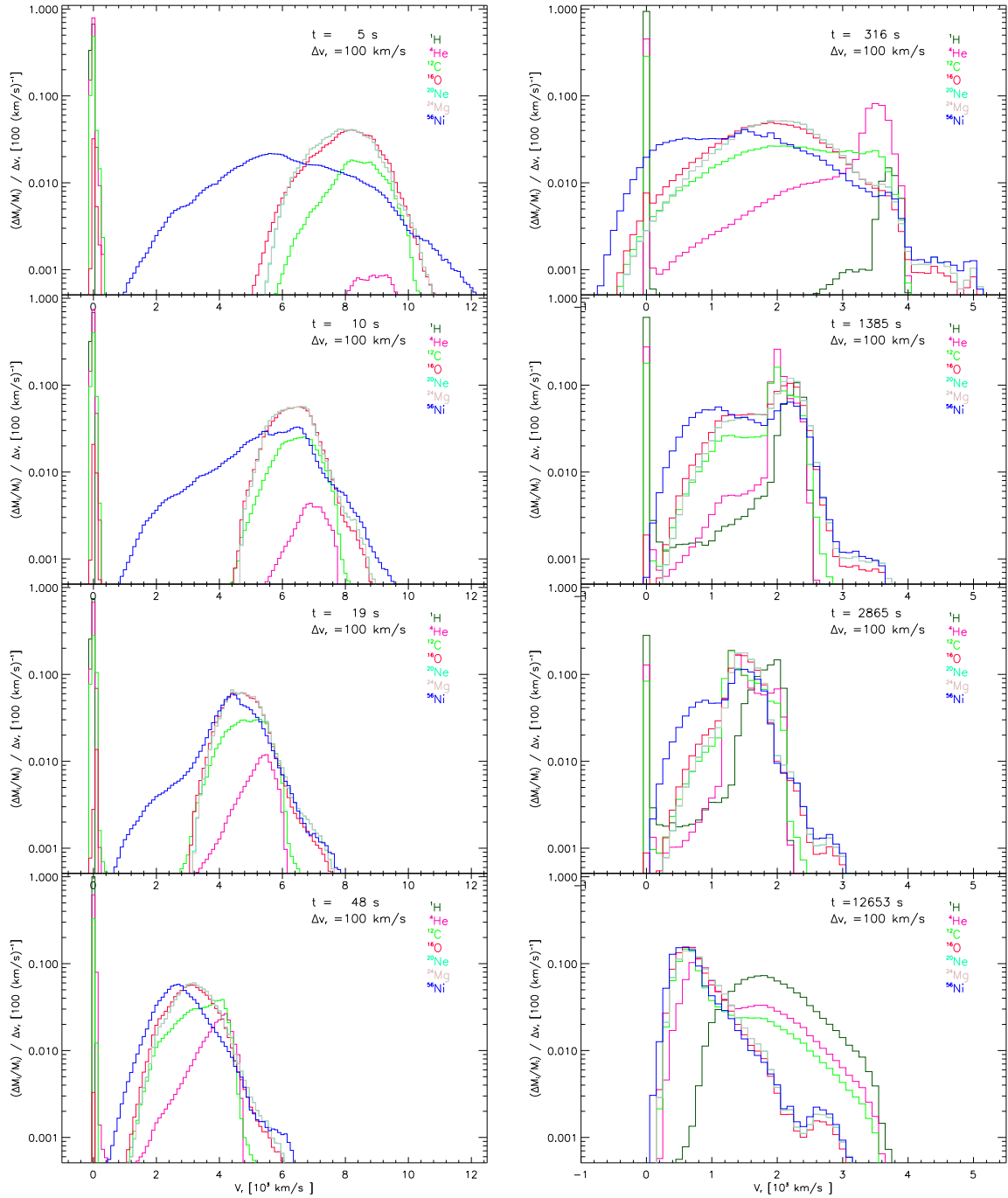


Figure 6.5: Normalised masses of the nuclear species of model 3D3 rebinned in the radial velocity space (Subsection 6.4.1) versus radial velocity at different epochs (see upper right corner of each panel). Note the cutoff of the hydrogen velocity distribution in the lower right panel. Hydrogen moving faster than the cutoff, has already left the computational domain.

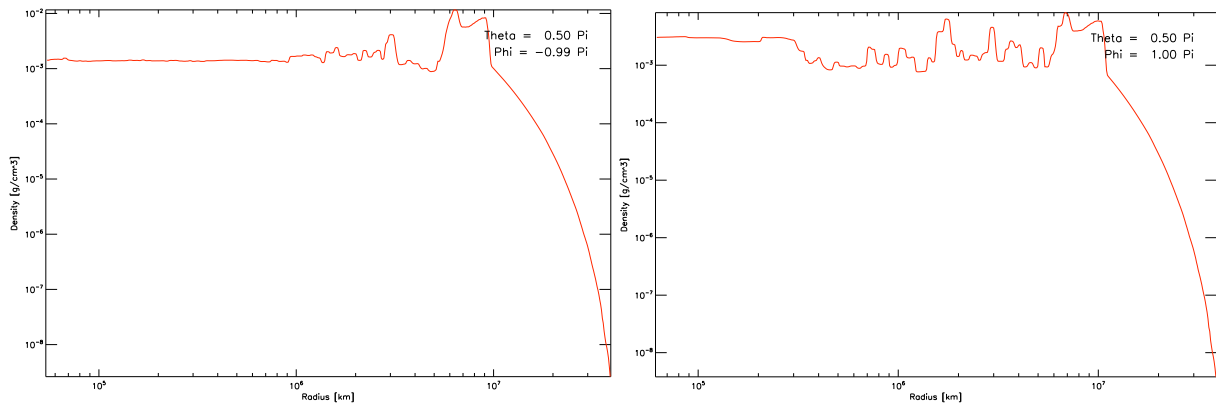


Figure 6.6: Representative radial density profile of the three dimensional model 3D3's slice 80 (left panel, Subsection 4.4.6) and of the two dimensional model 2D80 (right panel). Note that the "helium wall" is located between the shock wave at 10^7 km and the reverse shock at 3×10^6 km has very a similar size in both, the 2D and the 3D model.

interfaces between the Si core, the Oxygen-Neon-Magnesium core, and the Carbon-Oxygen core, respectively.

The fast moving clumps are composed of 48% ^{56}Ni , 39% ^{16}O , 12% ^{20}Ne and 1% ^{24}Mg (Figure 6.4). Comparing this to the original composition of the stellar core (Table 6.1, Figure 4.3), reveals that a large fraction of ^{56}Ni is mixed into the O/Ne/Mg core. Afterwards RTIs forming at the composition interfaces lying further outside are mixing the matter from the O/Ne/Mg core outwards, forming the fast moving clumps. Note that the relative abundances of ^{16}O , ^{20}Ne and ^{24}Mg are approximately the same as in the original stellar O/Ne/Mg core.

6.4.2 Clump velocity in 3D vs. 2D

Comparing the mass fractions in the radial velocity space of the two dimensional models 2D2 and 2D80 to the corresponding slices (Subsection 4.4.6) of the three dimensional model 3D3 shows that the velocities of clumps consisting of heavy elements, i.e. ^{16}O , ^{20}Ne , ^{24}Mg and ^{56}Ni , are comparable in the 2D and the 3D models up to 3 000 s. Until then the clumps have not reach the so-called "helium wall", which is located in front of the H/He interface. When passing the "helium wall", the clumps are effectively decelerated in the two dimensional simulations, whereas in the three dimensional simulations, the clumps are decelerated only moderately (Figure 6.8, 6.9, A.11, A.12, A.17 and A.22).

The supernova shock wave is accelerated when it reaches the step density gradient at the H/He interface ($n > 3$) and decelerated where the density gradient gets flatter again (cf. Subsection 6.2.2 and Figure A.2). A blast wave in spherical geometry (Sedov 1946, 1959) which is decelerated launches a reverse shock wave. The supernova shock wave is therefore splitted into two shock waves when it passes through the H/He interface. A transmitted shock wave which has practically the same strength as the original shock wave and continues its way outwards through the stellar envelope. And a much weaker reverse shock, where fast matter is significantly decelerated. The piled up matter, mainly ^4He , forms a high density structure, the so-called "helium wall" (Figure 6.6)

The unequal deceleration of clumps can be understood by means of the hydrodynamic drag force. Using Newtons approach to the drag force acting on clumps moving in a flow having a high Reynolds number Re ($Re \gtrsim 10^3$) can be expressed due to the kinetic energy which has to be consumed to change

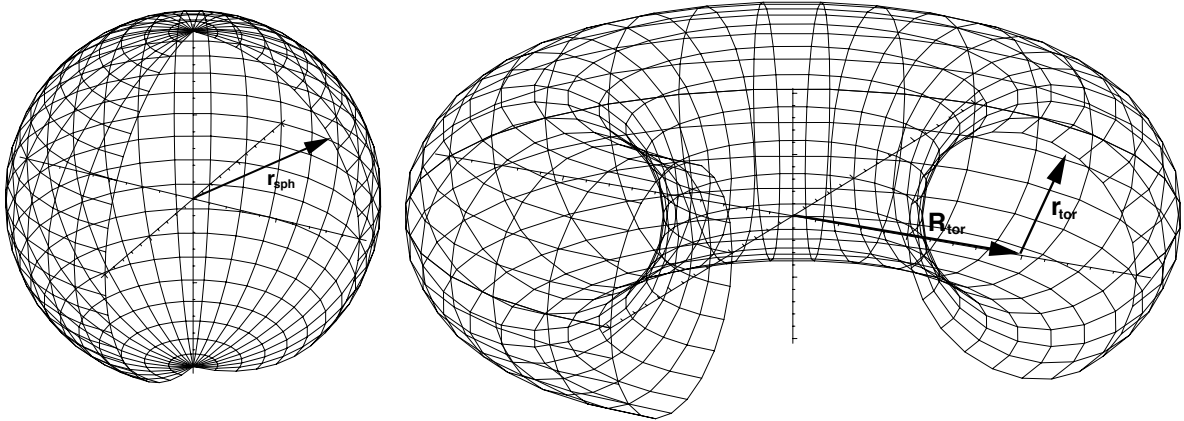


Figure 6.7: Schematic view of a sphere with radius r_{sph} (left) and a torus of thickness $2r_{\text{tor}}$ and diameter $2R_{\text{tor}}$ (right).

the clumps' velocity (e.g. Gerthsen 1997)

$$F_{\text{drag}} = \frac{1}{2} c_{\text{drag}} \rho A \vec{v}^2 \quad (6.3)$$

(in contrast to the approach of Stokes for bodies moving in a flow having a low Reynolds number Re ($Re \lesssim 10^3$). Here ρ is the density of the surrounding medium, A the geometric cross sectional area of the clump, the velocity of the clump is given by \vec{v} , and c_{drag} denotes the so-called drag coefficient. The drag coefficient depends on the form and surface characteristics of the clump, the Mach number Ma , the Reynolds number Re , and on the degree of turbulence of the hydrodynamic flow.

The Reynolds number Re measures whether a flow is turbulent or not. It is defined as

$$Re = \frac{\rho v l}{\eta} \quad , \quad (6.4)$$

where v the absolute value of the velocity $v = (v_r^2 + v_\theta^2 + v_\phi^2)^{\frac{1}{2}}$, l is the "size" of the clump ($l \approx 2r$), and η denotes the viscosity.

As long as the fast metal clumps propagate through the extremely thinned medium in the wake of the supernova shock wave their velocities in both two dimensional models 2D2 and 2D80 are the same within a few percent (Figure 6.8, 6.9) as in the three dimensional model 3D3 (in the slices which correspond to the 2D models (Subsection 4.4.6)). This changes significantly when the clumps reach the "helium wall" since

$$F_{\text{drag}} \propto \rho \quad , \quad (6.5)$$

and since the density of the "helium wall" is more than an order of magnitude higher than that of the post-shock matter (Figure 6.6). The dimensions and the shape of the "helium wall" are very similar in both the 2D models and the 3D model (Figure 6.6).

The physical conditions of the flow, both, of the clumps and of the surrounding medium are pretty much the same in the 2D and the 3D models. This leaves behind only one parameter which may account for the significantly larger deceleration of the metal clumps in the two dimensional models compared to the three dimensional models, and that is

$$F_{\text{drag}} \propto A \quad (6.6)$$

Let us for simplicity reasons assume that our “test” clump has a circular shape of the radius r . Then the topology of the “test” clump will be a sphere with the radius r_{sph} in the three dimensional case and, due to the assumed rotation symmetry, it will be a torus of thickness $2r_{\text{tor}}$ and diameter $2R_{\text{tor}}$ in the two dimensional case. The center of the torus, the center of the star and the origin of the spherical polar coordinate system, are assumed to coincide.

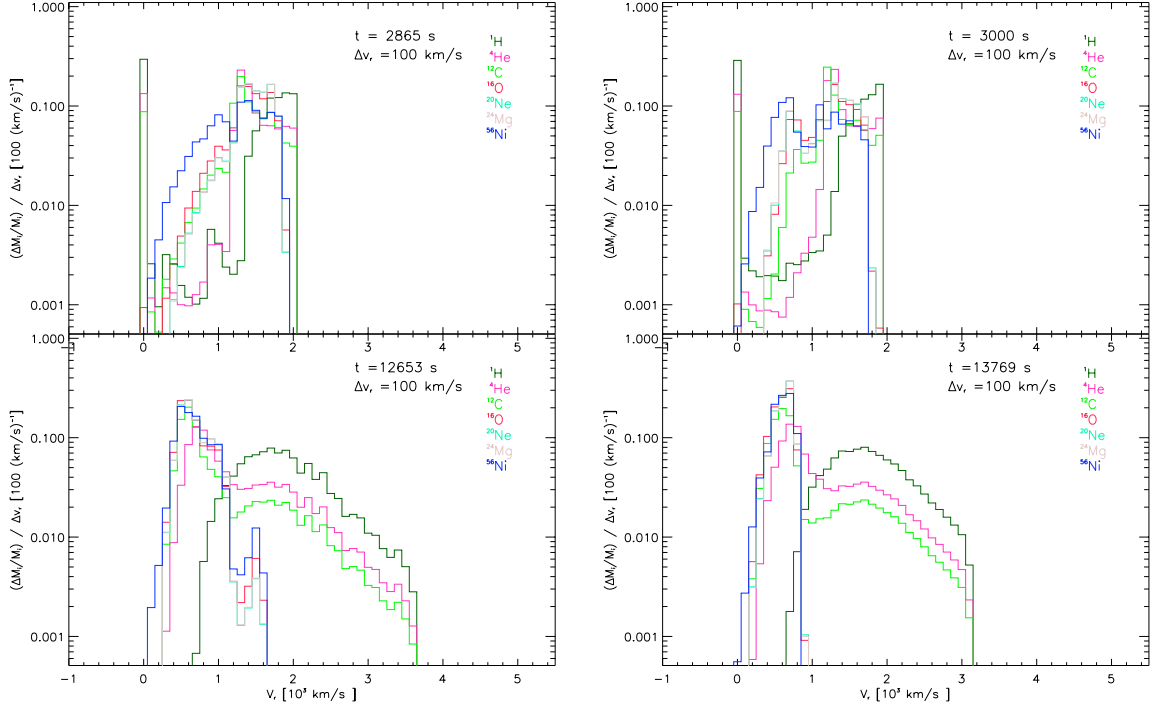


Figure 6.8: Various mass fractions of model 3D3 (slice 2 (Subsection 4.4.6), left panel) and model 2D2 (right panel) shown in the radial velocity space.

The geometric cross sectional area of a sphere is

$$A_{\text{sph}} = \pi r_{\text{sph}}^2 \quad , \quad (6.7)$$

whereas the geometric cross sectional area for a torus is

$$A_{\text{tor}} = 2\pi R_{\text{tor}} r_{\text{tor}} \quad . \quad (6.8)$$

We can estimate the growth of the clumps with time using a simple analytic model. We assume that the pressure of the progenitor envelope can be expressed using a power law function

$$p_{\text{env}}(r) \propto r^{-\beta} \quad (6.9)$$

and we approximate the relation between pressure p and density ρ with a polytropic equation of state

$$p = \kappa \rho^\Gamma \quad (6.10)$$

with the polytropic constant κ and the polytropic exponent Γ . The density of the clumps is proportional to their volume

$$\rho \propto V^{-1} \quad , \quad (6.11)$$

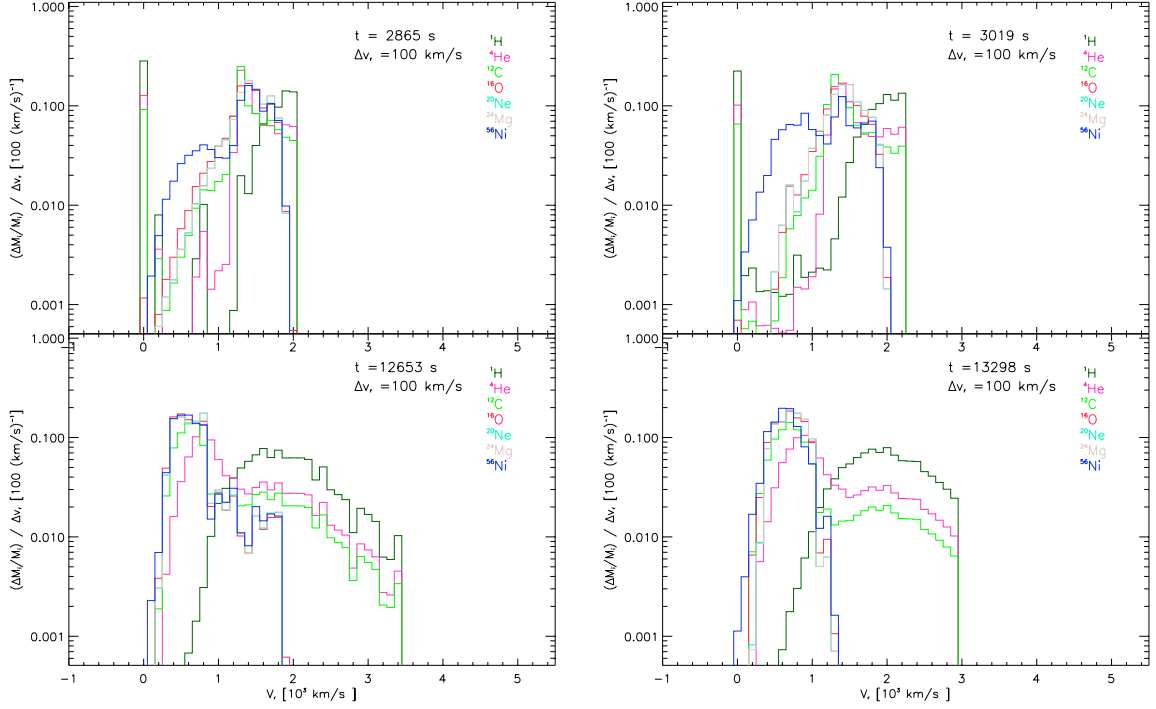


Figure 6.9: Same as Figure 6.8, but for model 3D3 (slice 80 (Subsection 4.4.6)) and model 2D80.

assuming conservation of mass. The volume of a torus is $V_{tor} = 2\pi^2 R_{tor} r_{tor}^2$ and that of a sphere is $V_{sph} = \frac{4\pi}{3} r_{sph}^3$. The diameter of a torus in spherical polar coordinates under the assumption of rotation symmetry is given by $R_{tor} = r \sin \theta$.

The last assumption we have to make is pressure equilibrium between the clumps and their environment

$$p_{env} \equiv p_{clump} \quad . \quad (6.12)$$

Using this assumption together with Equation 6.9, 6.10, and 6.11, one can express the geometrical cross section as a function of the radial distance $r(t)$ from the centre of the star. We get for the torus

$$A_{tor}(r) \propto (\sin \theta)^{1-\Gamma} r^{\frac{\beta+\Gamma}{2\Gamma}} \quad (6.13)$$

and for sphere

$$A_{sph}(r) \propto r^{\frac{2\beta}{3\Gamma}} \quad , \quad (6.14)$$

respectively. The pressure in the stellar envelope of a supernova progenitor is dominated by radiation pressure. Therefore we can approximate it by the polytrope with a polytropic exponent of $\Gamma \approx \frac{4}{3}$. Using this value of Γ , Equation 6.12 and 6.16, the geometrical cross section of a torus behaves like

$$A_{tor}(r) \propto (\sin \theta)^{-\frac{1}{3}} r^{\frac{3\beta}{8} + \frac{1}{2}} \quad (6.15)$$

and that of a sphere like

$$A_{sph}(r) \propto r^{\frac{\beta}{2}} \quad . \quad (6.16)$$

This means that, for $\beta < 4$, the torus has respectively a larger geometric cross sectional area than the sphere, especially at larger distances, where the H/He interface and the ”helium wall” are located ($\geq 1 \times 10^6$ km, Figure 4.3 and 6.6). And therefore, deceleration is more severe in case of axis symmetric simulations (Figure 6.8, 6.9).

When the clumps reach the ”helium wall” they first have to propagate through the reverse shock which has a very steep negative pressure gradient. Afterwards they move through the region between the supernova shock wave and the reverse shock, the actual ”helium wall” having a negative pressure gradient, too (Figure A.21). In that whole region the index β is negative (negative slope of the pressure profile) and hence the hydrodynamic drag is more severe than in other regions.

The above considerations provide a qualitative explanation why the clumps dynamics and velocity evolve similar in both, the 2D simulations and the 3D simulation, until the clumps reach the ”helium wall”. And why the deceleration of the clumps is much more severe in the 2D case.

Note that when rebinning of the mass fraction in radial velocity space of model 2D2 we omitted 5° — additionally to the already missing 15° cone — at the southern boundary in θ -direction, i.e. lower boundary in Figure A.18 and A.19. This was done because of an ”axis feature” which was developing there. These ”axis features” are well known from other studies (e.g. Kifonidis et al. 2003, 2006), although the feature which develops at the boundary of our model 2D2 is much smaller than in the latter cases, because the boundary in our two dimensional simulations is not located at $\theta = \pi$.

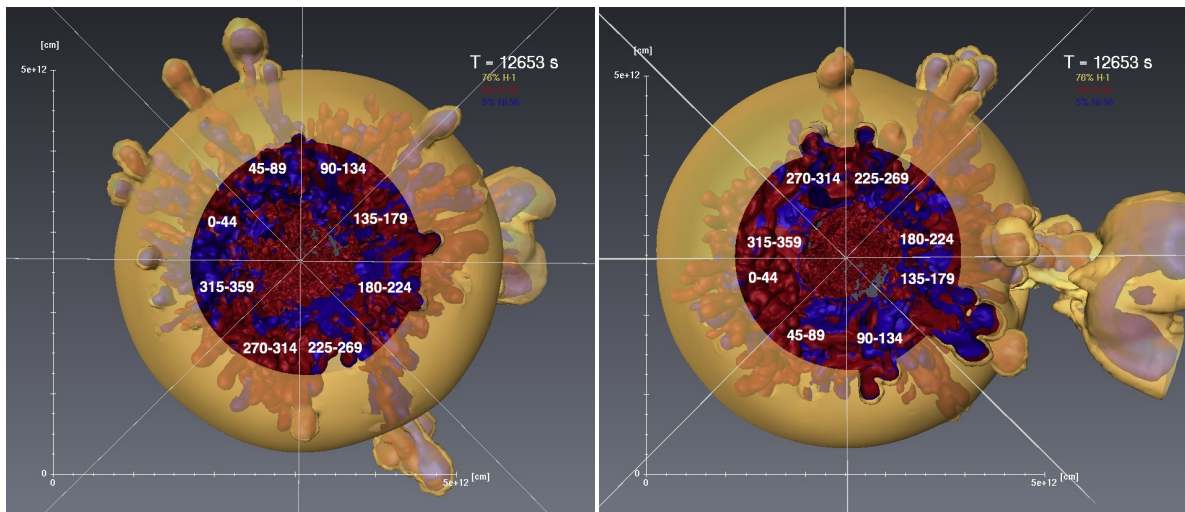


Figure 6.10: Angular data bins (Subsection 6.4.3) in longitudinal direction which are used in Figure 6.11. The white lines show the boundary of the data bins and the white numbers indicate the number of longitudinal data points included in the data bin. The plots show the clumps of ^{56}Ni (blue) and ^{16}O (red) penetrating through the H/He interface (beige) of model 3D3 at around 12.5 ks seen from the north pole (left) and the south pole (right). The length scale is 50 million km.

6.4.3 Spatial Distribution of Heavy Elements

The development of the RTIs at the Si/O composition interface, i.e. the Ni/O interface in our simulations, is deforming the interface until the boundary separating these two elements eventually is located in vertical direction. This boundary gets further twisted and distorted by the KHI and vanishes potentially. This can be seen in some of the RTI “fingers” in our models, especially the super “finger” (Figure 6.12, Figure A.16). Other “fingers” are consisting mainly of ^{16}O or ^{56}Ni , respectively.

To estimate the number of fast moving metal clumps and the maximum velocity of individually clump fractions, we performed a same analysis as described in Subsection 6.4.1. However, now we splitted the data sets of model 3D3 into 8 data-bins, equidistantly distributed along the longitudinal coordinate direction ϕ (Figure 6.11 and Figure 6.10). Both, the number of clumps and especially the maximum velocity of individually clump fractions, are impossible to derive from the rather continuously distributed mass fraction in the radial velocity space (Subsection 6.4.1, Figure 6.5) of the complete data domain. Note that the bins are denoted by the longitudinal indices included in the bin’s data domain (Figure 6.10).

Our analyses revealed that, depending on the initial conditions, it is possible to model the development and propagation of single super “clumps” (Figure 6.4) containing a few times $10^{-3} M_{\odot}$ of ^{16}O and ^{56}Ni and moving with velocities up to 3100 km s^{-1} . Comparing Figure 6.11 with Figure 6.5 shows that the high-velocity end of the composition mass fraction distribution is entirely dominated by the super “clump”. However, excluding the prominent “super clump” demonstrates that our model 3D3 is still able to “produce” a multitude of fast moving metal clumps (≥ 12 , Figure 6.10) moving with velocities up to 2350 km s^{-1} (Figure 6.11, right column: panel 2)

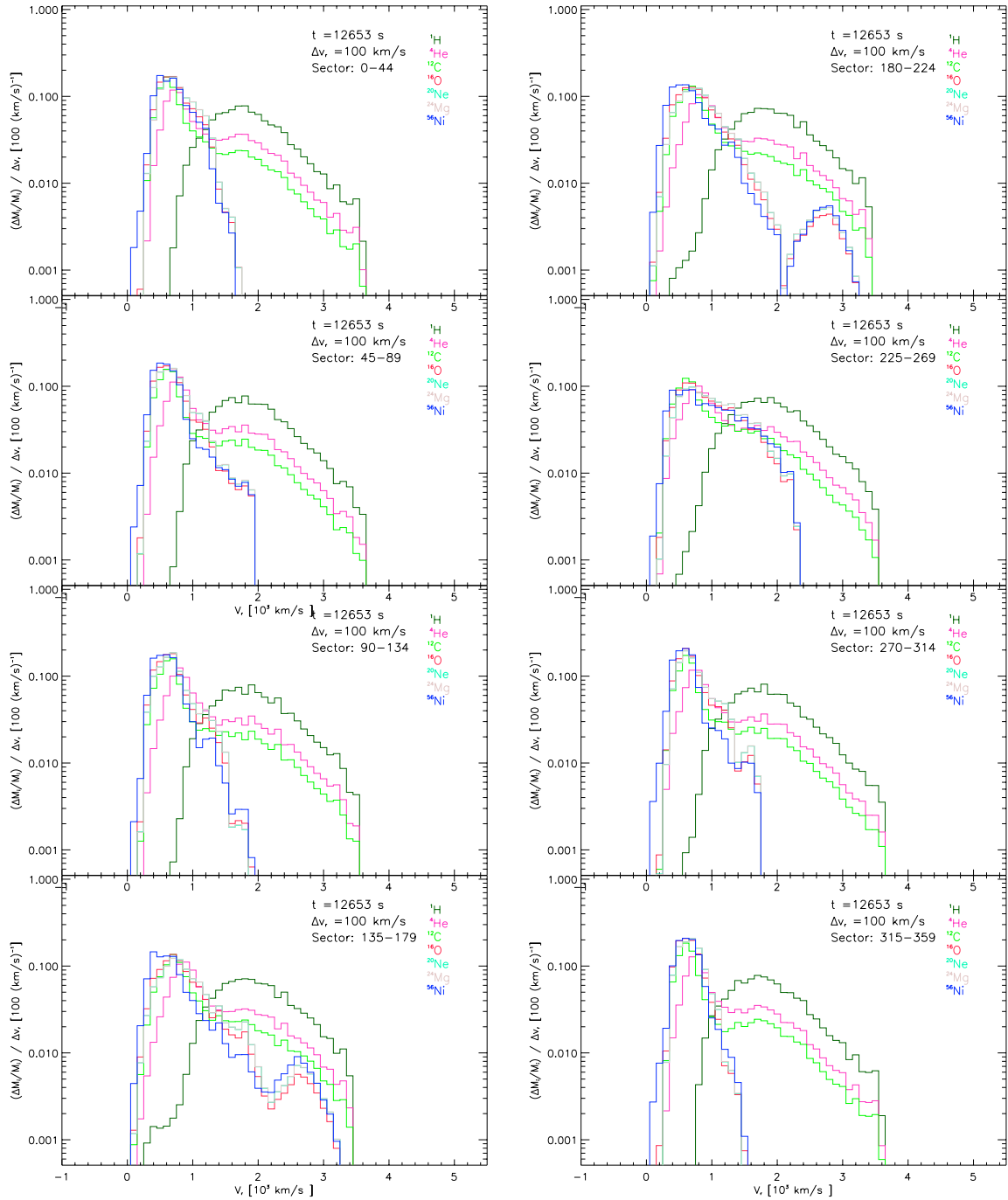


Figure 6.11: Same as Figure 6.5, but the longitudinal direction divided into 8 equidistant data bins (Subsection 6.4.3, Figure 6.10).

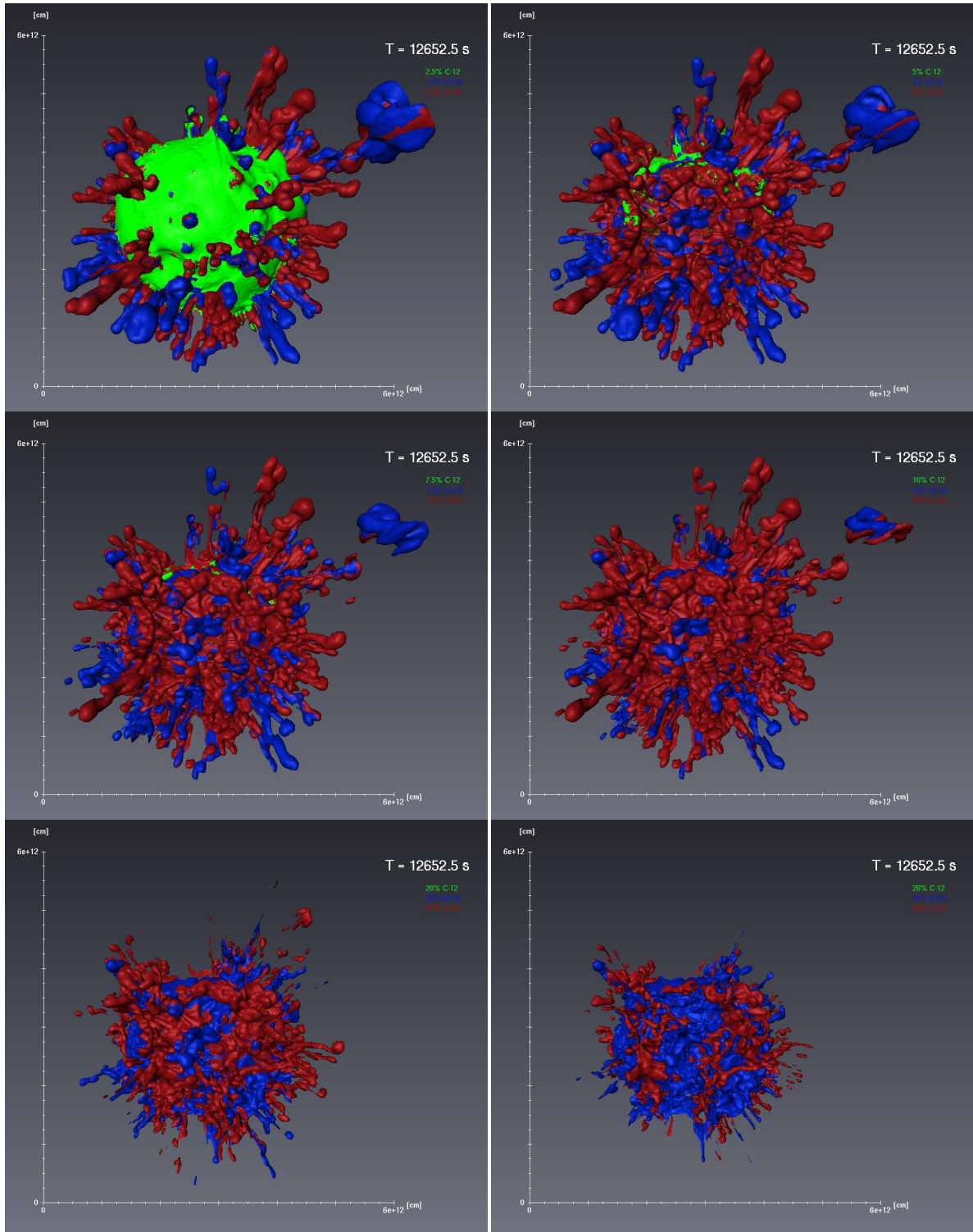


Figure 6.12: Panel of plots showing the iso-contours of different levels (2.5%, 5%, 7.5%, 10%, 20% and 30% from top left to bottom right) of the chemical species ^{12}C (green), ^{16}O (red) and ^{56}Ni (blue). The plot visualises the distribution of the heavy elements in model 3D3 at a late epoch around 12.5 ks.

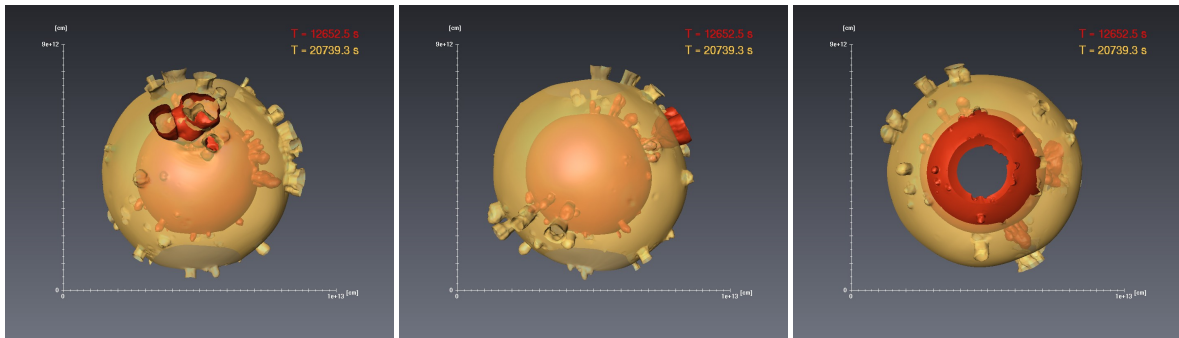


Figure 6.13: The three plots show the position and the shape of the H/He interface from various perspectives at two different epochs (red: 12.5 ks, beige: 21 ks). The viewing directions of the three plots (from left to right) correspond to the Cartesian coordinate directions x , y , z , respectively. Note that, the second epoch is shortly before the H/He interface leaves the computational grid. Note further that the interface was chosen as the iso-contour having an hydrogen abundance of 76%. Note that the length scale is about 100 million km.

6.5 The Richtmyer-Meshkov Instability in 3 Dimensions

6.5.1 RMI at the H/He Interface

In contrast to the 2D models of Kifonidis et al. (2006) (Figure 2.6) and our 2D model 2D80 (Figure 6.14), our three dimensional models 3D3 (Figure 6.13) and 3D2 do not develop a RMI at the H/He composition interface. Note that, in case of 3D2 due to the weaker shock deformation of the initial model (Subsection 4.4.5), one would not expect the development of a RMI.

Figure 6.13 shows the position and the shape of the H/He interface of model 3D3 at two epochs (at 13 ks shown in red and 21 ks shown in beige) in the late phase of our simulation, shortly before the interface is advected through the outer boundary of the computational domain. One can see the distorted shock wave was able to deform the interface. However, it failed to launch an observable RMI, and therefore to disrupt the intire interface. Instead of that the interface is partially disrupted by fast metal clumps acting as canon balls, which penetrate the interface (Section 6.4).

Remember that vorticity is a conserved quantity in two dimensionsal simulations, due to the assumed rotation symmetry. However, this is not the case in three dimensional simulations. Therefore, it might be the case that the vorticity which is deposited at the H/He interface by the aspherical supernova shock wave is redistributed in 3D, e.g. by turbulence, before a noticeable vortex has been formed.

6.5.2 Time Scale of the Development

Unfortunately, there is no analytic approach for the growth rate of the RMI in spherical coordinates. This is because Taylor's formalism which was used by Richtmyer to derive analytic expression (Subsection 5.4.2) is already unstable by itself in the spherical case (Subsection 5.2.3).

But to get an estimate of the time scales of the RMI for our models, one can use the impulsive Richtmyer-formula for the planar case (Subsection 5.4.2). This is an acceptable approximation, as long as the size of the structures is significantly smaller than the radius of the spherical interface. The impulsive Richtmyer-formula is given by Equation 5.55

$$\dot{\eta}_{imp} = k \Delta u A \eta_0 \quad , \quad (6.17)$$

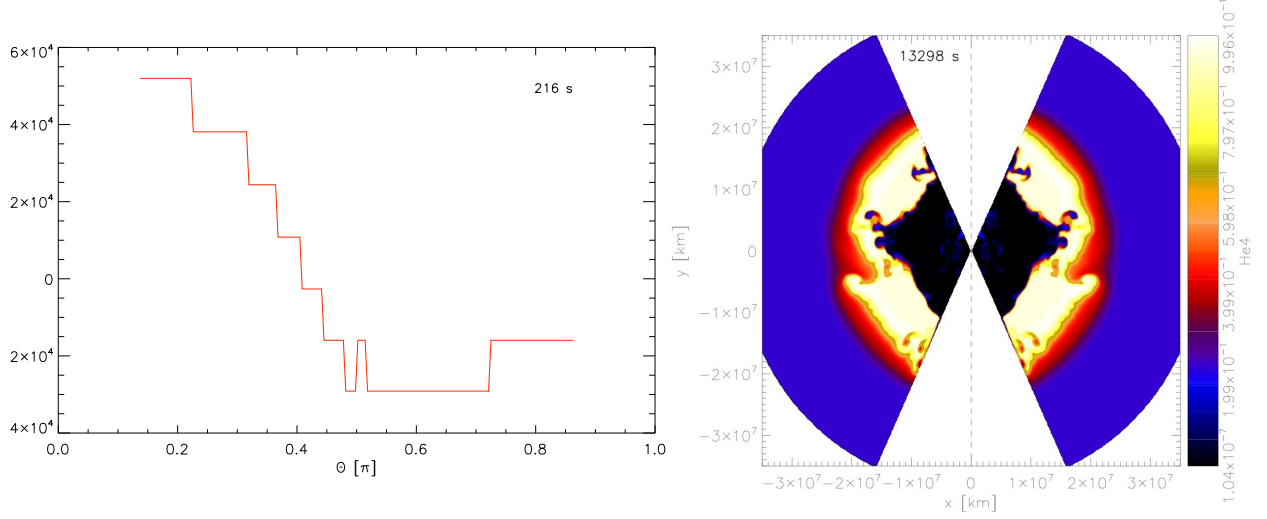


Figure 6.14: Left Panel: The deformation of the shock wave in model 2D80 216 s after core bounce, measured as difference of the shock positions $\Delta R_s(\theta)$ as a function of the azimuth angle θ . At that time the shock wave crosses the H/He interface. Note that the height of the steps trace the resolution of the grid and that the shock deformation in our simulations is barely resolved.

Right panel: Nuclear mass fraction of ${}^4\text{He}$ in model 2D80 showing the H/He interface at a late epoch. A large vortex which was generated by the RMI, located a bit south of the equator at about 2×10^7 km, has distorted the interface at about 13 ks after onset of the explosion.

where k denotes the shock perturbation wave number, Δu the velocity of the interface after shock transmission, A the Atwood number (Equation 5.52) of the interface, and η_0 the dimensionless shock perturbation amplitude.

The wave number and the dimensionless amplitude of the shock perturbation can be derived from the left panel of Figure 6.14. The perturbation of the shock wave in model 2D80 cannot be described as a single mode sinusoidal perturbation. However, using the global shape of the shock wave and the little feature near $\theta = \frac{\pi}{2}$, we can derive two “extreme” cases. One with $\lambda \approx 1.6\pi \times R_S$ and $A \approx 8 \times 10^4$ km and the other with $\lambda \approx 0.05\pi \times R_S$ and $A \approx 1.3 \times 10^4$ km. Using Equation 5.53 we get for the perturbation wave number

$$k = \frac{2\pi}{\lambda} \approx \frac{2}{0.05 \cdot 1.2 \times 10^6 \text{ km}} \approx 3.3 \times 10^{-5} \text{ km}^{-1} \quad (6.18)$$

and for the dimensionless shock perturbation

$$\eta_0 = \frac{\Delta R_s}{R_s} \approx \frac{\Delta R_s}{R_{H/He}} \approx \frac{13000 \text{ km}}{1.2 \times 10^6 \text{ km}} \approx 1.1 \times 10^{-2} \quad (6.19)$$

assuming $R_s \approx R_{H/He} \approx 1.2 \times 10^6$ km (Figure 4.3). Note that the values for the perturbation wavelength from Figure 6.14 is given in radian. Therefore, we have to multiply it with the Radius of the H/He interface $R_{H/He}$. For the interface velocity we get $\Delta u \approx 4500 \text{ km s}^{-1}$ (Figure A.1). The Atwood number A ranges between $A \approx 0.37 \dots 0.56$ depending on the assumed size of the interface (Figure A.20).

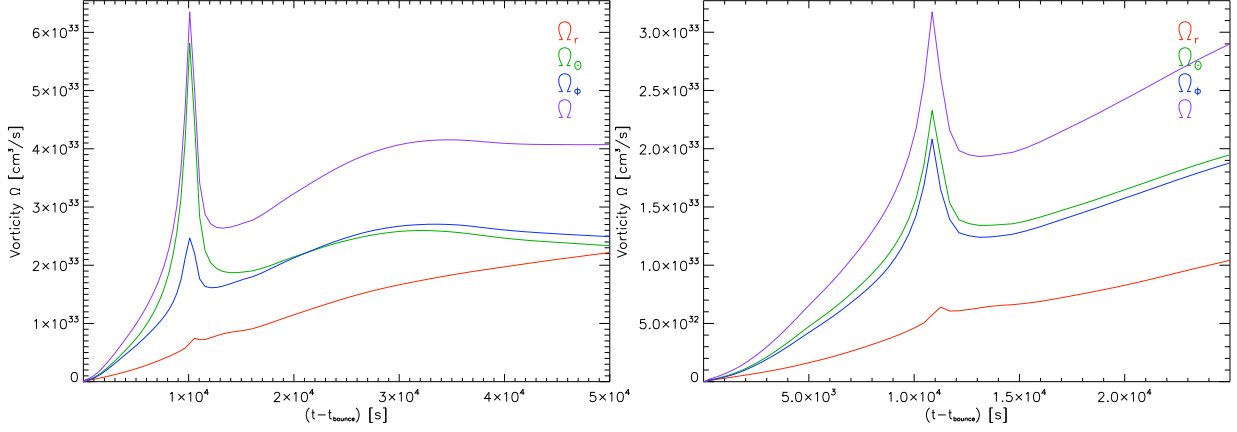


Figure 6.15: Left panel: Integrated absolute vorticity Ω (Equation 6.21) of model 3D3 (purple). Additionally, $|\Omega_r|$, $|\Omega_\theta|$ and $|\Omega_\phi|$ are plotted in red, green, and blue, respectively. Right panel: Same as left panel, but for model 3D2.

Combining all the estimates gives us an impulsive RMI growth time scale τ_{RMI} of

$$\begin{aligned} \dot{\eta}_{imp} &= k \Delta u A \eta_0 \approx 3.3 \times 10^{-5} \text{ km}^{-1} \cdot 4500 \text{ km s}^{-1} \cdot 0.56 \cdot 1.1 \times 10^{-2} & (6.20) \\ \tau_{\text{RMI}} &= \frac{1}{\dot{\eta}_{imp}} \approx 1100 \text{ s} \end{aligned}$$

for the more optimistic case and

$$\tau_{\text{RMI}} \approx 8900 \text{ s}$$

for the more pessimistic case. The actual RMI growth time scale should lie in between these two numbers, which is indeed the case. After 3 000 s, model 2D80 shows a clearly detectable RMI vortex (Figure 6.14, left panel).

6.5.3 Analysis Using Volume-Integrated Vorticity

To find a trace of a potentially developing RMI at the H/He interface of our three dimensional models 3D3 and 3D2, we performed an analysis of our data, similarly as described by Kifonidis et al. (2006). These authors calculated the volume-integrated vorticity of their two dimensional flow data. The integrated vorticity is defined as

$$\Omega(t) = \int_V \left| \vec{\nabla} \times \vec{u}(r, \theta, \phi, t) \right| dV \quad . \quad (6.21)$$

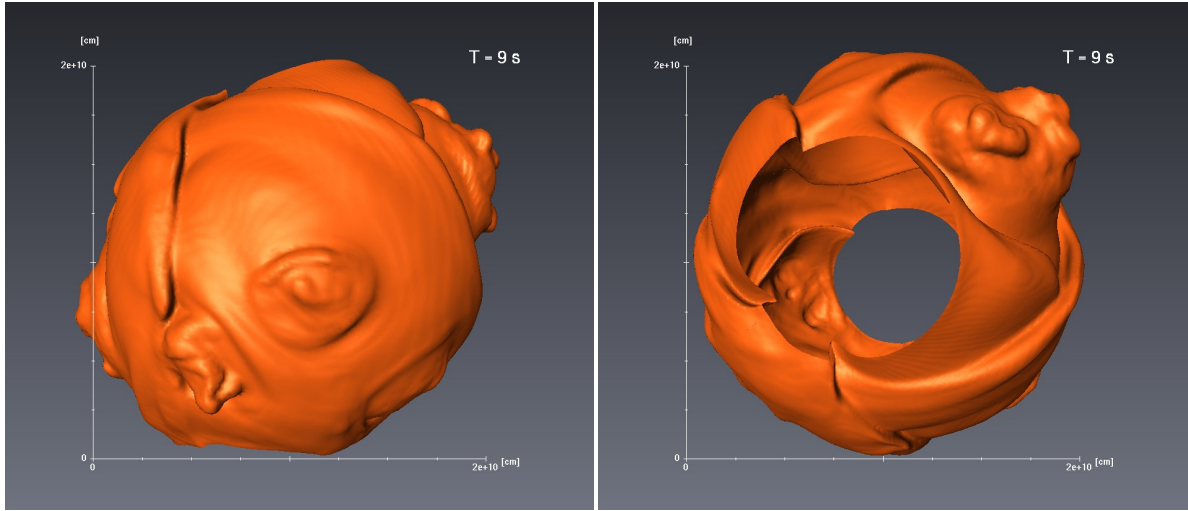


Figure 6.16: Two snapshots of model 3D3 9 s after core bounce showing developing RMIs at the (C+O)/He interface. The interface is “crumpled” by several extended RMI vortices. The length scale about 20 000 km.

Note that, Kifonidis et al. (2006) did not take the absolute value in their calculation. Together with Equation C.9 we get the following expression in spherical polar coordinates

$$\Omega(t) = \int_{R_i}^{R_o} \int_0^\pi \int_0^{2\pi} \left(\frac{1}{r^2 \sin^2 \theta} \left[\frac{\partial}{\partial \theta} (\sin \theta u_\phi) - \frac{\partial u_\theta}{\partial \phi} \right]^2 \right) r^2 \sin \theta dr d\theta d\phi \quad (6.22)$$

$$+ \frac{1}{r^2} \left[\frac{\partial u_r}{\partial \phi} - \frac{\partial}{\partial r} (r u_\phi) \right]^2 r^2 \sin \theta dr d\theta d\phi \quad (6.23)$$

$$+ \frac{1}{r^2} \left[\frac{\partial}{\partial r} (r u_\theta) - \frac{\partial u_r}{\partial \theta} \right]^2 r^2 \sin \theta dr d\theta d\phi \quad (6.24)$$

Figure 6.15 shows that the volume-integrated vorticity continuously grows in our models until it saturates around 3×10^4 s. The saturation is due to the fact, that the material carrying the vorticity is leaving the computational grid. The second feature is the large vorticity “spike” at around 1×10^4 s, coincident with the large fast metal-clump (Section 6.3) leaving the grid.

These two observations imply that the largest contribution to the volume-integrated vorticity is due to Kelvin-Helmholtz vortices which are located on the tips of the Rayleigh-Taylor fingers. With ongoing expansion of the supernova envelope these fingers are growing and the vortices occupy a larger volume, and therefore, they contribute more vorticity. The large clump and the vortices associated with it moves with a higher velocity than the average of the RT fingers (Figure 6.5, 6.11) and it carries larger KH vortices, hence the volume-integrated vorticity is rising steeply when the clump is reaching the outer parts of the grid and is dropping again after the clump has left the grid.

This interpretation is strongly supported by the analogous analysis of model 3D2. This model does not develop fast metal clumps (Section 6.3), and especially large clumps are only marginally recognisable. Likewise the “spike” is visible, but reaches only half the height compared to the “spike” of model 3D3. Furthermore, the RT fingers move on average with smaller velocities than in model 3D3, for which reason, i.e. model 3D2 shows no saturation of the volume-integrated vorticity (Figure 6.15, right panel).

6.5.4 RMI at the (C+O)/He Interface

Although, we found no traces of a developing RMI at the H/He interface, the developing RMIs triggered by the aspherically deformed supernova shock wave at the (C+O)/He composition interface (Figure 2.1) was easy to detect (Figure 6.16). However, in contrast to the work of Kifonidis et al. (2006), where the RMI plays an important role in the mixing process by disrupting the H/He interface, the RMI found here only produces an additional “mixing finger” similar to the “Rayleigh-Taylor-mushrooms”. This can be best seen from the time series of entropy contours plotted for slice 80 of model 3D3 (Figure A.7).

This detection supportingly suggests that the deformed shock wave triggers RMIs at the other composition interface located inside the (C+O)/He interface, too, especially because the deformation of the shock is larger by trend shortly after the onset of the explosion. However, as the dynamic time scales get shorter for the composition shells lying deeper inside the star, it is impossible to detect a distinct RMI there. Instead developing RMIs contribute to the turbulent mixing of heavy elements inside the exploding star.

6.6 Discussion and Conclusions

6.6.1 Strength of Our Study

Our simulations are the first 3D simulations using a high resolution shock capturing scheme to follow the SN shock wave from a few milliseconds after the core bounce (up to 1s, see Scheck et al. 2006a) to hours later, long after the shock wave has left the star.

In contrast to previous works (Section 2.3) we do not use a parametrised energy deposition or parametrised asphericity of the shock wave. The explosion models we used as initial models (Scheck et al. 2006a, Section 4.4), simulated the neutrino driven supernova explosion using a parametrised neutrino transport scheme (Section 4.4) and a tabulated EOS. Our models cover the full 3D sphere, with only a small cone omitted along the polar coordinate singularity (Section 4.3).

6.6.2 Weakness of Our Study

The models 3D3 and 3D2 have explosion energies of 0.65 Bethe and 0.49 Bethe, respectively. That means they are sub-energetic SNe, compared to an “standard” SNe, which has a typical explosion energy of ~ 1.0 Bethe (Kasen & Woosley 2008). This raises the question how representative these models are for a typical core collapse SN or which kind of supernova sub-type do our models match?

Both models include the nuclear species produced during the progenitors thermonuclear evolution. However, a large amount of chemical species is synthesised during the supernova explosion by explosive nuclear burning, e.g. most of the radioactive ^{56}Ni released in a supernova explosion. Scheck et al. (2006a) neglected explosive nuclear burning to save computational costs. We made the same decision, on one hand to save computational costs — remember both models together needed roughly 435 000 CPU-h of HPC computer time — and on the other hand because no input data from the models of Scheck et al. (2006a) were available.

Our models do not include gravity. The derived expansion velocities, especially of the fast moving heavy element “clumps” are therefore overestimated.

Both initial models exhibit a $l = 1$ SASI mode (Subsection 2.1.3, 4.4.5), thus a detailed comparison with the models of Kifonidis et al. (2006) was not possible, as their models only exhibit $l = 2$ SASI modes. Furthermore, according to Scheck et al. (2006b) all SNe which develop a SASI exhibit

either a $l = 1$ or $l = 2$ mode, respectively, which means that our study explored only one half of this parameter space.

6.6.3 Discussion of Our Results

The RTIs which develop in our 3D models 3D3 and 3D2 are similar in size and shape to the RTI described in previous works (e.g. Kifonidis et al. 2003, 2006). Though shape of the RTIs in our simulations appears more roundly, which is due to the 4 times coarser resolution in our simulations compared to works previous. At late epochs the velocity of the RTI mushrooms is higher in the 3D simulations than in the 2D simulations of Kifonidis et al. (2003), as well as in our 2D comparison simulation. This can be understood using a geometric model (see below and Subsection 6.4.2).

Model 3D3 develops a “super clump”, i.e. a clump containing a few $10^{-3} M_{\odot}$ of ^{16}O , ^{20}Ne , ^{24}Mg and ^{56}Ni moving with a velocity of up to 3100 km s^{-1} . This clump has the right characteristics to explain some phenomena associated with SN 1987A (Subsection 1.3.2). However, future work has to investigate the probability of producing such a “super clump” depending on the initial conditions. Furthermore, the question remains how strong the evolution of such a “super clump” is influenced by the turn off of gravity at 1 s (Section 4.3, Section 4.4).

We find that our model 3D3 develops fast moving clumps of heavy elements moving with velocities up to 2350 km s^{-1} , in the case of our “super clumps” even up to 3100 km s^{-1} , although model 3D3, exhibiting an aspheric deformed shock wave (Section 6.5, Subsection 4.4.5), does not develop a RMI at the H/He composition interface. This result contradicts the conclusions of Kifonidis et al. (2003), who found that models which a spherical shock wave do develop fast clumps, however, they are heavily decelerated at the “helium wall” below the H/He composition interface. We found the same behaviour of the clumps in our 2D comparison models 2D2 and 2D80. We show that this behaviour is due to geometric effects caused by the assumed rotational symmetry in the 2D simulations.

Our models still fail to produce clump velocities as high as those observed by Mitchell et al. (2001, Subsection 1.3.2, Section 2.2) by several hundred km s^{-1} . However, since our model 3D3 does develop clumps with velocities up to 3100 km s^{-1} , it is an interesting question whether simulations using initial models with explosion energies exceeding that of our initial model (Subsection 4.4.4) would succeed to produce the right clump velocities. This is a task for future work.

Since our initial models do not develop a RMI at the H/He composition interface, it is still unclear whether the result of Kifonidis et al. (2006), that the developing RMI disrupts the H/He interface and the “helium wall” and therefore suppresses the deceleration of the clumps, is important for three dimensional models or not. This question can be answered by simulating explosions with initial models exhibiting a strong aspheric shock wave. It is likely that more than one mechanism is realised in nature to mix heavy nucleosynthesis products outwards into the hydrogen envelope with high velocities (Subsection 1.3.2, Section 2.2).

Nevertheless, our model 3D3 develops a clearly detectable RM instabilities at the (C+O)/He interface (Subsection 6.5.4). However, these RMIs do not play a role for mixing heavy chemical species outwards. They rather contribute to mixing as the RTIs or convection does. We were able to trace one RMI vortex from its formation at the (C+O)/He interface to later epochs (Figure A.7, Subsection 6.5.4), showing that it forms a mushroom shaped structure very similar to the well known RTI mushrooms. Moreover, the detection of RMIs at the (C+O)/He interface suggests that RMIs are triggered at the composition interfaces lying inside the (C+O)/He interface, too. However, due to the much shorter dynamic time scales in these stellar parts it is not possible to detect the RMI there, although it contributes to the turbulent mixing inside the exploding star.

6.6.4 Outlook on Future Works

Using supercomputers of the next generation it will be possible to perform three dimensional radiation hydrodynamic supernova simulations using the computer code described in Scheck et al. (2006b), and to reach a final time of 2 to 4 seconds, when the explosion energies of such models will have saturated.

With the computer code mentioned above it is also possible to include a detailed nuclear reaction network to follow the explosive nuclear burning during the supernova explosion and trace a much larger set of nuclear species, provided that enough computer power and main memory is accessible. Thus it will be possible to reveal detailed information about the production and mixing of heavy elements. In addition, it should be possible to link some of SN1987 A's observed features to the simulated models in a more detailed manner.

Of course it is preferable and possible to include gravity. However, this remains a challenge due to the reasons discussed in Section 4.1 which can only be mastered with more computer time. To get an estimate of the amount of CPU time needed for simulation including gravity, we performed a 2D simulation with gravity, which needed 5 times more timesteps than comparable 2D simulations without gravity. This translates for 3D simulations to a requirement of roughly 1 million CPU-hours.

A huge step forward which is definitely not achievable within the near future is to calculate three dimensional models using a Boltzmann neutrino transport scheme (e.g. Rampp & Janka 2002; Buras et al. 2006) as initial models for the shock propagation simulations.

Part IV
Appendix

Appendix A

Additional Plots

In this chapter of the appendix we show plots and plot panels are of minor importance for our analyses presented in Part III and for which there was no room in the main body of the thesis. To some of them is referred in the thesis' text, but not to all. However, to complete the picture of our work, we like to present a comparable set of plots for all models included in this study.

1.1 Additional Plots Initial Model

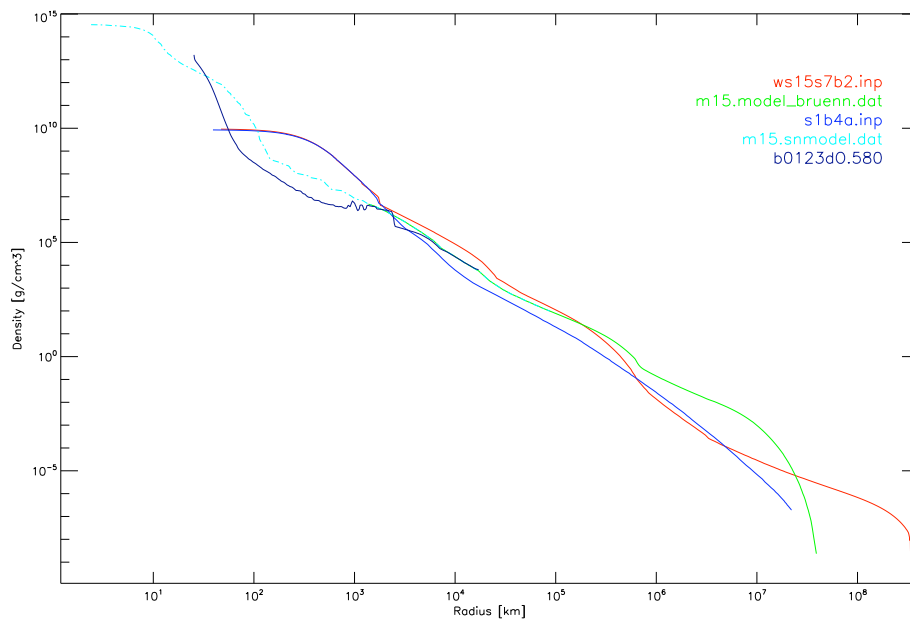


Figure A.1: Comparison of the density profiles of different SN progenitor models. The progenitor model used for our initial models is the green curve denoted with `m15.model_bruenn.dat`. The H/He interface is marked by a small density step near 10⁶ km.

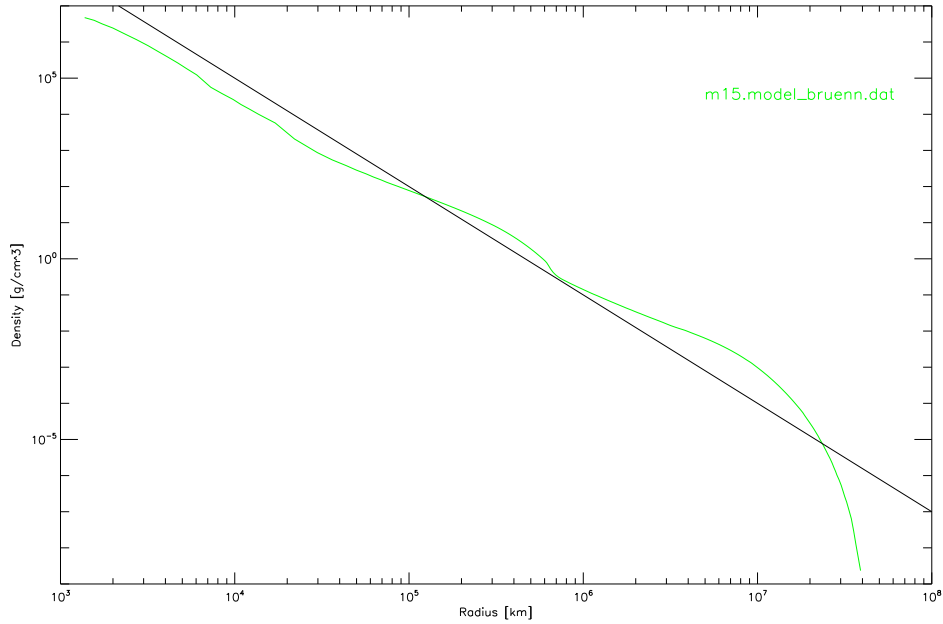


Figure A.2: Comparison of the density profiles of our SN progenitor model `m15.model_bruenn.dat` with a power law of the slope $\sim R^{-3}$ plotted in black.

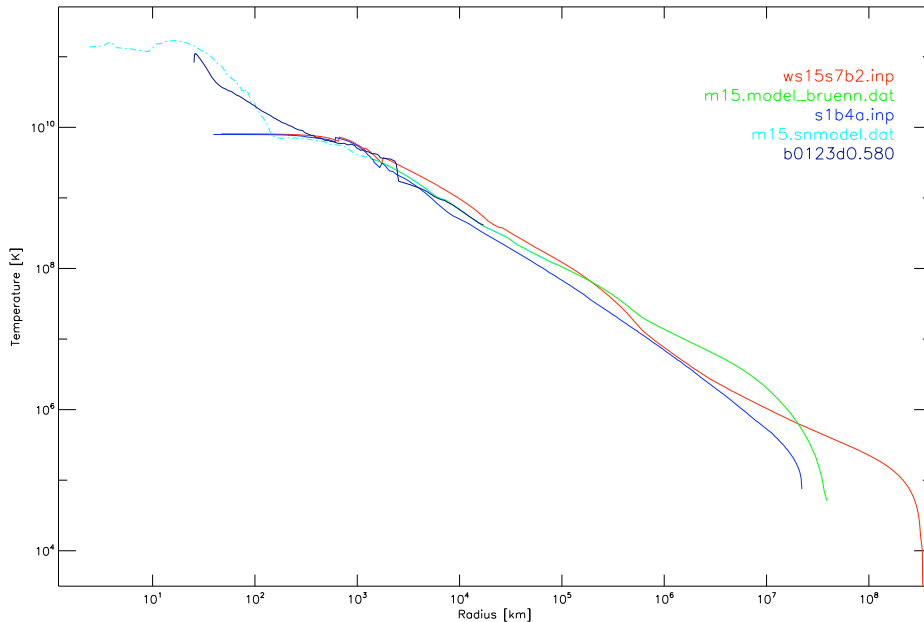


Figure A.3: Comparison of the temperature profiles of different SN progenitor models. The progenitor model used for our initial models is the green curve denoted with `m15.model_bruenn.dat`. The H/He interface is marked by a small density step near 10^5 km.

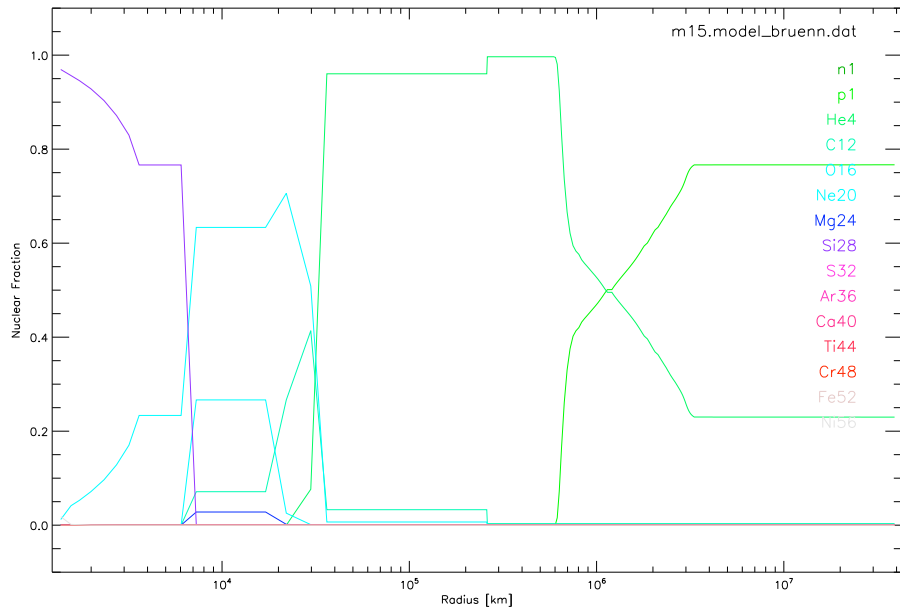


Figure A.4: Nuclear composition structure of the progenitor model m15.model_bruenn.dat which we used for our initial model.

1.2 Additional Plots Model 3D3

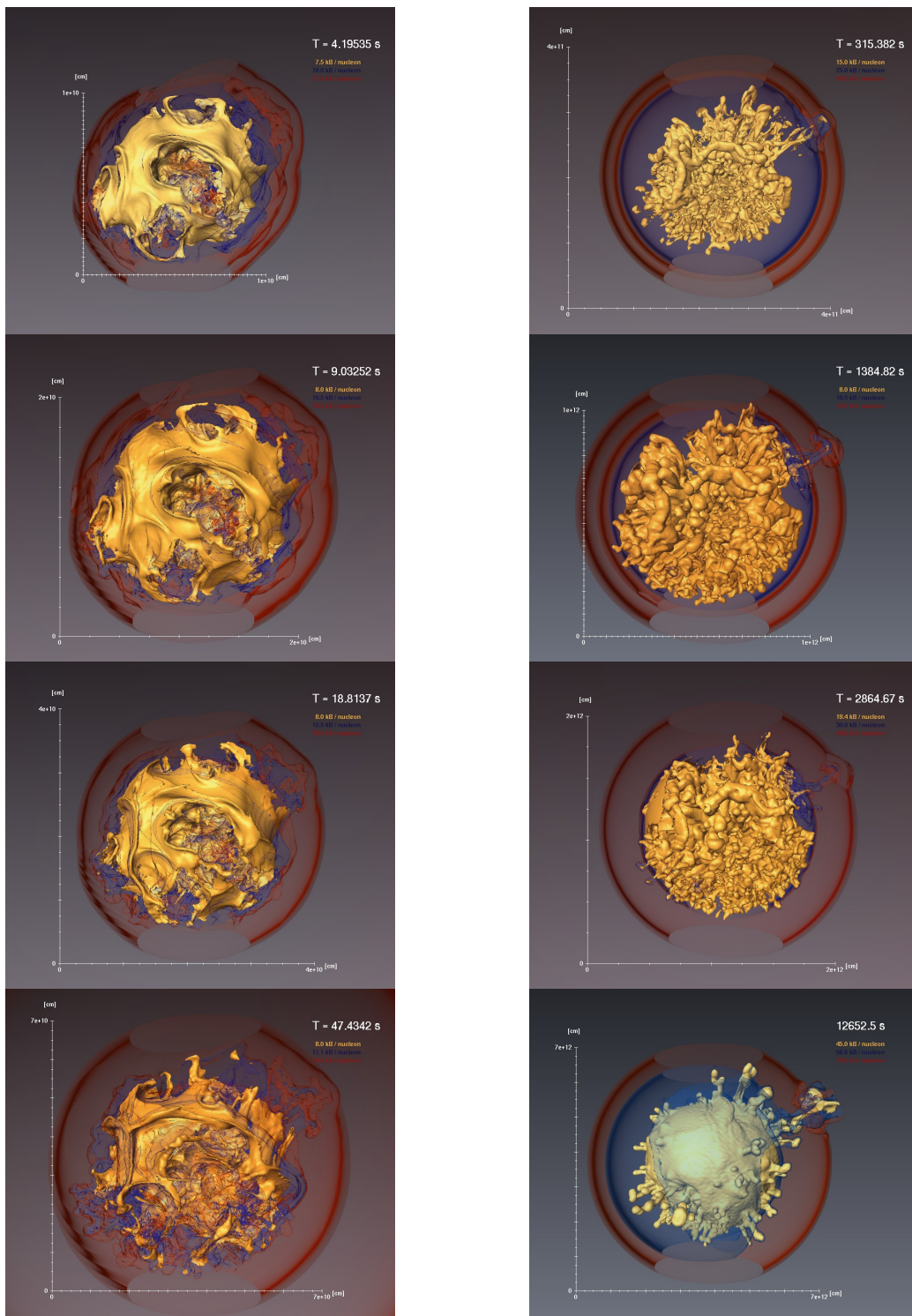


Figure A.5: Series of plots showing the entropy structure of model 3D3 evolving with time. Each plot shows a set of three entropy iso-contours, chosen to visualise a maximum of the substructure contained in the data.



Figure A.6: Series of plots showing the entropy structure of model 3D3's slice 2 evolving with time.

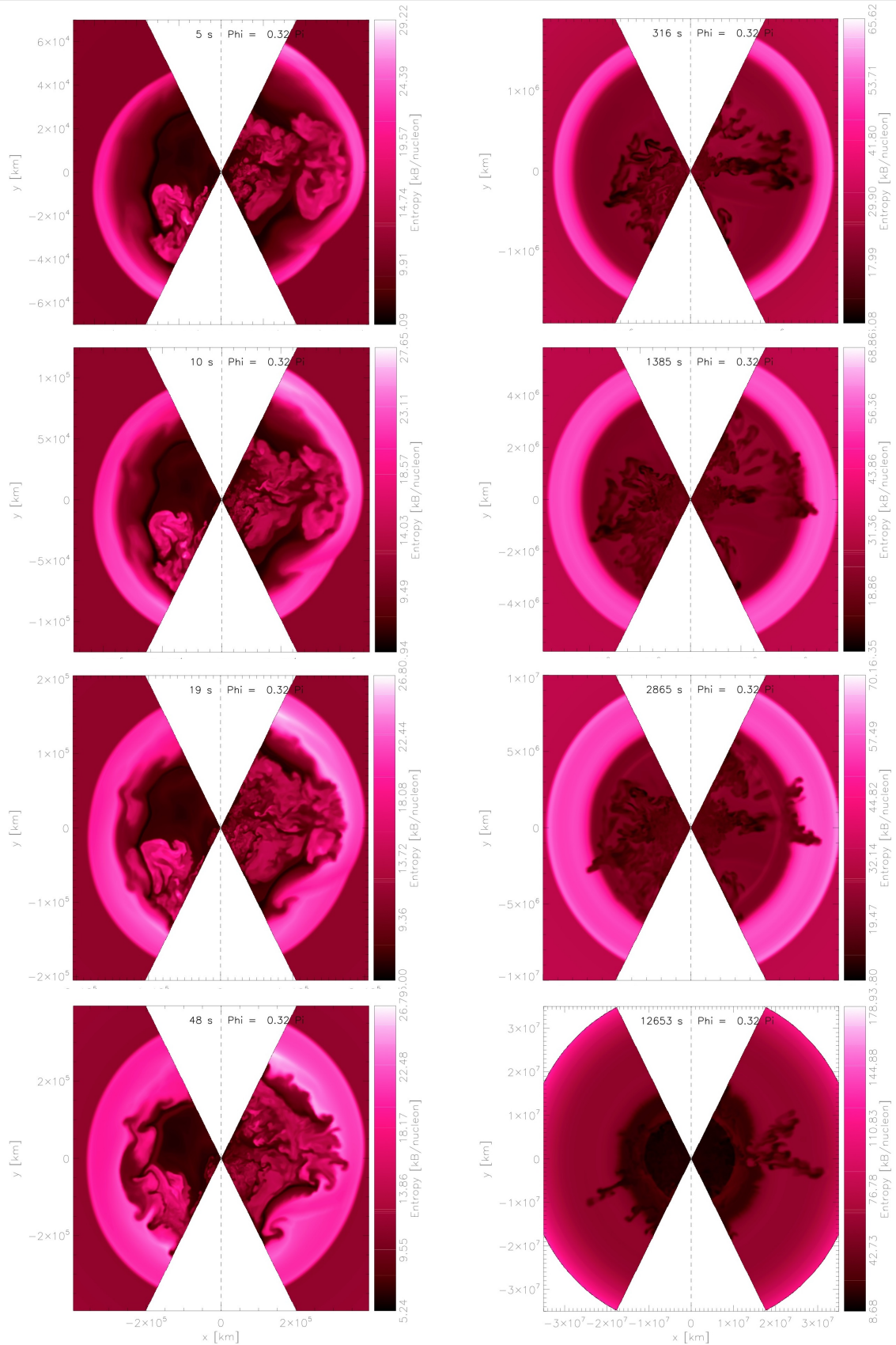


Figure A.7: Series of plots showing the entropy structure of model 3D3's slice 80 evolving with time. Note the RMI vortex which starts to develop at the (C+O)/He composition interface at a distance of 40 000 km in first panel on the left side near the southern boundary.

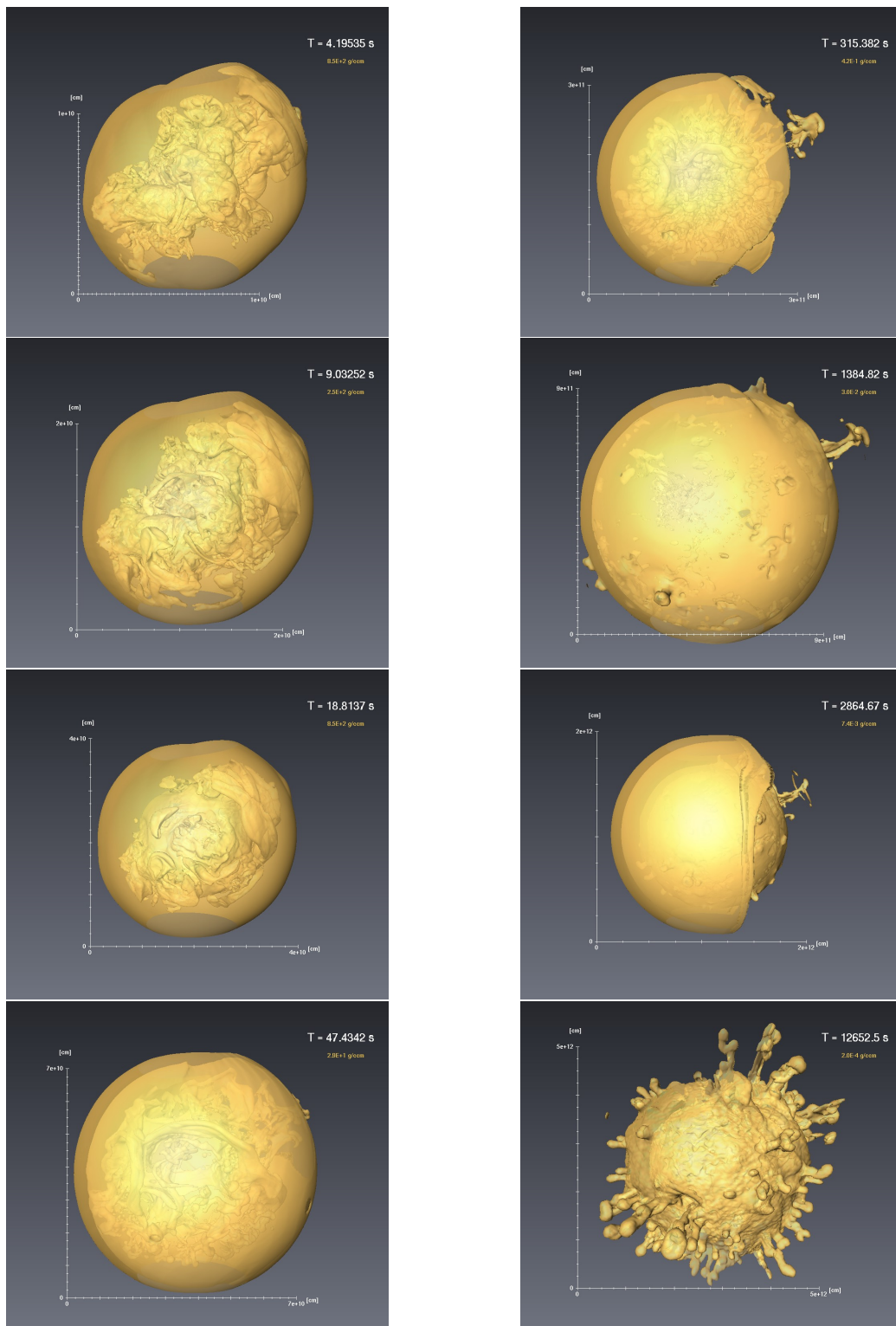


Figure A.8: Series of plots showing the density structure of model 3D3 evolving with time. Each plot shows the density iso-contour showing a maximum of the substructure contained in the data.

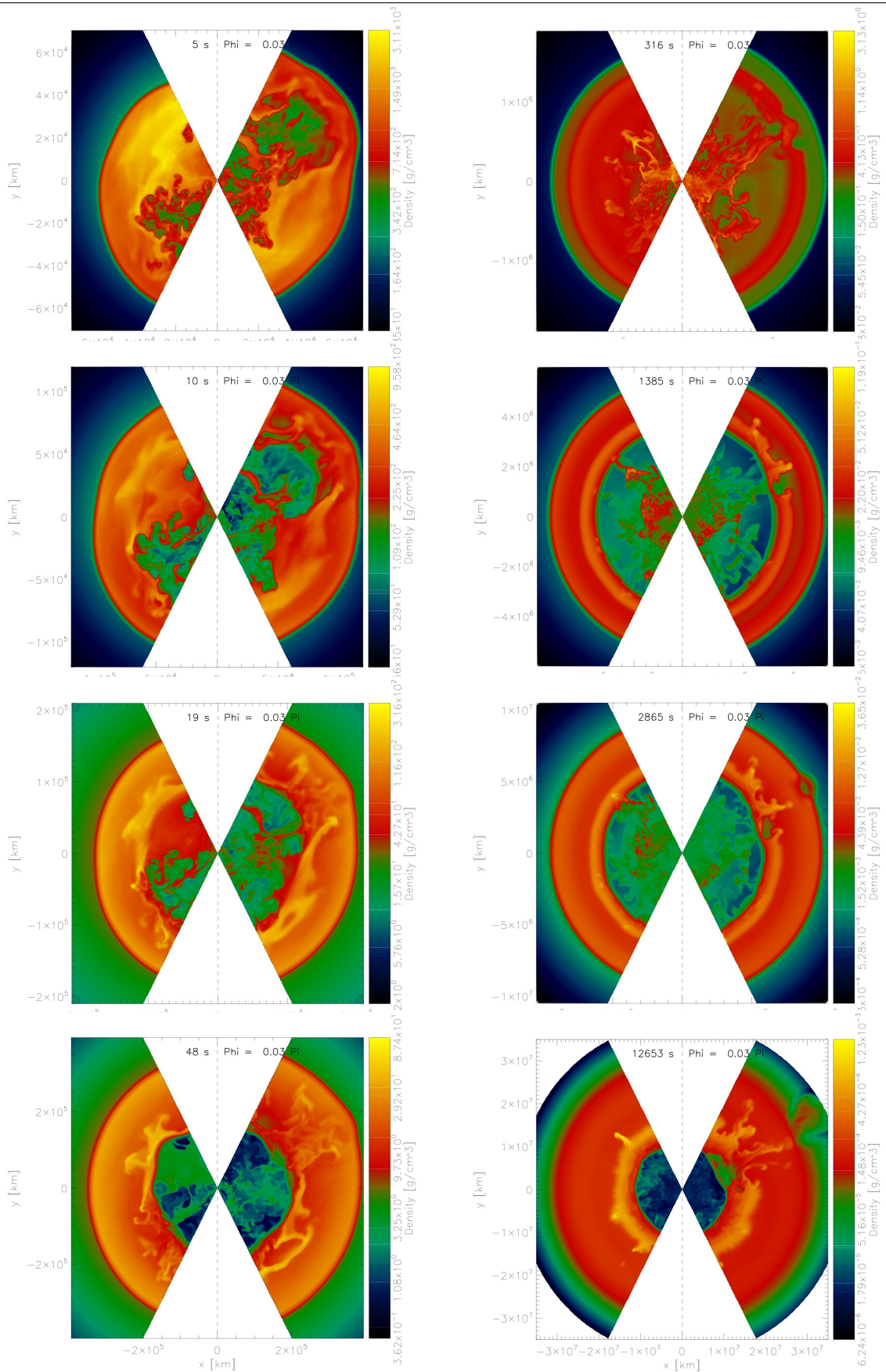


Figure A.9: Series of plots showing the density structure of model 3D3's slice 2 evolving with time.

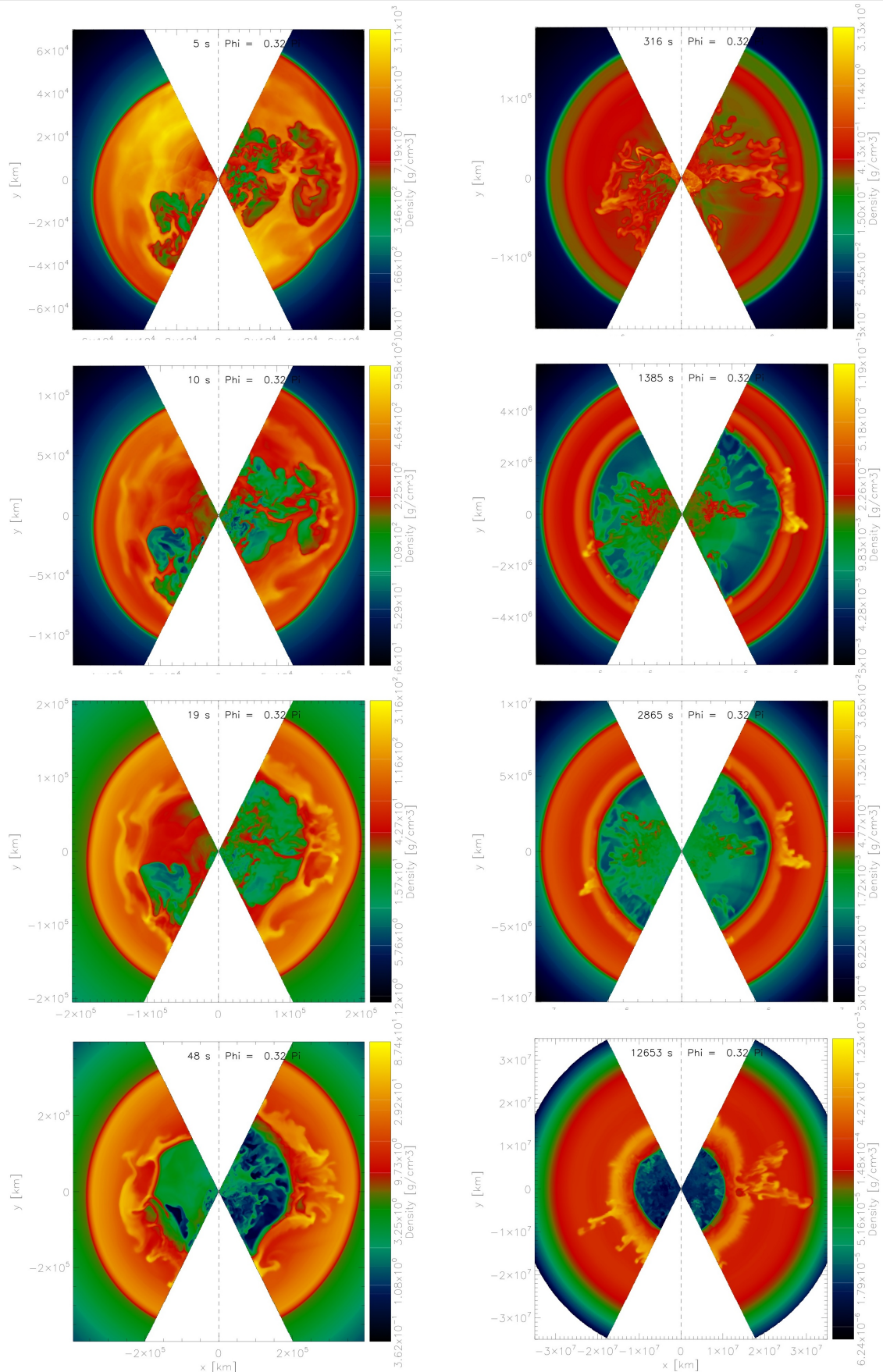


Figure A.10: Series of plots showing the density structure of model 3D3's slice 80 evolving with time. Note the RMI vortex which starts to develop at the (C+O)/He composition interface at a distance of 40 000 km in first panel on the left side near the southern boundary.

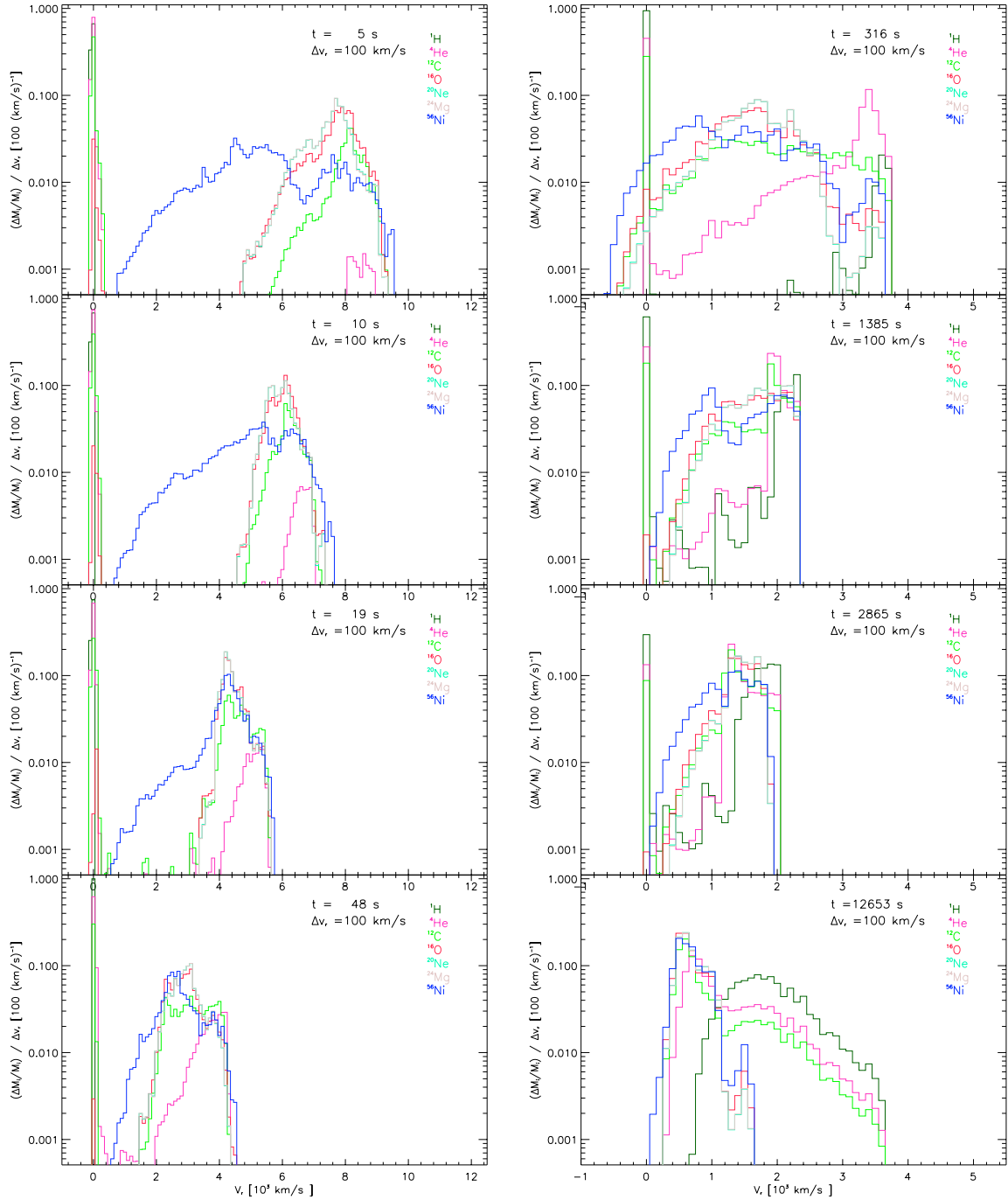


Figure A.11: Same as Figure 6.5, but including only the meridional slice number 2, i.e. the slice at $\phi = 0 \text{ deg}$. Note again the velocity cut off, mentioned already in Figure 6.5

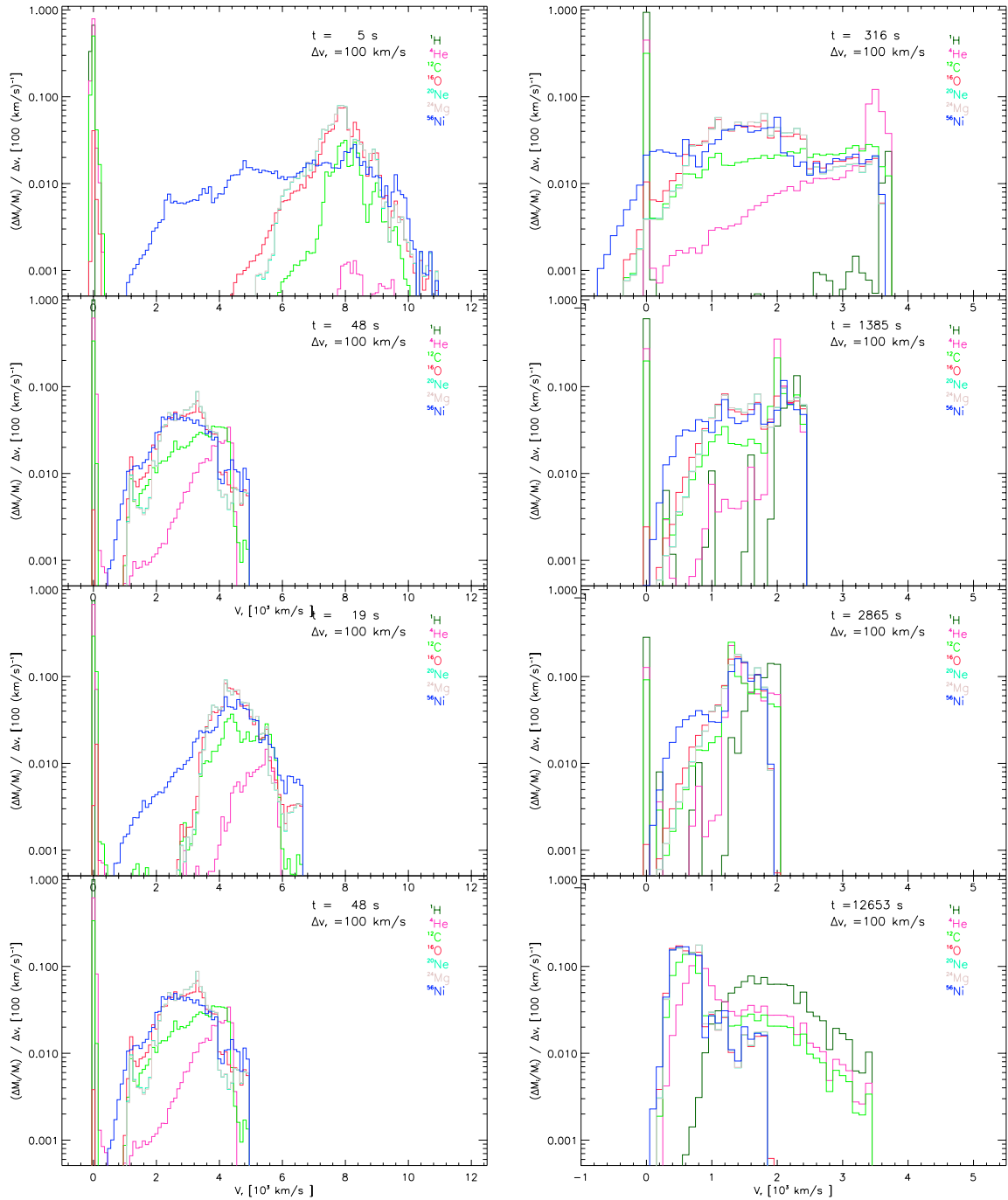


Figure A.12: Same as Figure 6.5, but including only the meridional slice number 80, i.e. the slice at $\phi = 80 \text{ deg}$. Note again the velocity cut off, mentioned already in Figure A.12

1.3 Additional Plots Model 3D2

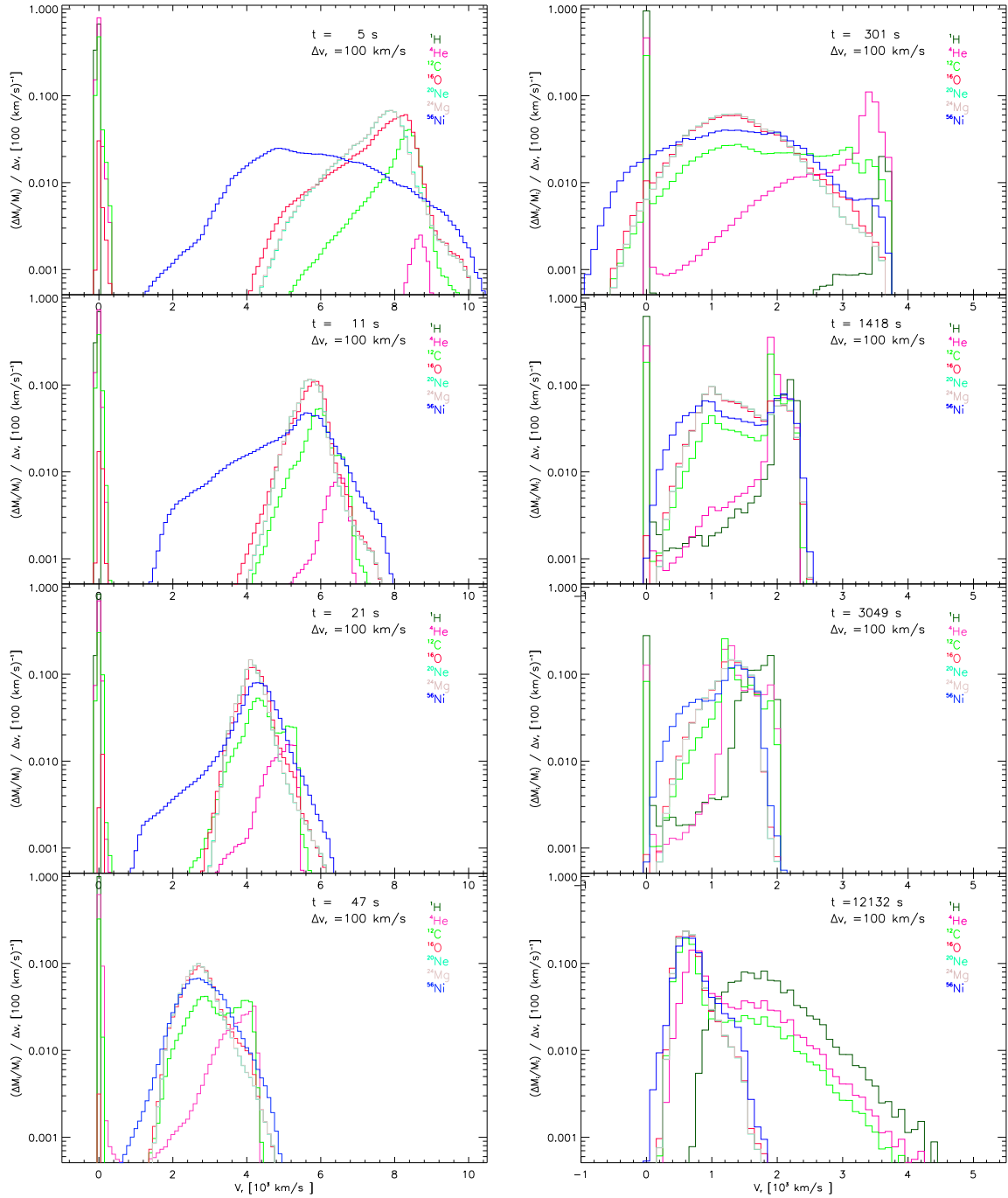


Figure A.13: Same as Figure 6.5, but for model 3D2. Note again the velocity cut off, mentioned already in Figure 6.5

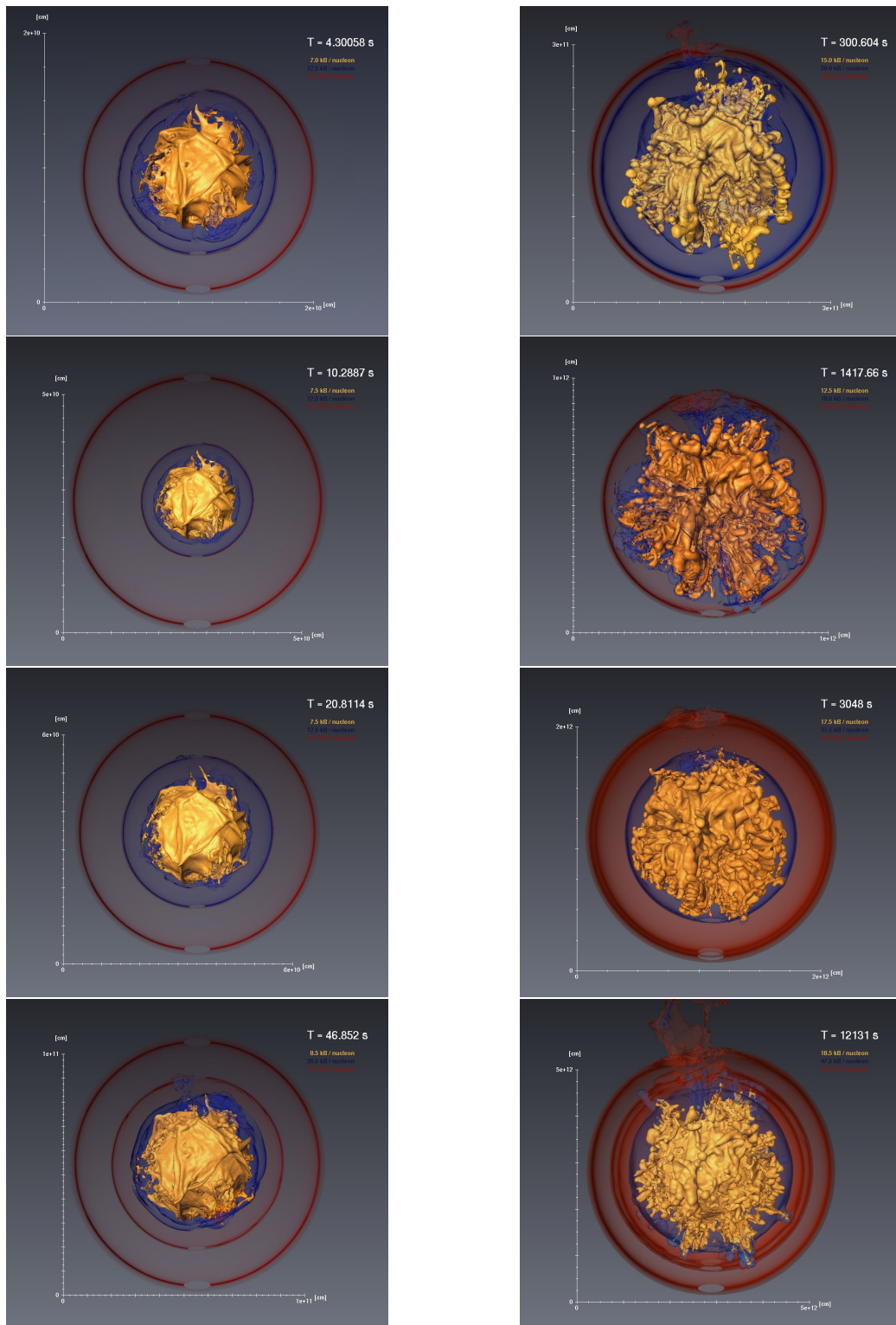


Figure A.14: Series of plots showing the entropy structure of model 3D2 evolving with time. Each plot shows a set of three entropy iso-contours, chosen to visualise a maximum of the substructure contained in the data.

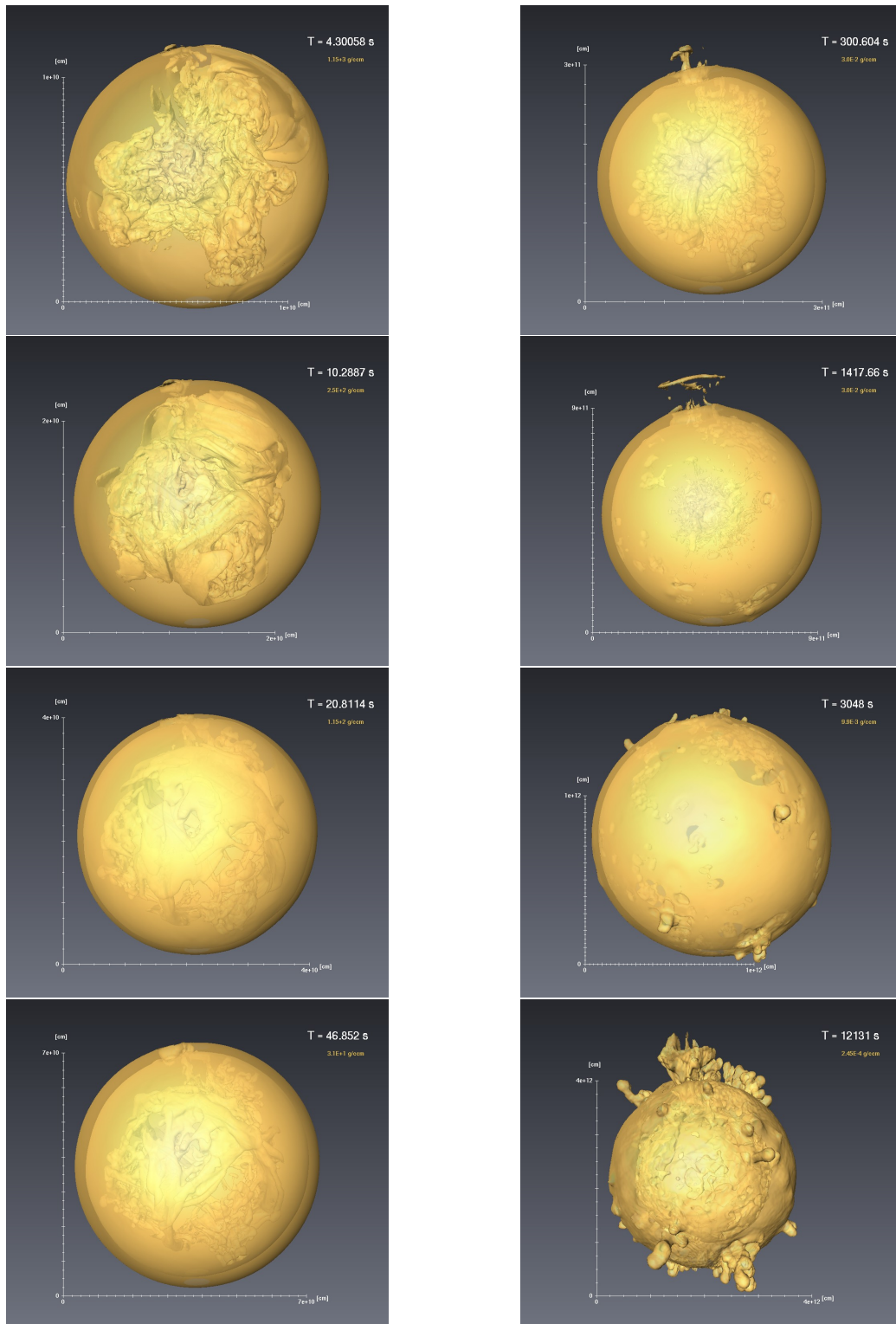


Figure A.15: Series of plots showing the density structure of model 3D2 evolving with time. Each plot shows the density iso-contour showing a maximum of the substructure contained in the data.

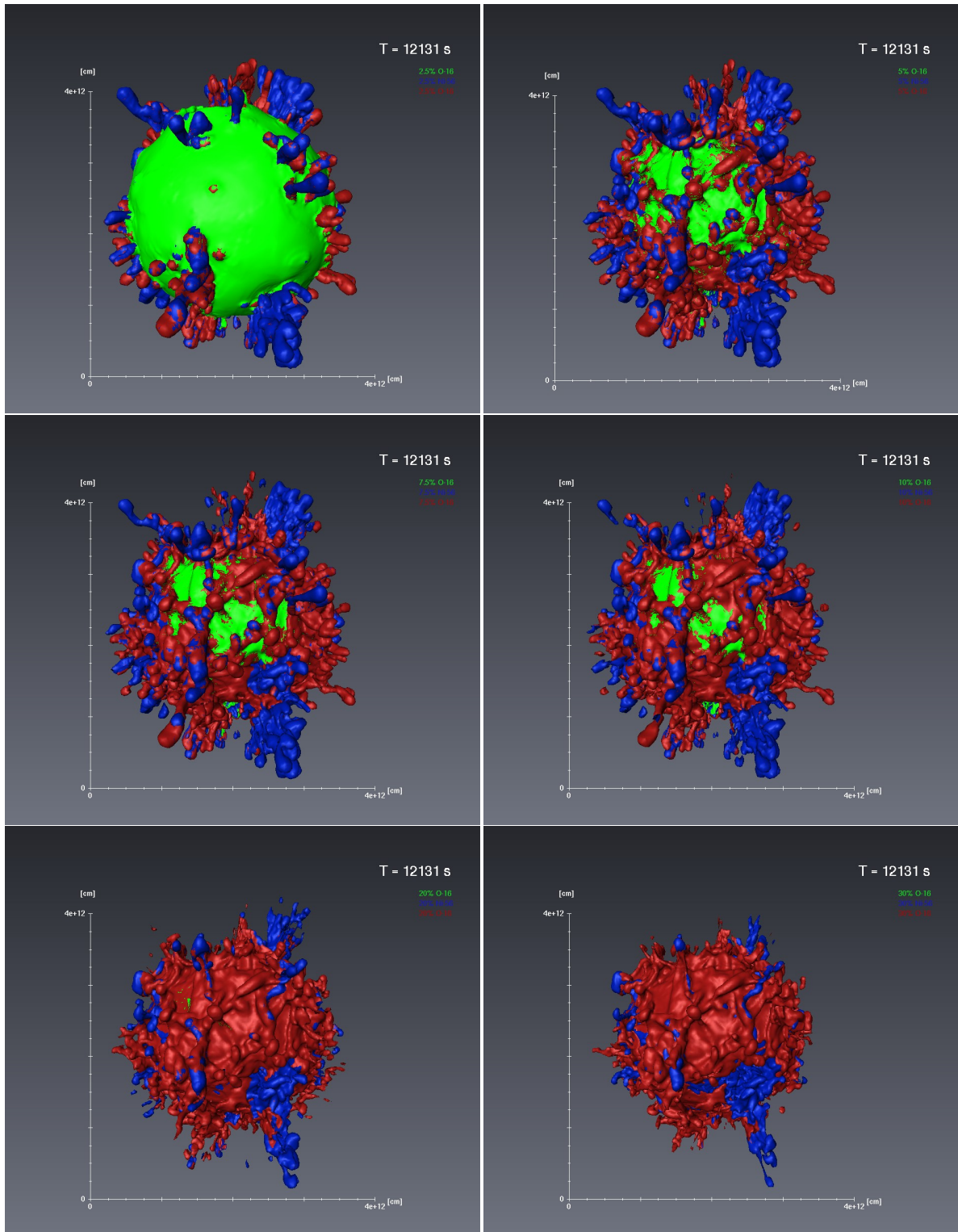


Figure A.16: Same as Figure 6.12, but for model 3D2.

1.4 Additional Plots Model 2D2

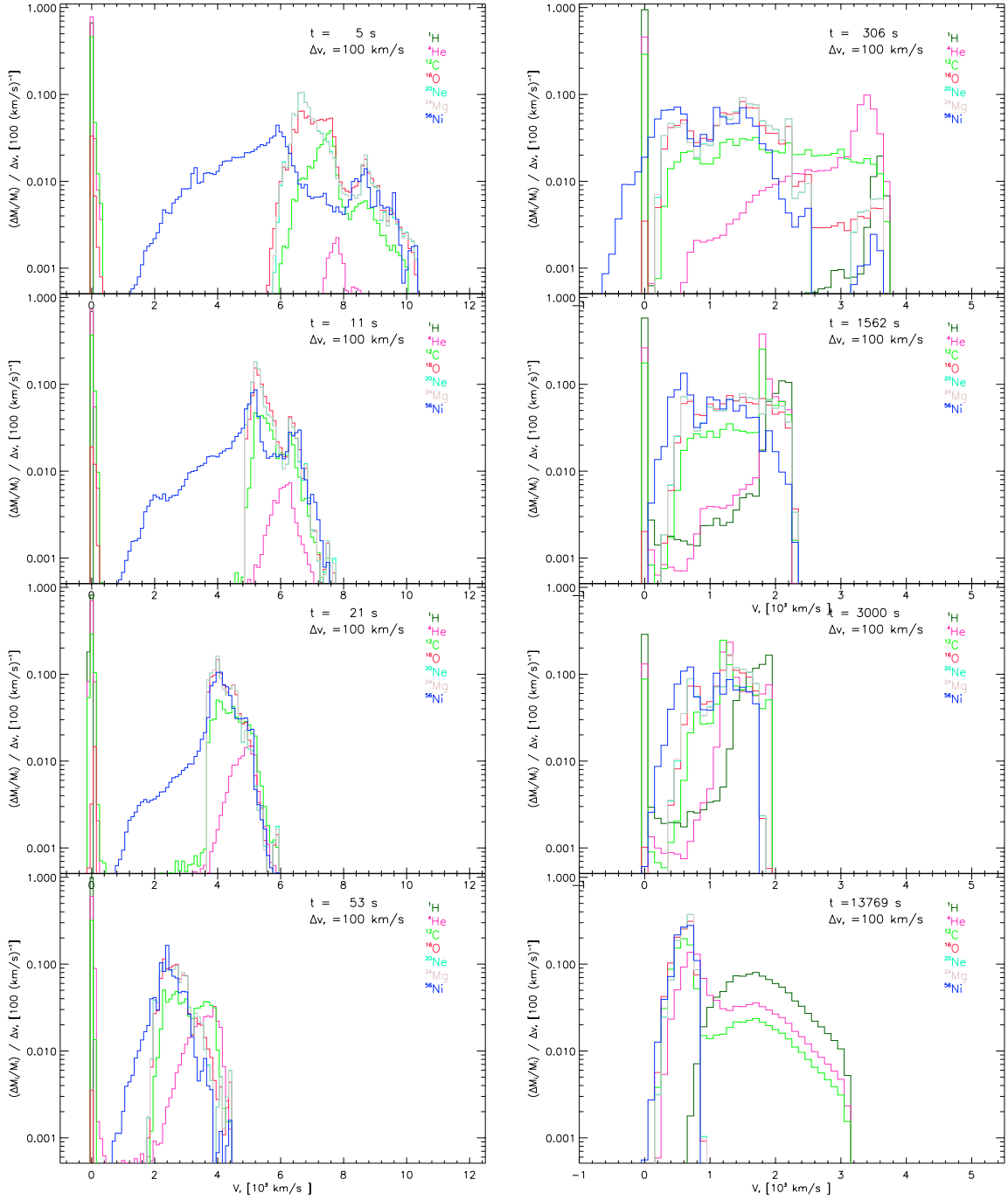


Figure A.17: Same as Figure 6.5, but for model 2D2. Note again the velocity cut off, mentioned already in Figure 6.5

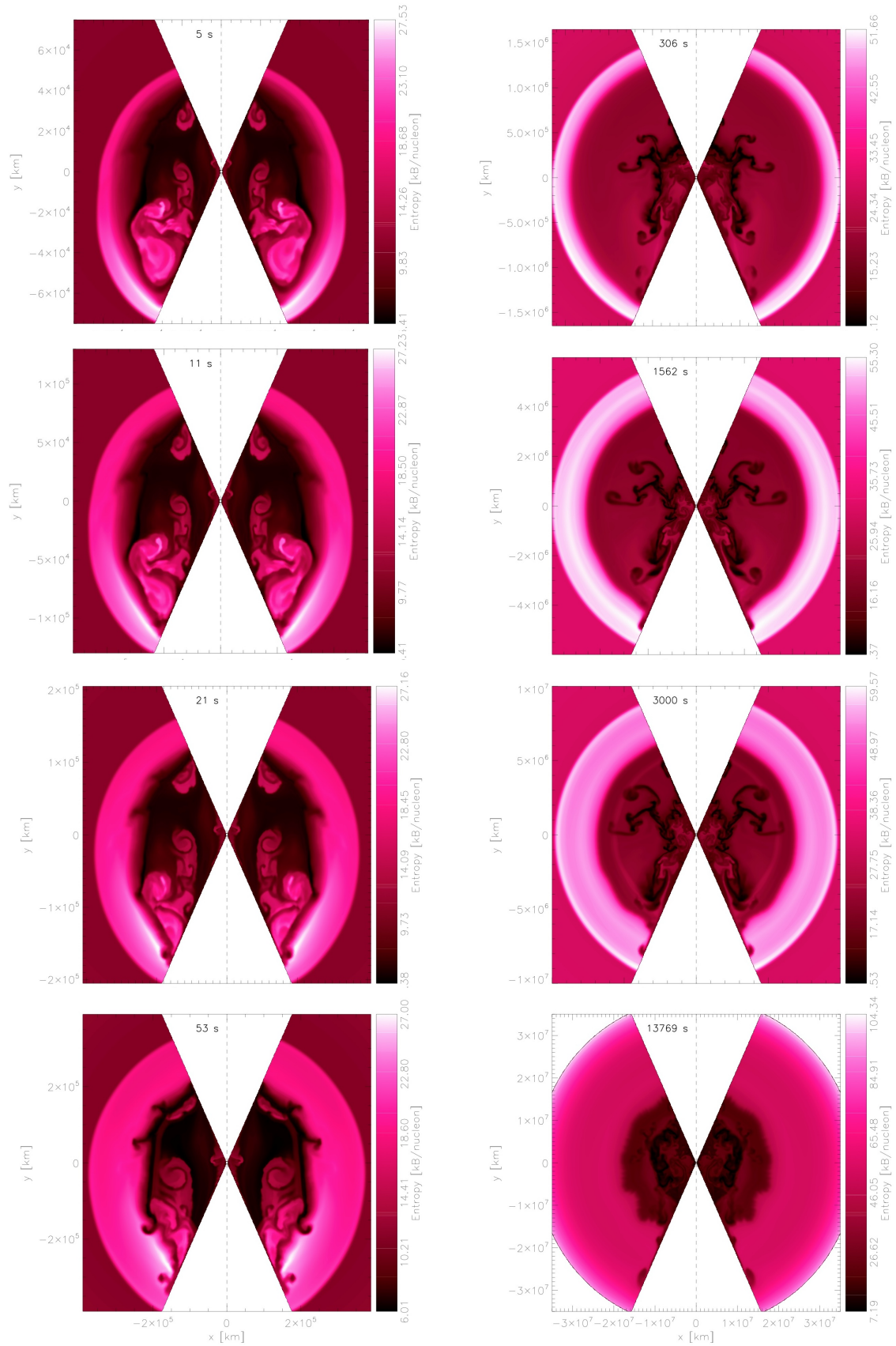


Figure A.18: Series of plots showing the entropy structure of model 2D2 evolving with time.

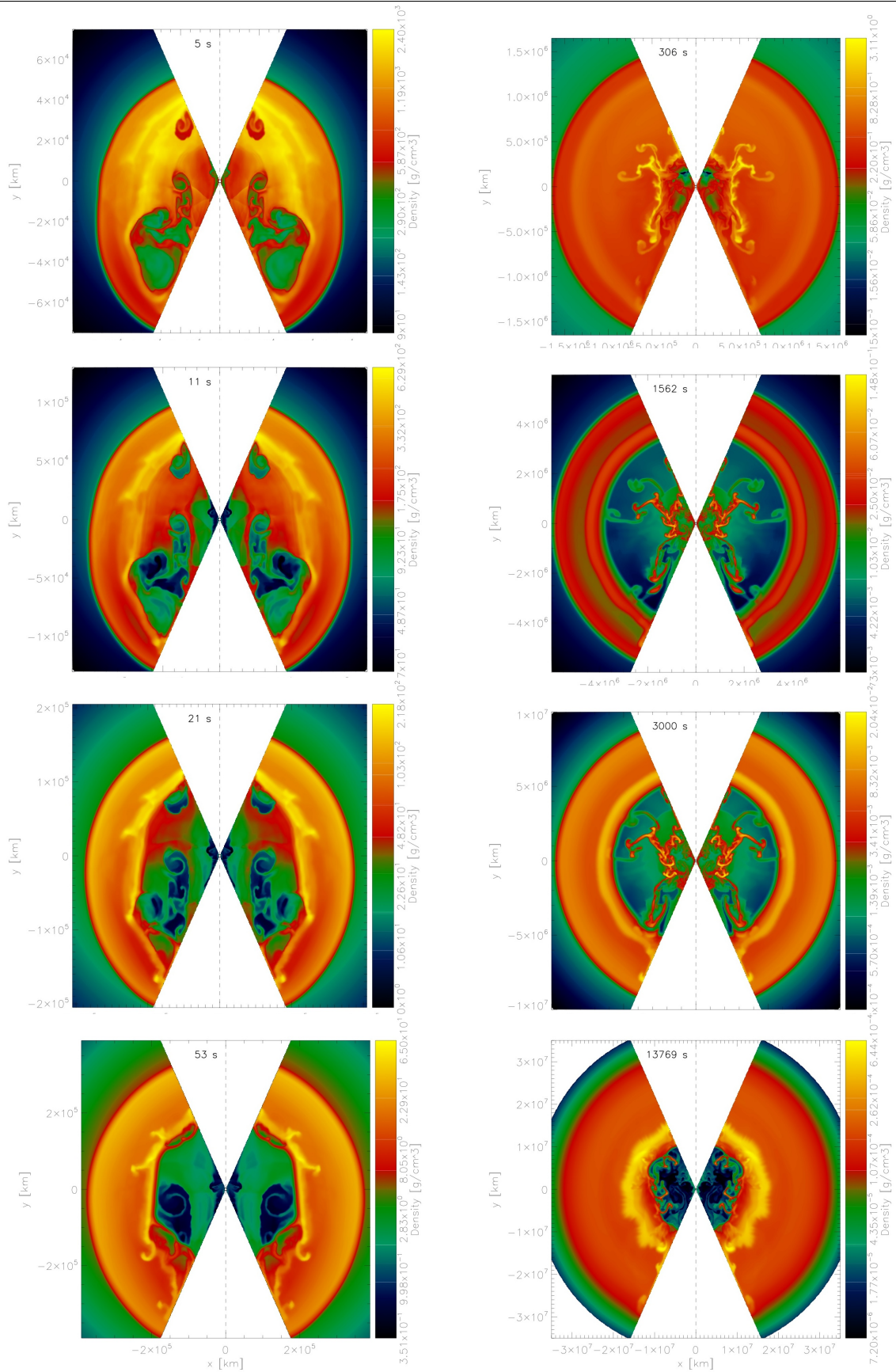


Figure A.19: Series of plots showing the density structure of model 2D2 evolving with time.

1.5 Additional Plots Model 2D80

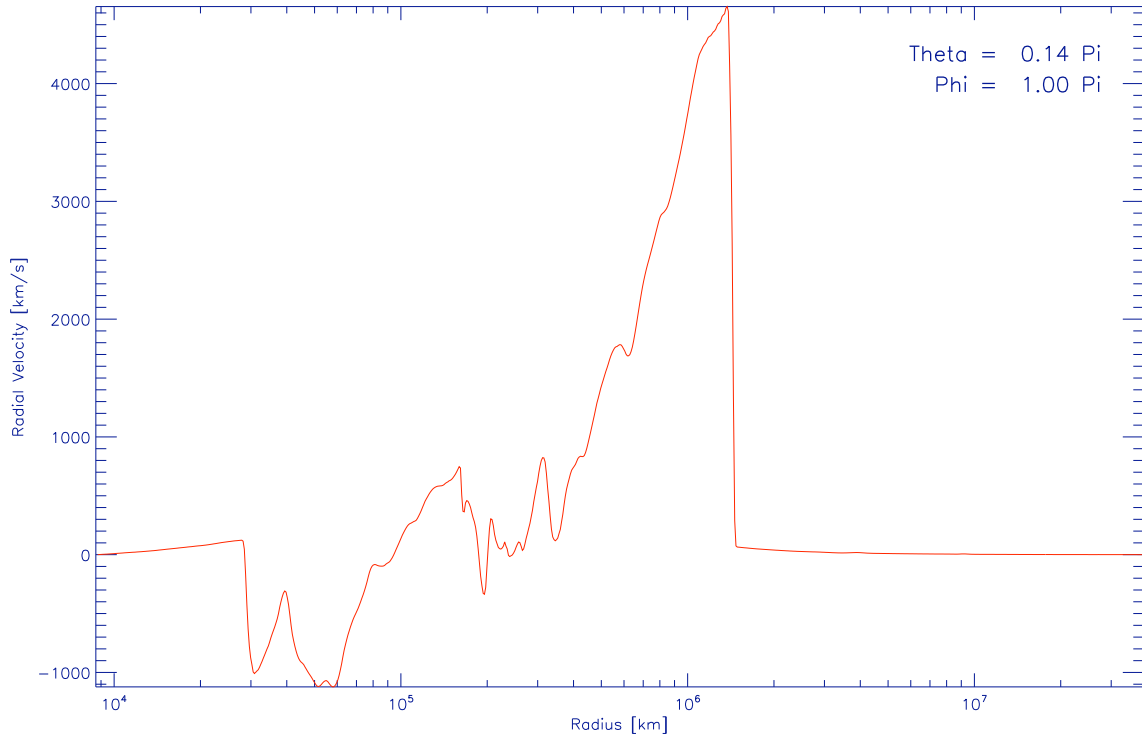


Figure A.20: Representative 1D velocity profile of model 2D80 at approximately the time (216 s) when the shock wave is passing the H/He interface.

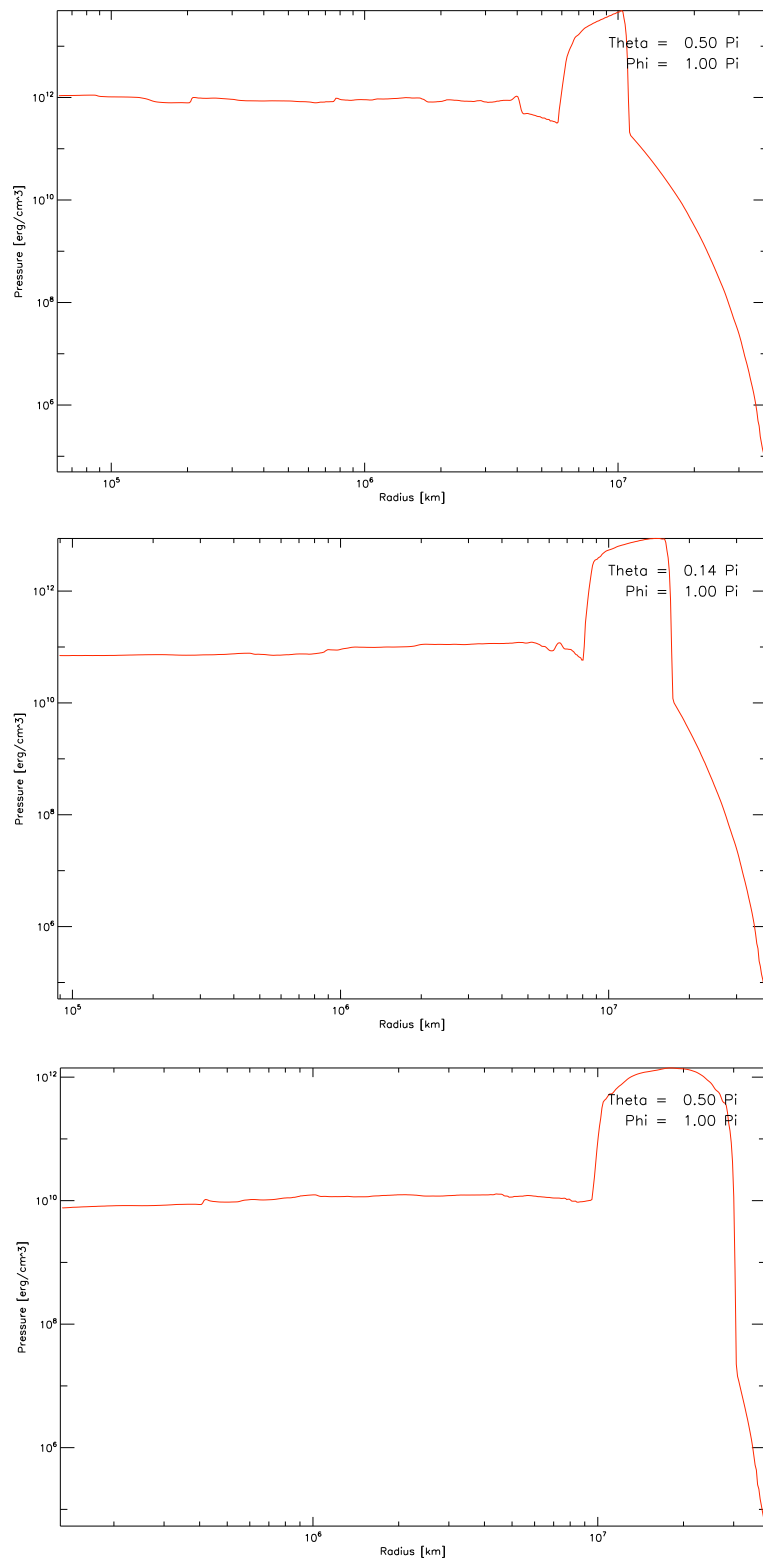


Figure A.21: Time sequence of representative 1D velocity profile of model 2D80 at the epochs 3019 s, 4965 s and 8309 s (from top to bottom). The “bump” moving towards the right represents the pressure profile of the “helium wall” (Subsection 6.4.2), with the shock wave being the right edge and the reverse shock being the left edge of the “bump”.

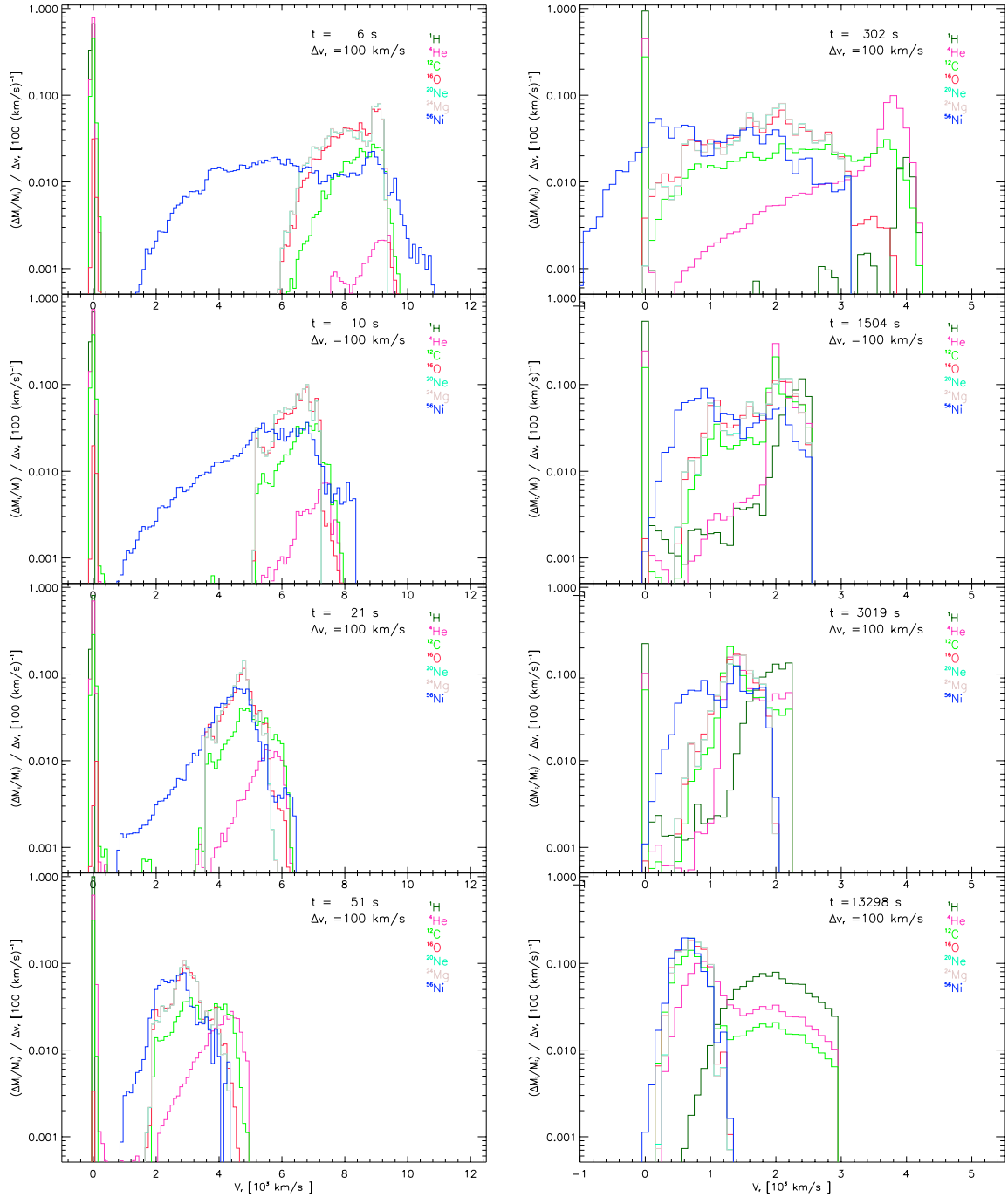


Figure A.22: Same as Figure 6.5, but for model 2D80. Note again the velocity cut off, mentioned already in Figure 6.5

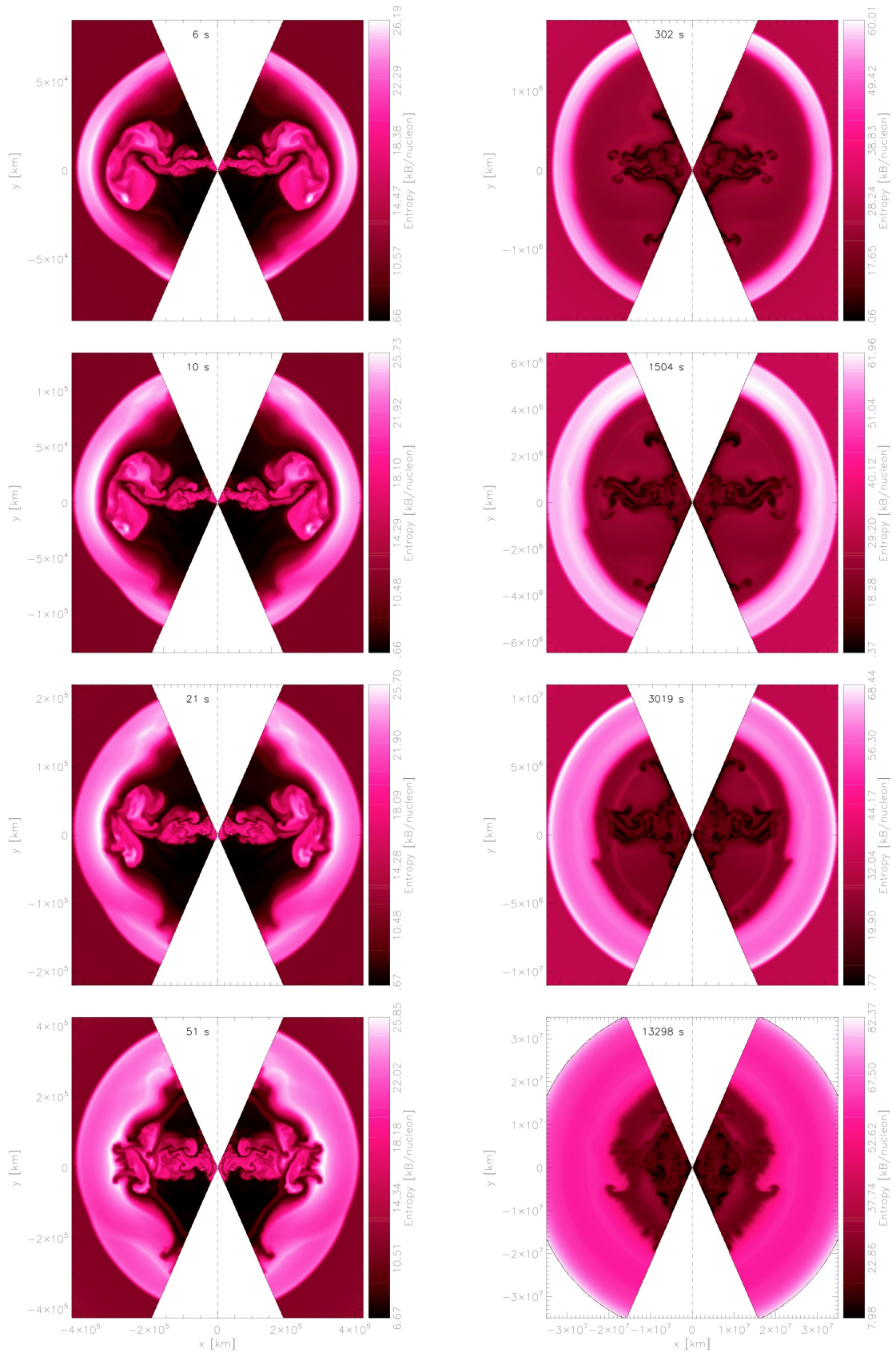


Figure A.23: Series of plots showing the entropy structure of model 2D80 evolving with time.

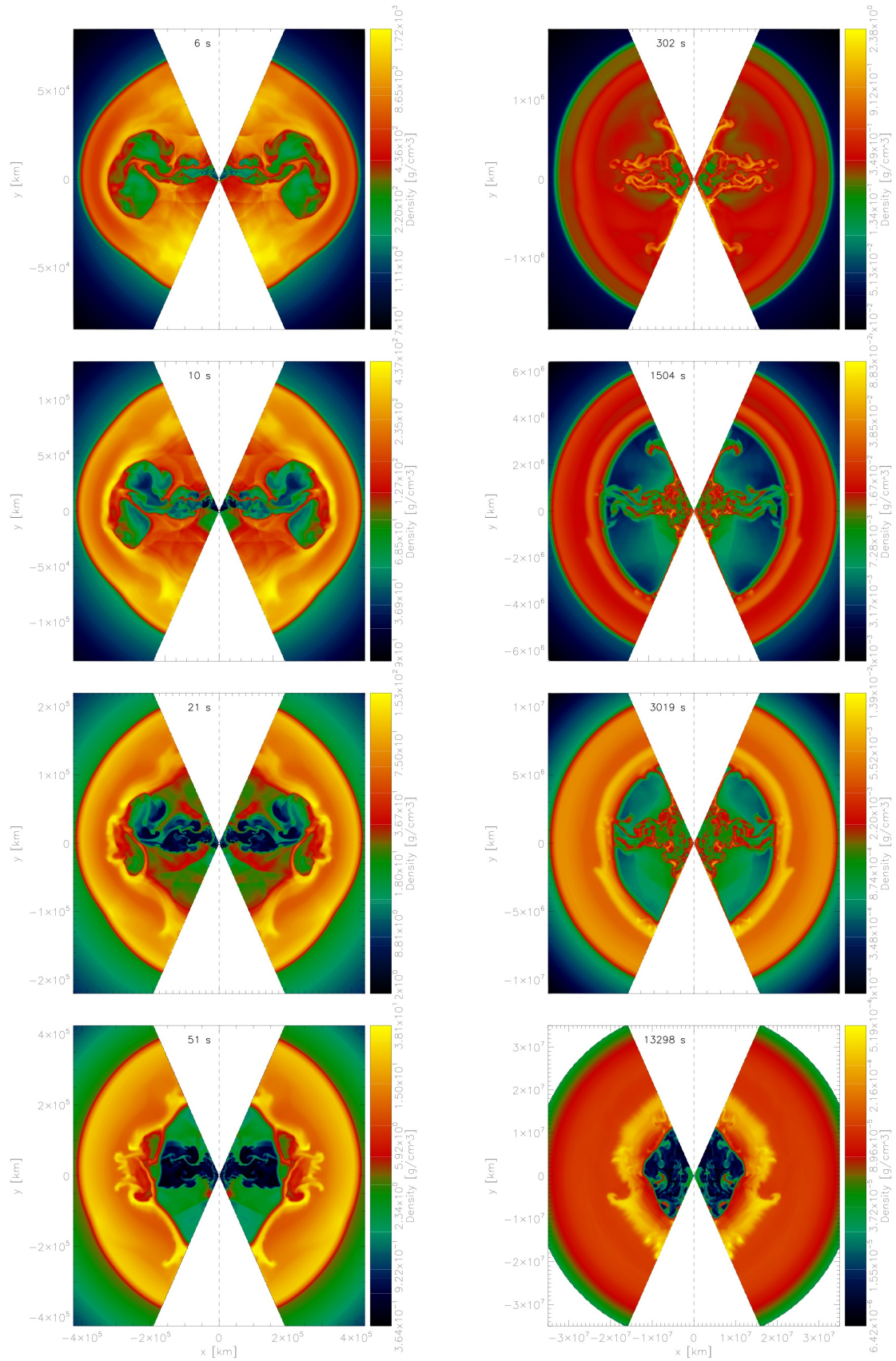


Figure A.24: Series of plots showing the density structure of model 2D80 evolving with time.

Appendix B

Definitions & Abbreviations

Table B.1: Definitions and abbreviations used in my thesis. Note that all abbreviations are defined when used first in the text.

Å	Old unit, $1 \text{Å} = 0.1 \text{ nm}$
AMR	adaptive mesh refinement
ccSNe	Core collapse supernovae
SN	Supernova
SNe	Supernovae
SNR	Supernova remnant
M_{\odot}	Unit used for stellar masses ² , $1 M_{\odot} = 1.989 \times 10^{33} \text{ g}$
Bethe	Unit used for SN energies, short 1 b, $1 \text{ b} = 10^{51} \text{ erg}$
LOTOSS	Lick Observatory and the Tenagra Observatory Supernova Searches
CTIO	Tololo Inter-American Observatory
SAAO	South African Astronomical Observatory
PNS	proto-neutron star
EOS	Equation of state
SASI	Standing accretion shock instability
RTI	Rayleigh-Taylor instability
KHI	Kelvin-Helmholtz instability
RMI	Richtmyer-Meshkov instability
PPM	Piecewise Parabolic Method
CFL	Courant-Friedrich-Levy
σ	Stefan-Boltzmann radiation constant ³ $\sigma = 5.67 \times 10^{-8} \text{ W m}^{-2} \text{ K}^{-4}$

²Numerical value from Zimmermann & Weigert (1999)

³Numerical value from Cohen & Taylor (1987) as given in Bronstein et al. (1999)

Appendix C

Mathematics

3.1 Spherical Polar Coordinates

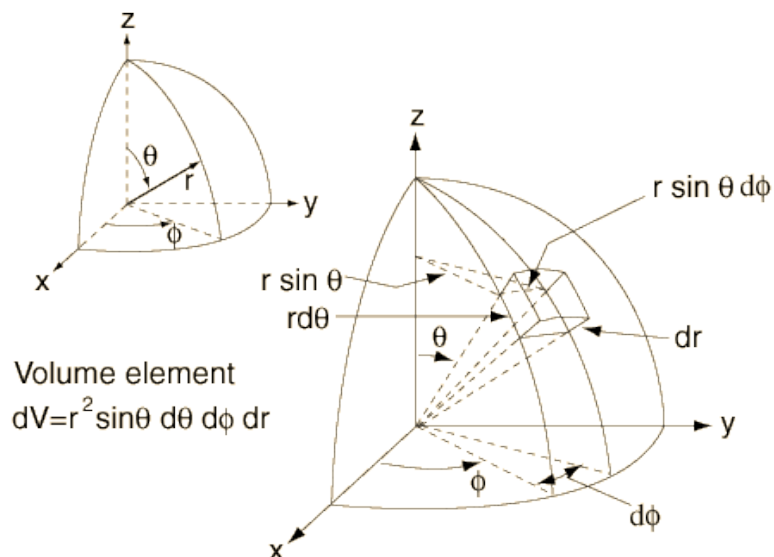


Figure C.1: Definition of spherical polar coordinates. Figure from *HyperMath Homepage* by C.R. Nave

3.2 Vector Operators in Cartesian Coordinates

Note that the vector operators given in Section 3.2 and Section 3.3, were taken from Bronstein et al. (1999). First we need the line element which is given in planar geometry as

$$d\vec{r} = \vec{e}_x dx + \vec{e}_y dy + \vec{e}_z dz \quad (\text{C.1})$$

and the Nabla operator in cartesian coordinates

$$\vec{\nabla} = \frac{\partial}{\partial x} \vec{e}_x + \frac{\partial}{\partial y} \vec{e}_y + \frac{\partial}{\partial z} \vec{e}_z \quad (\text{C.2})$$

Therewith we can express the divergence as

$$\operatorname{div}(\vec{V}) = \vec{\nabla} \cdot \vec{V} = \frac{\partial V_x}{\partial x} + \frac{\partial V_y}{\partial y} + \frac{\partial V_z}{\partial z} \quad , \quad (\text{C.3})$$

the gradient as

$$\operatorname{grad} U = \vec{\nabla} U = \frac{\partial U}{\partial x} \vec{e}_x + \frac{\partial U}{\partial y} \vec{e}_y + \frac{\partial U}{\partial z} \vec{e}_z \quad , \quad (\text{C.4})$$

and the vector gradient as

$$(\vec{a} \operatorname{grad}) \vec{V} = (\vec{a} \vec{\nabla}) \vec{V} = \begin{pmatrix} \frac{\partial V_x}{\partial x} & \frac{\partial V_x}{\partial y} & \frac{\partial V_x}{\partial z} \\ \frac{\partial V_y}{\partial x} & \frac{\partial V_y}{\partial y} & \frac{\partial V_y}{\partial z} \\ \frac{\partial V_z}{\partial x} & \frac{\partial V_z}{\partial y} & \frac{\partial V_z}{\partial z} \end{pmatrix} \begin{pmatrix} a_x \\ a_y \\ a_z \end{pmatrix} \quad . \quad (\text{C.5})$$

$$(\vec{a} \operatorname{grad}) \vec{V} = (\vec{a} \vec{\nabla}) \vec{V} = \begin{pmatrix} \frac{\partial V_y}{\partial x} & \frac{\partial V_y}{\partial y} & \frac{\partial V_y}{\partial z} \\ \frac{\partial V_z}{\partial x} & \frac{\partial V_z}{\partial y} & \frac{\partial V_z}{\partial z} \end{pmatrix} \begin{pmatrix} a_x \\ a_y \\ a_z \end{pmatrix} \quad . \quad (\text{C.6})$$

$$\begin{pmatrix} \frac{\partial V_x}{\partial x} & \frac{\partial V_x}{\partial y} & \frac{\partial V_x}{\partial z} \\ \frac{\partial V_y}{\partial x} & \frac{\partial V_y}{\partial y} & \frac{\partial V_y}{\partial z} \\ \frac{\partial V_z}{\partial x} & \frac{\partial V_z}{\partial y} & \frac{\partial V_z}{\partial z} \end{pmatrix} \begin{pmatrix} a_x \\ a_y \\ a_z \end{pmatrix} \quad . \quad (\text{C.7})$$

3.3 Vector Operators in Spherical Polar Coordinates

First we need the line element which is given in spherical polar coordinates as

$$d\vec{r} = \vec{e}_r dr + \vec{e}_\theta r d\theta + \vec{e}_\phi r \sin\theta d\phi \quad (\text{C.8})$$

and the Nabla operator in spherical polar coordinates

$$\vec{\nabla} = \frac{1}{r^2} \frac{\partial}{\partial r} \vec{e}_r + \frac{1}{r \sin\theta} \frac{\partial}{\partial \theta} \vec{e}_\theta + \frac{1}{r \sin\theta} \frac{\partial}{\partial \phi} \vec{e}_\phi \quad . \quad (\text{C.9})$$

Therewith we can express the divergence in spherical polar coordinates as

$$\operatorname{div}(\vec{V}) = \vec{\nabla} \cdot \vec{V} = \frac{1}{r^2} \frac{\partial (r^2 V_r)}{\partial r} + \frac{1}{r \sin\theta} \frac{\partial (\sin\theta V_\theta)}{\partial \theta} + \frac{1}{r \sin\theta} \frac{\partial V_\phi}{\partial \phi} \quad , \quad (\text{C.10})$$

the gradient as

$$\operatorname{grad} U = \vec{\nabla} U = \frac{\partial U}{\partial r} \vec{e}_r + \frac{1}{r} \frac{\partial U}{\partial \theta} \vec{e}_\theta + \frac{1}{r \sin\theta} \frac{\partial U}{\partial \phi} \vec{e}_\phi \quad , \quad (\text{C.11})$$

and the vector gradient as

$$(\vec{a} \operatorname{grad}) \vec{V} = (\vec{a} \vec{\nabla}) \vec{V} = \begin{pmatrix} \frac{\partial V_r}{\partial r} & \frac{1}{r} \frac{\partial V_r}{\partial \theta} & \frac{1}{r \sin\theta} \frac{\partial V_r}{\partial \phi} \\ \frac{\partial V_\theta}{\partial r} & \frac{1}{r} \frac{\partial V_\theta}{\partial \theta} & \frac{1}{r \sin\theta} \frac{\partial V_\theta}{\partial \phi} \\ \frac{\partial V_\phi}{\partial r} & \frac{1}{r} \frac{\partial V_\phi}{\partial \theta} & \frac{1}{r \sin\theta} \frac{\partial V_\phi}{\partial \phi} \end{pmatrix} \begin{pmatrix} a_r \\ a_\theta \\ a_\phi \end{pmatrix} \quad . \quad (\text{C.12})$$

$$(\vec{a} \operatorname{grad}) \vec{V} = (\vec{a} \vec{\nabla}) \vec{V} = \begin{pmatrix} \frac{\partial V_r}{\partial r} & \frac{1}{r} \frac{\partial V_\theta}{\partial \theta} & \frac{1}{r \sin\theta} \frac{\partial V_\theta}{\partial \phi} \\ \frac{\partial V_\theta}{\partial r} & \frac{1}{r} \frac{\partial V_\phi}{\partial \theta} & \frac{1}{r \sin\theta} \frac{\partial V_\phi}{\partial \phi} \end{pmatrix} \begin{pmatrix} a_r \\ a_\theta \\ a_\phi \end{pmatrix} \quad . \quad (\text{C.13})$$

$$\begin{pmatrix} \frac{\partial V_r}{\partial r} & \frac{1}{r} \frac{\partial V_r}{\partial \theta} & \frac{1}{r \sin\theta} \frac{\partial V_r}{\partial \phi} \\ \frac{\partial V_\theta}{\partial r} & \frac{1}{r} \frac{\partial V_\theta}{\partial \theta} & \frac{1}{r \sin\theta} \frac{\partial V_\theta}{\partial \phi} \\ \frac{\partial V_\phi}{\partial r} & \frac{1}{r} \frac{\partial V_\phi}{\partial \theta} & \frac{1}{r \sin\theta} \frac{\partial V_\phi}{\partial \phi} \end{pmatrix} \begin{pmatrix} a_r \\ a_\theta \\ a_\phi \end{pmatrix} \quad . \quad (\text{C.14})$$

Bibliography

- Arcones A., Janka H.T., Scheck L., 2007, *A&A* 467, 1227
- Arnett D., 2000, *ApJS* 127, 213
- Arnett D., Fryxell B., Müller E., 1989a, *ApJL* 341, L63
- Arnett W.D., 1987, *ApJ* 319, 136
- Arnett W.D., Bahcall J.N., Kirshner R.P., Woosley S.E., 1989b, *ARA&A* 27, 629
- Baade W., Zwicky F., 1934, *Proceedings of the National Academy of Science* 20, 254
- Bell G.I., 1951, “Taylor Instability on Cylinders and Spheres in the Small Amplitude Approximation”, Los Alamos National Laboratory report LA-1321
- Benz W., Thielemann F.K., 1990, *ApJL* 348, L17
- Bethe H.A., 1990, *Reviews of Modern Physics* 62, 801
- Bionta R.M., Blewitt G., Bratton C.B., et al., 1987, *Physical Review Letters* 58, 1494
- Blondin J.M., Mezzacappa A., 2005, In: *Bulletin of the American Astronomical Society*, Vol. 37. *Bulletin of the American Astronomical Society*, p.1181
- Blondin J.M., Mezzacappa A., 2006, In: *Bulletin of the American Astronomical Society*, Vol. 38. *Bulletin of the American Astronomical Society*, p.1099
- Blondin J.M., Mezzacappa A., 2007, *Nat* 445, 58
- Blondin J.M., Mezzacappa A., DeMarino C., 2003, *ApJ* 584, 971
- Blondin J.M., Shaw S., 2007, *ApJ* 656, 366
- Blumen W., 1970, *J. Fluid Mech.* 70, 769
- Bowers R.L., Wilson J.R., 1982, *ApJS* 50, 115
- Bratton C.B., Casper D., Ciocio A., et al., 1988, *Phys. Rev. D* 37, 3361
- Bronstein I.N., Semandjajew K.A., Musiol G., Mühlig H., 1999, *Taschenbuch der Mathematik*, Verlag Harri Deutsch, Frankfurt am Main, fourth edition
- Brouillette M., 2002, *Annu. Rev. Fluid Mech.* 34, 445 arjournals.annualreviews.org by DFG
- Bruenn S.W., 1993, In: Guidry M.W., Strayer M.R. (eds.) *Nuclear Physics in the Universe.*, p.31
- Buras R., Rampp M., Janka H.T., Kifonidis K., 2006, *A&A* 447, 1049
- Chandrasekhar S., 1961, *Hydrodynamic and hydro-magnetic stability*, International Series of Monographs on Physics, Oxford: Clarendon, 1961
- Chevalier R.A., Fransson C., 1987, *Nat* 328, 44
- Chevalier R.A., Soker N., 1989, *ApJ* 341, 867
- Cohen E.R., Taylor B.N., 1987, *Reviews of Modern Physics* 59, 1121
- Colella P., Glaz H.M., 1985, *Journal of Computational Physics* 59, 264
- Colella P., Woodward P.R., 1984, *Journal of Computational Physics* 54, 174
- Colgate S.A., Johnson M.H., 1960, *Physical Review Letters* 5, 235
- Colgate S.A., White R.H., 1966, *ApJ* 143, 626
- Douvion T., Lagage P.O., Cesarsky C.J., 1999, *A&A* 352, L111
- Douvion T., Lagage P.O., Cesarsky C.J., 2000, *New Astronomy Review* 44, 341
- Ebisuzaki T., Shigeyama T., Nomoto K., 1989, *ApJL* 344, L65
- Einfeldt B., 1988, *SIAM J. Num. Ana.* 25
- Fabian A.C., Rees M.J., van den Heuvel E.P.J., van Paradijs J., 1987, *Nat* 328, 323
- Fassia A., Meikle W.P.S., 1999, *MNRAS* 302, 314
- Fassia A., Meikle W.P.S., Geballe T.R., et al., 1998, *MNRAS* 299, 150
- Fermi E., 1951, “Taylor Instability of an Incompressible Fluid”, Document AECU-2979 Part I
- Fermi E., von Neumann J., 1953, “Taylor Instability at the Boundary of Two Incompressible Liquid”, Document AECU-2979 Part II
- Fesen R.A., Hammell M.C., Morse J., et al., 2006, *ApJ* 636, 859
- Filippenko A.V., 1997, *ARA&A* 35, 309
- Foglizzo T., 2002, *A&A* 392, 353
- Foglizzo T., Galletti P., Scheck L., Janka H.T., 2007, *ApJ* 654, 1006
- Fowler W.A., Hoyle F., 1964, *ApJS* 9, 201
- Fraley G., 1986, *Phys. Fluids* 29, 376
- Fryxell B., Arnett D., Müller E., 1991, *ApJ* 367, 619
- Gerthsen C., 1997, *Gerthsen Physik*, Springer-Lehrbuch, Springer, Berlin [[u.a.], 19. aufl. edition
- Gerwin R.A., 1968, *Rev. Mod. Phys.* 40, 652
- Haas M.R., Erickson E.F., Lord S.D., et al., 1990, *ApJ* 360, 257
- Hanuschik R.W., 1988, *Proceedings of the Astronomical Society of Australia* 7, 446
- Hanuschik R.W., Dachs J., 1987a, In: Danziger I.J. (ed.) *ESO Workshop on SN 1987 A.*, p.153
- Hanuschik R.W., Dachs J., 1987b, *A&A* 182, L29+
- Harkness R.P., Wheeler J.C., 1990, In: *Supernovae*, p.

- 1 - 29., p.1
- Helmholtz H., 1882, *Wissenschaftliche Abhandlungen* 146–157 J. A. Barth, Leipzig
- Herant M., Benz W., 1991, *ApJL* 370, L81
- Herant M., Benz W., 1992, *ApJ* 387, 294
- Herant M., Benz W., Colgate S., 1992, *ApJ* 395, 642
- Herant M., Woosley S.E., 1994, *ApJ* 425, 814
- Hillebrandt W., Höflich P., 1989, *Reports of Progress in Physics* 52, 1421
- Hirata K., Kajita T., Koshiha M., et al., 1987, *Physical Review Letters* 58, 1490
- Hirata K.S., Kajita T., Koshiha M., et al., 1988, *Phys. Rev. D* 38, 448
- Holmes R.L., Dimonte G., Fryxell B., et al., 1999, *Journal of Fluid Mechanics* 389, 55
- Howard L.N., Maslowe S.A., 1973, *Boundary-Layer Meterology* 4, 511
- Hoyle F., Fowler W.A., 1960, *ApJ* 132, 565
- Hungerford A.L., Fryer C.L., Warren M.S., 2003, *ApJ* 594, 390
- Janka H.T., 2001, *A&A* 368, 527
- Janka H.T., Langanke K., Marek A., et al., 2007, *Phys. Rep.* 442, 38
- Janka H.T., Müller E., 1996, *A&A* 306, 167
- Kane J., Arnett D., Remington B.A., et al., 1997, *ApJL* 478, L75+
- Kasen D., Woosley S., 2008, in prep.
- Kawabata K.S., Jeffery D.J., Iye M., et al., 2002, *ApJL* 580, L39
- Kelvin L., 1910a, *Mathematical and Physical Papers*, Vol. VI of *Hydrodynamics and General Dynamics*, Ch. Hydrokinetic solutions and observations: On the motion of free solids through a liquid, p.69, *Hydrodynamics and General Dynamics*, Cambridge, England
- Kelvin L., 1910b, *Mathematical and Physical Papers*, Vol. VI of *Hydrodynamics and General Dynamics*, Ch. Hydrokinetic solutions and observations: Influence of wind and capillarity on waves in water supposed frictionless, p.76, *Hydrodynamics and General Dynamics*, Cambridge, England
- Kifonidis K., 2000, Ph.D. thesis, Technische Universität München
- Kifonidis K., Plewa T., Janka H.T., Müller E., 2003, *A&A* 408, 621
- Kifonidis K., Plewa T., Scheck L., et al., 2006, *A&A* 453, 661
- Kopka H., 2000, LATEX Band1: Einführung, Addison-Wesley
- Kotake K., Sato K., Takahashi K., 2006, *Reports of Progress in Physics* 69, 971
- Landau L.D., 1932, *Physik. Zeits. Sowjetunion* 1, 285
- Landau L.D., Lifschitz E.M., 1991, *Lehrbuch der theoretischen Physik (Band 5): Statistische Physik Teil 1*, Verlag Harri Deutsch, nachdruck der 8., korrigierten aufl. 1991 (2008) edition
- Leonard D.C., Filippenko A.V., Ardila D.R., Brotherton M.S., 2001, *ApJ* 553, 861
- Leonard D.C., Filippenko A.V., Barth A.J., Matheson T., 2000, *ApJ* 536, 239
- Leonard D.C., Filippenko A.V., Ganeshalingam M., et al., 2006, *Nat* 440, 505
- Link B., Epstein R.I., Lattimer J.M., 1999, *Phys. Rev. Lett.* 83, 3362
- Liou M.S., 2000, *Journal of Computational Physics* 160, 623
- Mandelbrot B.B., 1974, *Journal of Fluid Mechanics* 62, 331
- Markstein G.H., 1957, *J. Aero. Sci.* 8, 238
- Marschall L.A., 1988, *The supernova story*, New York, Plenum Press, 1988, 313 p.
- Matcher S.J., Meikle W.P.S., Morgan B.L., et al., 1987, *IAU Circ.* 4413, 2
- Maund J.R., Wheeler J.C., Patat F., et al., 2007, *ApJ* 671, 1944
- Mazzali P.A., Kawabata K.S., Maeda K., et al., 2007, *ApJ* 670, 592
- Meikle W.P.S., Matcher S.J., Morgan B.L., 1987, *Nat* 329, 608
- Meshkov E.E., 1969, *Fluid. Dyn.* 4, 101
- Meshkov E.E., 1970, *NASA Tech. Trans.* F-13, 074
- Meshkov E.E., Nevmerzhitsky N.V., Zmushko V.V., 1997, In: Jourdan G., Houas L. (eds.) *The Physics of Compressible Turbulent Mixing.*, Impr. Caratère, Marseille, p.343
- Mezzacappa A., 2005, In: Turatto M., Benetti S., Zampieri L., Shea W. (eds.) *1604-2004: Supernovae as Cosmological Lighthouses*, Vol. 342. *Astronomical Society of the Pacific Conference Series*, p.175
- Mikaelian K.O., 1994, *Physics of Fluids* 6, 356
- Miles J.W., 1957, *Journal of Fluid Mechanics* 3, 185
- Miles J.W., 1959, *Journal of Fluid Mechanics* 6, 583
- Minkowski R., 1941, *PASP* 53, 224
- Mitchell R.C., Baron E., Branch D., et al., 2001, *ApJ* 556, 979
- Müller E., 1997, *Classical and Quantum Gravity* 14, 1455
- Müller E., Fryxell B., Arnett D., 1991, *A&A* 251, 505
- Müller, E. und Hillebrandt W., 2005, *Hydrodynamik: Grundlagen und numerische Verfahren*, <http://www.mpa->

- garching.mpg.de/lectures/HYDRO/
- Nisenson P., Papaliolios C., Karovska M., Noyes R., 1987, *ApJL* 320, L15
- Nomoto K., Shigeyama T., Kumaga S., Hashimoto M.A., 1988, In: Couch W. (ed.) *Elizabeth and Frederick White Symposium on Supernova 1987A*, Vol. 7. *Proceedings of the Astronomical Society of Australia*, p.490
- Pfennig G., Klewe-Nebenius H., Seelmann-Eggebert W., 1995, *Karlsruhe Nuklidkarte*, Technical Report 6th, rev. 1998, Institut für Radiochemie, Kernforschungszentrum Karlsruhe GmbH
- Plewa T., Müller E., 1999, *A&A* 342, 179
- Plewa T., Müller E., 2001, *Computer Physics Communications* 138, 101
- Quirk J.J., 1994, *International Journal for Numerical Methods in Fluids* 18, 555
- Quirk J.J., 1998, In: Hussaini M.Y., van Leer V., van Rosendale J. (eds.) *Upwind and High-Resolution Schemes*, Vol. 17. *European Journal of Mechanics - B/Fluids* 4, Springer
- Rampp M., Janka H.T., 2002, *A&A* 396, 361
- Richtmyer R.D., 1960, *Comm. Pure Appl. Maths* 13, 297
- Rutledge R.E., Bildsten L., Brown E.F., et al., 2001, *ApJ* 559, 1054
- Scheck L., Foglizzo T., Kifonidis K., et al., 2006a, unpublished (priv. comm.)
- Scheck L., Janka H.T., Foglizzo T., Kifonidis K., 2008, *A&A* 477, 931
- Scheck L., Kifonidis K., Janka H.T., Müller E., 2006b, *A&A* 457, 963
- Scheck L., Plewa T., Janka H.T., et al., 2004, *Physical Review Letters* 92, 011103
- Sedov L.I., 1946, *Prikl. Mat. Mekh.*
- Sedov L.I., 1959, *Similarity and Dimensional Methods in Mechanics*, *Similarity and Dimensional Methods in Mechanics*, New York: Academic Press, 1959
- Sharp D.H., 1984, *Physica D Nonlinear Phenomena* 12, 3
- Shigeyama T., Nomoto K., Tsujimoto T., Hashimoto M.A., 1990, *ApJL* 361, L23
- Sommerfeld A., 1949, *Partial Differential Equations in Physics*, p. 188, Academic Press, New York
- Stairs I.H., 2004, *Science* 304, 547
- Strutt J.W., 1900, *Scientific Papers*, Vol. II, p. 200, Cambridge University Press, Cambridge England (Lord Rayleigh)
- Taylor G.I., 1950, *Proc. R. Soc. London Ser. A* 201
- Timmes F.X., Swesty F.D., 2000, *ApJS* 126, 501
- Trümper J.E., Burwitz V., Haberl F., Zavlin V.E., 2004, *Nuclear Physics B Proceedings Supplements* 132, 560
- Tuohy I.R., Burton W.M., Clark D.H., 1982, *ApJL* 260, L65
- Tuohy I.R., Dopita M.A., 1983, *ApJL* 268, L11
- Unsöld A., Baschek B., 1999, *Der neue Kosmos*, Springer, Berlin Heidelberg New York, sixth edition
- Utrobin V.P., 2004, *Astronomy Letters* 30, 293
- Utrobin V.P., Chugai N.N., 2005, *A&A* 441, 271
- Wang L., Baade D., Höflich P., Wheeler J.C., 2003, *ApJ* 592, 457
- West R.M., Reipurth B., Jorgensen H.E., et al., 1987, *IAU Circ.* 4319, 1
- Wosley S., Janka H.T., 2005, *Nature Physics*
- Wosley S.E., Eastman R.G., 1997, In: Ruiz-Lapuente P., Canal R., Isern J. (eds.) *NATO ASIC Proc. 486: Thermonuclear Supernovae.*, p.821
- Wosley S.E., Heger A., Weaver T.A., 2002, *Reviews of Modern Physics* 74, 1015
- Wosley S.E., Phillips M.M., 1988, *Science* 240, 750
- Wosley S.E., Pinto P.A., Ensmann L., 1988a, *ApJ* 324, 466
- Wosley S.E., Pinto P.A., Martin P.G., Weaver T.A., 1987, *ApJ* 318, 664
- Wosley S.E., Pinto P.A., Weaver T.A., 1988b, *Proceedings of the Astronomical Society of Australia* 7, 355
- Zhang Q., Sohn S.I., 1996, *Physics Letters A* 212, 149
- Zhang Q., Sohn S.I., 1997, *Physics of Fluids* 9, 1106
- Zimmermann H., Weigert A., 1999, *Lexikon der Astronomie*, Spektrum Akademischer Verlag, Berlin Heidelberg New York, eighth edition

Online References

Astrophysics Data System (ADS), National Aeronautics and Space Administration (NASA):
<http://adswww.harvard.edu/index.html>

Cerro Tololo Inter-American Observatory (CTIO)
<http://www.ctio.noao.edu>

Description of the *NOVA laser facility*
<https://www.llnl.gov/str/Remington.html>

HyperMath Homepage by C.R. Nave
<http://hyperphysics.phy-astr.gsu.edu/hbase/hmat.html>

Lawrence Livermore National Laboratory
<https://www.llnl.gov>

Lick Observatory and the Tenagra Observatory Supernova Searches (LOTOSS)
<http://astro.berkeley.edu/~bait/lotoss.html>

List of Supernovae at the Harvard-Smithsonian Center for Astrophysics
<http://www.cfa.harvard.edu/supernova/finders/Supernovae.html>

South African Astronomical Observatory (SAAO)
<http://www.sao.ac.za>

The Flow of the Year 1997 from Chanhong Hu
<http://www.riam.kyushu-u.ac.jp/ship/STAFF/hu/flow.html>

Acknowledgement

First I like to thank Ewald Müller for offering me this interesting topic to work on, for believing in and supporting me.

I also like to thank H.-Thomas Janka for being interested in my work, for a lot of fruitful discussions and many good advices.

A special thanks goes to Konstantinos Kifonidis for having made this version of PROMETHEUS so fast, that I was able to finish my simulation in time and for the fruitful discussions on this topic. And I like to thank Leonhard Scheck for providing his 3D models, without my work would not have been possible.

I thank Andreas Marek and Martin Obergaulinger for helping me by having good advices, having always time for good discussions and their friendship. And I would like to thank my office mate Bernhard Müller for a lot of long and useful discussion, aswell for being a calm companion in workaday life.

I would like to thank the members and former members of the working group for a lot of good discussions and a very good working atmosphere. These are Miguel Angel Aloy, Almudena Arcones, Andreas Bauswein, Reiner Birkel, Robert Buras, Pablo Cerda-Duran, Harald Dimmelmeier, Michael Fink, Michael Gabler, Stephan Hachinger Wolfgang Hillebrandt, H.-Thomas Janka, Konstantinos Kifonidis, Markus Kromer, Thomas Mädler, Andreas Marek, Paolo Mazzali, Miroslav Mocak, Pedro Montero, Bernhard Müller, Ewald Müller, Martin Obergaulinger, Roland Oechslin, Rüdiger Pakmor, Fritz Röpke, Daniel Sauer, Leonhard Scheck, Stuart Sim, Stefan Taubenberger, Annop Wongwathanarat and Burkhard Zink.

I also like to thank the Institute's members of MPA for giving me a very interesting, joyful and wonderful time.

This research was supported by a large computer time grant at the *Leibnitz Rechenzentrum (LRZ) München* and the computational environment of the *Rechenzentrum der Max Planck Gesellschaft (RZG)* in Garching

Another special thanks goes to Conny Wendler from the HLRB II team at LRZ, who did everything to get me computer time very fast.

I would like to thank Monika Schwetz from the Agentur für Arbeit in Freising for her understanding of my situation and for being very cooperative.

I thank my beloved Ruth for pushing and encouraging me, but nevertheless being calm with me and furthermore, for correcting the language of this thesis.

At last I want to give many thanks to my wonderful parents Elvira and Joachim for supporting me so many years and my brother Daniel for often being a mirror to myself.

I apologise if I have forgotten somebody to mention here.

Curriculum Vitae

Personal Information

Place and date of birth: Konstanz, 02 November 1977

Citizenship: German

Education

Jan 2005 – Nov 2008	PhD student, Max Planck Institute for Astrophysics
26 Jul 2004	University diploma in physics (Dipl. phys.) <i>Irradiated Accretion Disc Models</i>
Oct 2000 – Sep 2004	Eberhard-Karls-Universität of Tübingen
11 Apr 2001	prediploma (minors: mathematics, chemistry)
Oct 1998 – Sep 2000	University of Stuttgart
26 Jun 1997	school leaving certificate (Abitur)
Sep 1994 – Jul 1997	Education as PTA (laboratory assistant in physics), Kerschensteiner Schule
Sep 1994 – Jul 1997	Gymnasium, Kerschensteiner Schule
Sep 1988 – Jul 1994	Secondary School, Reinhold-Nägele-Realschule
Sep 1984 – Jul 1988	Elementary School, Grundschule Strümpfelbach

Professional Experience

- Oct 2000 – Jun 2003 Graduate Assistant, Institut for Astronomy and Astrophysics, Section Astronomy, University of Tübingen
- Nov 1999 – Oct 2001 Graduate Assistant (Operator at the DYNAMITRON linear accelerator), Institut for Radiationphysics, University of Stuttgart
- Sep 1998 – Oct 1999 Graduate Assistant, Fraunhofer-Institut for Productionstechnics and Automation IPA, Stuttgart
- Sep 1994 – Jun 1997 Education as PTA (laboratory assistent in physics), Kerschensteiner Schule

Teaching Experience

- Oct 2003 – Sep 2004 Institute for Experimental Physics, University of Tübingen
Teaching Assistent for an undergraduate laborator class on physics for non-physics majors. Topics covered: mechanics, electricity, optics, atomic and nuclear physics
- Oct 2005 – Sep 2006 Institute for Experimental Physics, Technical University München
Teaching Assistent for an undergraduate laborator class on physics for physics majors. Topics covered: mechanics: moment of inertia

Service

- Jul 1997 – Jul 1998 Civil Service, Deaconry Social Station, Waiblingen

Memberships in Professional Societies

- Astronomische Gesellschaft
Deutsche Physikalische Gesellschaft